ALMA MATER STUDIORUM · UNIVERSITÀ DI BOLOGNA

SCUOLA DI SCIENZE
Corso di Laurea Magistrale in Astrofisica e Cosmologia

Cosmological exploitation of the size function of cosmic voids identified in the distribution of biased tracers

Presentata da:

Sofia Contarini

Relatori:

Ch.mo Prof. Lauro Moscardini
Dott. Federico Marulli
Dott. Tommaso Ronconi

Appello II
Anno Accademico 2017-2018

Contents

Abstract

Cosmic voids are large underdense regions of the Universe that, together with galaxy clusters, filaments and walls, characterise the large-scale structure of the Universe, the so-called *cosmic web*. They emerged from the negative perturbations in the primordial Gaussian density fluctuation field, and became more spherical as evolving in the mildly non-linear regime (Icke, 1984). Analogously to galaxy clusters, their *positive counterparts* in the density field, their number counts and density profiles provide powerful cosmological probes, despite the difficulty in constructing complete and well-characterised void catalogues. The statistical properties and evolution of cosmic voids can be accurately investigated with numerical simulations. Recently, thanks to the huge amount of data coming from wide galaxy surveys, large cosmic void catalogues have been constructed and used to constrain cosmology.

The statistical description of the void size function has been developed by Sheth and van de Weygaert (2004), and then revisited by Jennings et al. (2013). It has been proved that these models can accurately describe the size function of cosmic voids identified in the dark matter density field, provided that the void sample is appropriately cleaned from spurious objects (Ronconi and Marulli, 2017). However, to exploit voids as cosmological probes, it is necessary to extend the models to more realistic cases, that is to describe the underdense regions in the density distribution of galaxies which are biased tracers. Since voids in biased tracers are systematically larger than those identified in the dark matter field, a correction to the dark matter void size function is necessary. A possible procedure to take into account the effect of bias on the size distribution of cosmic voids has been proposed by Ronconi et al. (in preparation). This consists in modifying properly the density threshold used to define the voids.

The scientific goals of this thesis work are the following: *(i)* to test the algorithm to clean void catalogues developed by Ronconi and Marulli (2017) on Λ-cold dark matter (ΛCDM) N-body simulations, *(ii)* to quantify the accuracy of the theoretical void size function model with dark matter catalogues, *(iii)* to re-parametrise the theoretical model of the void size function

for biased tracers, and *(iv)* to investigate the cosmological constraining power of cosmic void statistics.

For these purposes, we made use of large, high-resolution halo catalogues extracted from ΛCDM N-body simulations. From these catalogues of biased tracers we extracted void catalogues with the Void IDentification and Examination toolkit (VIDE) (Sutter et al., 2015), a widespread void detection code. Then the VIDE void catalogues have been cleaned exploiting the algorithm developed by Ronconi and Marulli (2017). This procedure removes all the spurious voids from the catalogue and re-scales the void radii to a defined density threshold. All the statistical analyses and the catalogue manipulations have been performed with the CosmoBolognaLib (Marulli et al., 2016), a large set of *free software* C++/Python libraries that provide an efficient numerical environment for cosmological investigations of the large-scale structure of the Universe.

The main result of this thesis work is a new parameterisation of the theoretical void size function that takes into account the effect of the tracer bias. We found that the theoretical void number density is systematically underpredicted if the effective bias is used to assess the density threshold in the model. In fact, as already noted by Pollina et al. (2017, 2018), the tracer bias inside small cosmic voids deviates from the one at large scales. We verified this phenomenon by estimating the bias from the ratio between the averaged void density profiles traced by dark matter and biased tracers. In particular, the bias computed with this technique is systematically larger than the linear effective bias of the tracers used to identify the voids. Thus, we used the former to re-parameterise the theoretical size function, in order to compare it to the one measured from the halo catalogues. Thanks to this new parameterisation, that has been calibrated and tested in this thesis work, the theoretical void size function is now fully consistent with the result of numerical simulations. Finally, we investigate the effect of varying some of the cosmological parameters used to compute the theoretical void size function.

Sommario

I vuoti cosmici sono vaste regioni sottodense dell'Universo che, insieme agli ammassi di galassie, ai filamenti e ai muri, caratterizzano la struttura su larga scala dell'Universo, la cosidetta *ragnatela cosmica*. I vuoti emergono dalle perturbazioni negative del campo primordiale gaussiano di fluttuazioni di densità e hanno la caratteristica di diventare sempre più sferici, evolvendo in regime lievemente non-lineare (Icke, 1984). Analogamente agli ammassi di galassie, la loro *controparte positiva* nel campo di densità, i loro conteggi e i profili di densità forniscono un potente test cosmologico, nonostante la difficoltà nel costruirne cataloghi completi e ben caratterizzati. Le proprietà statistiche e l'evoluzione dei vuoti cosmici possono essere analizzate accuratamente con simulazioni numeriche. Recentemente, grazie all'enorme quantità di dati proveniente dalle grandi survey di galassie, è stato possibile costruire cataloghi di vuoti cosmici sufficientemente estesi da poter essere utilizzati per misurare accuratamente i principali parametri del modello cosmologico.

La descrizione statistica della *size function* dei vuoti è stata sviluppata da Sheth and van de Weygaert (2004), e successivamente rivisitata da Jennings et al. (2013). È stato provato che questi modelli sono in grado di descrivere accuratamente la *size function* dei vuoti cosmici identificati nel campo di densità della materia oscura (DM), a patto che il campione di vuoti sia stato precedentemente ripulito dagli oggetti spuri (Ronconi and Marulli, 2017). Ciononostante, per poter utilizzare i vuoti come test cosmologici, è necessario estendere i modelli a casi più realistici, che descrivano le regioni sotto-dense nella distribuzione di densità delle galassie, che sono traccianti con bias. Dato che i vuoti nei traccianti con bias sono sistematicamente più grandi di quelli identificati nel campo di DM, è necessaria una correzione alla *size function* dei vuoti tracciati dalla DM. Una possibile procedura per considerare gli effetti del bias sulle distribuzioni di grandezza dei vuoti cosmici è stata proposta da Ronconi et al. (in preparation), e consiste nel modificare opportunamente la soglia di densità utilizzata per definire i vuoti.

Gli obiettivi di questo lavoro di tesi sono i seguenti: (i) testare l'algoritmo per la pulizia dei cataloghi sviluppato da Ronconi and Marulli (2017) su sim-

ulazioni N-body del modello Λ-cold dark matter (ΛCDM), (*ii*) quantificare l'accuratezza del modello teorico basato sulle *size function* dei vuoti con cataloghi di DM, (*iii*) riparametrizzare il modello teorico delle *size function* dei vuoti per traccianti con bias, e (*iv*) analizzare l'efficacia della statistica dei vuoti nel porre vincoli ai parametri cosmologici.

Per questi scopi, sono stati utilizzati grandi cataloghi di aloni ad alta risoluzione, ottenuti da simulazioni N-body ΛCDM. Da questi cataloghi di traccianti con bias sono stati estratti cataloghi di vuoti con il *Void IDentification and Examination toolkit* (VIDE) (Sutter et al., 2015), un codice per l'individuazione dei vuoti ampiamente utilizzato. Dopodiché i cataloghi di vuoti ottenuti con VIDE sono stati ripuliti utilizzando l'algoritmo sviluppato da Ronconi and Marulli (2017). Questa procedura rimuove tutti i vuoti spuri dal catalogo e riscala i raggi dei vuoti ad una soglia di densità fissata. Tutte le analisi statistiche e il trattamento dei cataloghi sono stati eseguiti con le CosmoBolognaLib (Marulli et al., 2016), un insieme di librerie C++/Python pubbliche, che forniscono un ambiente numerico efficiente per lo studio cosmologico di strutture su larga scala dell'Universo.

Il risultato principale di questo lavoro di tesi consiste in una nuova parametrizzazione delle *size function* teoriche dei vuoti, che considera l'effetto del bias dei traccianti. Ciò che abbiamo trovato è che la densità numerica teorica dei vuoti è sistematicamente sottostimata quando viene utilizzato il bias effettivo per stimare la soglia di densità nel modello. Di fatto, come era stato già evidenziato da Pollina et al. (2017, 2018), il bias dei traccianti calcolato in prossimità dei vuoti, devia da quello misurato a grandi scale, almeno quando si considerano vuoti di dimensioni ridotte. Questo fenomeno è stato verificato stimando il bias dal rapporto tra i profili medi di densità dei vuoti definiti dalla DM e quelli ottenuti da traccianti con bias. In particolare, il bias calcolato con questo metodo è sistematicamente più grande del bias lineare effettivo dei traccianti usati per identificare i vuoti. Per questo è stato utilizzato il primo di questi valori per riparametrizzare la *size function* teorica, che è stata poi confrontata con quella ottenuta dalle misure sui cataloghi di aloni della simulazione.

Grazie a questa nuova parametrizzazione, calibrata e testata in questo lavoro di tesi, la *size function* teorica dei vuoti è ora pienamente consistente con i risultati delle simulazioni numeriche. Infine, sono state fornite previsioni sui vincoli cosmologici che possono essere ottenuti utilizzando queste statistiche sui cataloghi di vuoti delle future survey.

Introduction

The concordance ΛCDM model is currently widely accepted, and it is known as the Standard Cosmological Model. This model is based on two fundamental assumptions: *(i)* the presence of *cold dark matter*, an unknown type of non-relativistic particles that apparently seem to interact only through gravity with the common baryonic matter; *(ii)* the existence of a mysterious energy component responsible for the present accelerated expansion of the Universe, the so-called *dark energy*, that in its simplest version is described by the Cosmological Constant, Λ. The behavior of these components is, at least up to now, far to be completely understood. Cold DM and DE constitute the majority component of the Universe, with a percentage of abundance of approximately 26% and 70%, respectively.

Despite the ΛCDM scenario shows a remarkably successful agreement with most of the available observations, there are still some possible tensions between its predictions and observations at small scales. In particular, we can recall the abundance of satellite galaxies in cold DM haloes, the low baryon fraction in galaxy clusters and the "cusp-core" problem for the halo density profiles (Allen et al., 2004; LaRoque et al., 2006; Newman et al., 2009). Moreover, the fundamental nature of cold DM particles and of the DE component is still unknown and other issues remain still unresolved, like the problem of coincidence (that will be analysed in section 1.5) and the currently lack of comprehension of the physics of inflation.

In this scenario, the formation of the cosmic structures observed in the present-day Universe starts from the gravitational collapse of the initial perturbations in the Gaussian primordial density field. From this initial collapse, a hierarchical process of formation begins. First DM haloes are formed, which are virialised, gravitationally bound structures that provide the potential wells in which baryons can cool and condense. Then, inside the DM haloes, the luminous objects that we can observe in the sky are born, as galaxy and galaxy clusters.

Among these structures, organised in filaments and walls, *cosmic voids* emerge as large underdense regions from which matter is pushed away as effect of gravity and because of the action of dark energy. They represent the result of the evolution of underdensities in the primordial density field. As it can be seen in figure 1, cosmic voids constitute a major part of the Universe: while galaxy clusters enclose most of the mass in the Universe, voids are the dominant spatial component, accounting for the $90 - 95\%$ of the entire volume (Platen et al., 2007). Their sizes span over a wide range of scales, from diameters of 3-5 Mpc (*minivoids*) to about 200 Mpc (*supervoids*) (Szapudi et al., 2015; Tikhonov and Karachentsev, 2006). Voids are only mildly non-linear objects, and tend to become more spherical as they evolve, which suggests that their evolution should be easier to describe than that of positive perturbations. Thanks to their relatively simple structure and shape, voids are useful probes of a variety of cosmological parameters and have indeed been shown to possess great potential for constraining dark energy and testing theories of gravity (see e.g. Pisani et al., 2015; Sahlén and Silk, 2016; Pollina et al., 2016; Hawken et al., 2017).

In this thesis work we will test the theoretical model for the void statistical distribution as a function of size proposed by Jennings et al. (2013). In particular, we will make use of voids traced by the distribution of DM haloes. As in the case of real data catalogues, we will have to take into account the bias between the underlying DM distribution and the tracers used to build the void catalogues. In order to estimate the theoretical void size function, an accurate analysis of the halo bias will be performed. After having established the value of tracer linear bias, b, necessary to recover the size distribution of voids in the DM distribution, we will perform a re-parametrisation of the void theoretical size function. Since cosmic voids are defined as spheres embedding a fixed density contrast $\delta_{v,tr}^{NL} = -0.795$ (defined by the phenomenon of *shell-crossing*, that will be examined in section 2.1), we will re-scale this threshold to the value $\delta_{v,DM}^{NL} = \delta_{v,tr}^{NL}/b$ in order to derive the equivalent one in the DM particles distribution. This value will be then converted in the corresponding one in the linear theory with the method described in Bernardeau (1994), and then will be inserted in the theoretical model for the size function. The aim of this re-parametrisation is to predict the distribution of voids traced by the underlying DM distribution, supposing to have information only on the tracer one. In fact, dealing with real data catalogues, it can be really challenging to investigate the properties of the underneath total mass distribution.

We will demonstrate that, with this prescription, the measured size function of voids is fully consistent with the theoretical predictions. Moreover, it will be possible to exploit the proposed method to derive constraints on the cosmological parameters of the model and extend the entire procedure to real data catalogues.

Our work is organized as follows:

- In chapter 1 we give a general introduction to the cosmological framework, introducing the theoretical basis of the Standard Cosmological Model.

- In chapter 2 we illustrate some of the general properties of cosmic voids, focusing in particular on their definition and main statistical properties.

- Chapter 3 provides a general overview of the main algorithms and computational tools we used in our work.

- Chapter 4 presents an accurate analysis of the tracer bias.

- In chapter 5 we apply the techniques previously described to halo catalogues extracted from N-body simulations, we compute the theoretical size function for voids identified in the distributions of biased tracers, and investigate the dependence of the void size function on some cosmological parameters of the ΛCDM model.

- Finally, in chapter 6 we summarise our results and discuss future developments of this work.

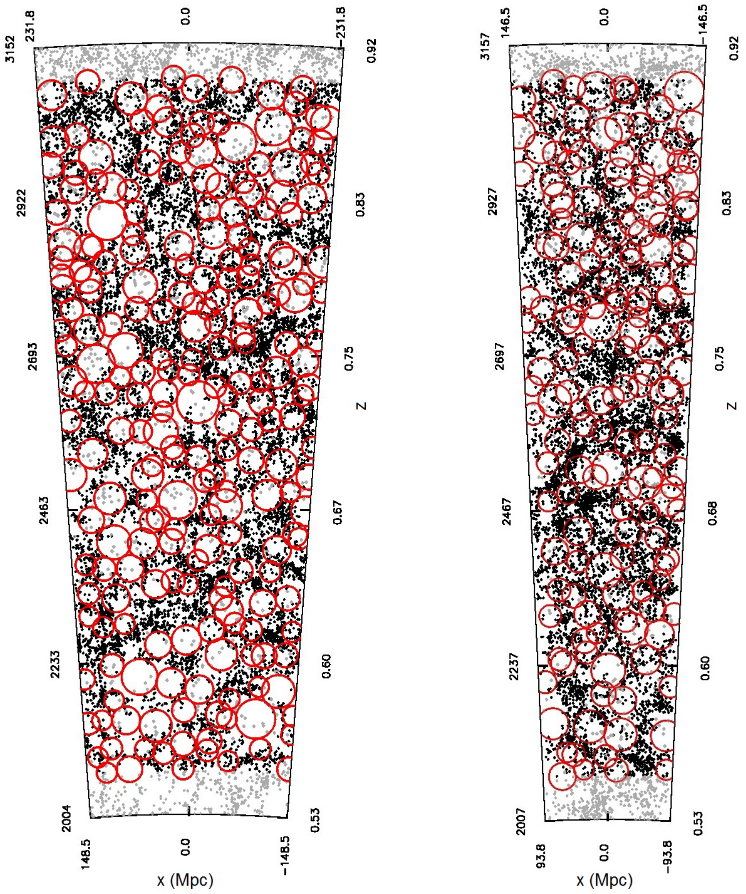

Figure 1: Two samples of galaxies obtained from the VIMOS Public Extragalactic Redshift Survey (VIPERS). Cosmic voids are depicted with red circles, representing the maximal spheres embedding a fixed level of density. The black dots are the galaxies of the sample in the given z-range, while the grey dots are the galaxies detected as isolated, or outside the redshift range. The scales show comoving distances in Mpc and the corresponding redshift. Credits: Micheletti et al. (2014).

Chapter 1

Cosmological framework

In this chapter we briefly summarise the cosmological framework on which this thesis work is built on. Our aim is to provide an overview on the basic mathematical structure of modern cosmological models based on the General Theory of Relativity. In particular, we provide an introduction to the Friedmann-Robertson–Walker metric, that describes the curvature of the hypersurfaces defined by the space-time. After the introduction of the Hubble Law and the definition of redshift, we illustrate the Friedmann Equations, as the solutions to the Einstein's Field Equation. Then we describe the main features of the currently adopted Standard Cosmological model. Finally, we introduce the Jeans theory, that deals with the gravitational instability of the primordial fluctuations and leads to the growth of the large-scale structures of the Universe.

1.1 Fundamentals of General Relativity

The force of gravity is the predominant interaction on sufficiently large scales. For this reason, the cosmological models are mainly based on the action of this force. The best description of this force is given by the Theory of General Relativity (GR), proposed by Albert Einstein (Einstein, 1915).

In the context of GR, the geometry of space-time is described by the *metric tensor* $g_{\mu\nu}$. The importance of the metric tensor emerges from the following equation:

$$\mathrm{d}s^2 = g_{\mu\nu}\mathrm{d}x^\mu \mathrm{d}x^\nu \quad (\mu, \nu = 0, 1, 2, 3) \ ,$$

which represents the minimum distance in the space-time between the events labelled by $x^j = (t, x_1, x_2, x_3)$ and $x^j + \mathrm{d}x^j = (t + \mathrm{d}t, x_1 + \mathrm{d}x_1, x_2 + \mathrm{d}x_2, x_3 + \mathrm{d}x_3)$, where x_i represent the spatial coordinates and t the proper time. This interval can be explicitly separated as:

$$\mathrm{d}s^2 = g_{00}\mathrm{d}t^2 + 2g_{0i}\mathrm{d}x^i\mathrm{d}t + g_{ij}\mathrm{d}x^i\mathrm{d}x^j \ , \tag{1.1}$$

where $g_{00}dt^2$ is the time component, $g_{ij}dx^idx^j$ the spatial components and $2g_{0i}dx^idt$ the mixed components.

The space-time metric is connected with the energy-momentum tensor $T_{\mu\nu}$, which decribes the matter and energy content of the Universe, by the Einstein's Field Equation of GR:

$$R_{\nu\mu} - \frac{1}{2}g_{\nu\mu}R = \frac{8\pi G}{c^4}T_{\mu\nu} \ , \tag{1.2}$$

where G represents the gravitational constant and c the speed of light. $R_{\mu\nu}$ and R are the Ricci Tensor and Scalar, respectively defined using the fourth-order Riemann Tensor $R^{\mu}_{\alpha\beta\gamma}$:

$$R_{\alpha\beta} \equiv R^{\mu}_{\alpha\beta\mu}$$

$$R \equiv R^{\mu}_{\mu} = g^{\mu\nu}R_{\mu\nu} \ .$$

Considering the left-hand side of equation (1.2), we can define the Einstein tensor $G_{\mu\nu}$ as:

$$G_{\mu\nu} \equiv R_{\nu\mu} - \frac{1}{2}g_{\nu\mu}R \ , \tag{1.3}$$

which returns information about the space-time geometry. Equation (1.2) implies that the geometry of the Universe is determined by its content of matter and energy. Assuming the standard Big Bang model, we can consider the different energy components as perfect fluids, that are constituted by particles having a mean free path much lower than the physical scales of interaction. Under this hypothesis, we can write the energy-momentum tensor for the different components as:

$$T_{\mu\nu} = -pg_{\mu\nu} + (p + \rho c^2)u_\mu u_\nu \ , \tag{1.4}$$

where p represents the pressure term, ρc^2 is the energy density term and u_i are the components of the 4-velocity of the fluid element.

1.2 The Friedmann-Robertson-Walker metric

All the models developed in modern cosmology are based on a fundamental assumption, the *Cosmological Principle* (CP), that is the hypothesis of isotropy and homogeneity of the Universe on sufficiently large scales (hundreds of megaparsecs nowadays). Isotropy is the property of looking the same in every direction, while homogeneity is the property of being identical everywhere in space. Once assumed the validity of this hypothesis, our goal is to build a model of the Universe satisfying the CP. We can define a universal time such that the spatial metric is the same at each position in space. Thanks to the assumption of isotropy, the mixed components g_{0i} of the equation (1.1) have to be null. Thus we can obtain the general form of the metric:

$$\mathrm{d}s^2 = c^2\mathrm{d}t^2 - g_{ij}\mathrm{d}x^i\mathrm{d}x^j = (c\mathrm{d}t)^2 - \mathrm{d}l^2 \ . \tag{1.5}$$

Any point in space-time is marked with a set of three spatial coordinates x_i $(i = 1, 2, 3)$, called *comoving coordinates*, which are the coordinates at rest with the Universe expansion. In the same way, we can define the *proper time*, t, as the time measured by a clock at rest with the expansion of the Universe. To determine g_{ij} we have to find a spatial 3D metric which follows the requirements of homogeneity and isotropy of the CP.

The geometrical properties of the space-time are described by the metric. In particular, the 3-dimensional Riemann tensor R_{ijkl} determines the curvature of a 3-dimensional space, while the scalar curvature is given by $R = g_{ij}R^{ij}$, obtained from the contraction of the Ricci tensor with the metric g_{ij}. Thanks to the assumption of the CP, the tensor R_{ijkl} does not depend on the derivatives of the metric g_{ij}, while the scalar R has to be constant. For the symmetry properties of the deriving form of the Riemann tensor, it is possible to define the most general form of equation (1.5), in the *Friedmann-Robertson-Walker* (FRW) metric:

$$\mathrm{d}s^2 = c^2\mathrm{d}t^2 - a^2(t)\left[\frac{\mathrm{d}r^2}{1-\kappa r^2} + r^2(\sin^2\theta\ \mathrm{d}\phi^2 + \mathrm{d}\theta^2)\right] \ , \tag{1.6}$$

where $a(t)$ is the cosmic scale factor (or the expansion parameter), having the dimensions of a length, and κ is the curvature parameter. The equation (1.6) expresses the metric in spherical polar coordinates, being r, ϕ and θ dimensionless comoving coordinates. Given an energy-momentum tensor, the value of κ and the function $a(t)$ can be derived by the Einstein's Field Equations.

Let us consider a free massive particle at rest at the origin of the comoving coordinates system at a fixed instant in time. The absence of preferred directions ensures that no acceleration can be induced on this particle by the effect of gravity. Thanks to the required homogeneity, we can define as geodetic each world line with $x^i = const.$

The curvature of the space-time can be positive, zero or negative. This is determined by the parameter κ, which can assume only three possible values:

$\kappa = +1$ (closed universe, hyper-spherical geometry), $\kappa = 0$ (flat universe, Euclidean geometry) and $\kappa = -1$ (open universe, hyperbolic geometry).

Let us introduce a new coordinate χ defined as:

$$\chi \equiv \int \frac{\mathrm{d}r}{\sqrt{1-\kappa r^2}} \ . \tag{1.7}$$

By considering the three possible values of κ in the equation (1.7) we obtain:

$$\chi = \begin{cases} \sin^{-1} r & \text{for } \kappa = +1 \\ r & \text{for } \kappa = 0 \\ \sinh^{-1} & \text{for } \kappa = -1 \end{cases} \ . \tag{1.8}$$

Now it is possible to re-write the spatial part of the FRW metric in terms of (χ, θ, ϕ):

$$\mathrm{d}l^2 = a^2 \left[\mathrm{d}\chi^2 + f^2(\chi)(\mathrm{d}\theta^2 + \sin^2\theta \ \mathrm{d}\phi^2)\right] \ , \tag{1.9}$$

where

$$f(\chi) = \begin{cases} \sin(\chi) & \text{for } \kappa = +1 \\ \chi & \text{for } \kappa = 0 \\ \sinh(\chi) & \text{for } \kappa = -1 \end{cases} \ . \tag{1.10}$$

For $\kappa = +1$ the Universe has a finite volume, analogous to the two-dimensional case of a sphere. In this case, the equation (1.9) describes a 3D-sphere with radius a in a four-dimensional flat space defined by:

$$x_0^2 + x_1^2 + x_2^2 + x_3^2 = a^2 \ ,$$

where (x_0, x_1, x_2, x_3) are the Cartesian coordinates. It is also possible to introduce the angular coordinates (χ, θ, ϕ), obtaining the relations:

$$\begin{cases} x_1 = a\cos\chi \ \sin\theta\sin\phi \\ x_2 = a\cos\chi \ \sin\theta\cos\phi \\ x_3 = a\cos\chi \ \cos\theta \\ x_4 = a\sin\chi \end{cases} \ .$$

By expressing $\mathrm{d}x_i$ in terms of polar coordinates the line element of the sphere

$$\mathrm{d}L^2 = \mathrm{d}x_0^2 + \mathrm{d}x_1^2 + \mathrm{d}x_2^2 + \mathrm{d}x_3^2$$

becomes:

$$\mathrm{d}L^2_{sphere} \equiv a^2 \left[\mathrm{d}\chi^2 + \sin^2\chi \ (\sin^2\theta \ \mathrm{d}\phi^2 + \mathrm{d}\theta^2)\right] \ ,$$

which is identical to the equation (1.9) with $\kappa = +1$. The space of the closed Universe is totally covered, at a fixed time, by the following range of angles:

$$0 \leq \chi < \pi \quad , \quad 0 \leq \theta < \pi \quad , 0 \leq \phi < 2\pi \ ,$$

with a (finite) volume given by:

$$V = a^3 \int_0^{2\pi} \mathrm{d}\phi \int_0^{\pi} \sin\theta \ \mathrm{d}\theta \int_0^{\pi} \sin^2\chi \ \mathrm{d}\chi = 2\pi^2 a^3 \ .$$

The surface of this sphere can be parameterised in terms of χ:

$$S = 4\pi a^2 \sin^2\chi \ .$$

This surface reaches the maximum value for $\chi = \pi/2$, then it decreases and becomes null for $\chi = 0, \pi$. In such a space, the sum of the internal angles of a triangle is larger than π and the surface $S(\chi)$ is systematically larger with respect to the one in an Euclidean geometry.

In the case of $\kappa = -1$ the geometry of the Universe is hyperbolic. In the 3D space a hyperboloid is defined by the following relation:

$$-x_0^2 - x_1^2 - x_2^2 - x_3^2 = a^2.$$

Analogously to the spherical case described above, the line element is:

$$\mathrm{d}L^2 = \mathrm{d}x_0^2 + \mathrm{d}x_1^2 + \mathrm{d}x_2^2 - \mathrm{d}x_3^2 \ .$$

Introducing the angular coordinates (χ, θ, ϕ) also in this case, we obtain:

$$\begin{cases} x_1 = a \sinh\chi \ \sin\theta \sin\phi \\ x_2 = a \sinh\chi \ \sin\theta \cos\phi \\ x_3 = a \sinh\chi \ \cos\theta \\ x_4 = a \cosh\chi \end{cases}$$

and the line element becomes:

$$\mathrm{d}L^2_{hyperboloid} \equiv a^2 \left[\mathrm{d}\chi^2 + \sinh^2\chi \ (\sin^2\theta \ \mathrm{d}\phi^2 + \mathrm{d}\theta^2)\right] \ .$$

The properties of a geometrical space having a constant negative curvature are similar to those of a flat case. In fact, it represents an infinite open Universe. The range of coordinates are the following:

$$0 \leq \chi < \infty \quad , \quad 0 \leq \theta < \pi \quad , 0 < \phi < 2\pi \ ,$$

and the surface S is defined by:

$$S = 4\pi a^2 \sinh^2\chi \ .$$

In this particular case, the sum of the internal angles of a triangle is smaller than π and the surface is greater than the Euclidean one.

1.3 Hubble Law and redshift

Let us consider two points P and P' at a given time t. With a FRW metric, the *proper distance*, d_{pr}, between these events is:

$$d_{pr} = a(t) \int_0^r \frac{\mathrm{d}r'}{\sqrt{1-\kappa r'^2}} = a(t)F(r)\,, \tag{1.11}$$

and depends on time through the scale parameter $a(t)$. At time t, the proper distance is related to the present one ($t = t_0$) by the following relation:

$$d_c \equiv d_{pr}(t_0) = a_0 F(r)\ , \tag{1.12}$$

where $a_0 \equiv a(t = t_0)$. Hereafter if a variable has the subscript "0", it will indicate that such quantity is calculated at $t = 0$. The previous quantity is called the *comoving distance* and remains constant with the expansion of the Universe. The direct connection between the two definitions is given by the equation:

$$d_{pr} = \frac{a(t)}{a_0} d_c\ . \tag{1.13}$$

The expansion of the Universe causes a continuous drifting apart of any two points in the space. The *radial velocity* between these points can be computed as the derivative of d_{pr} with respect to t:

$$v_r = \frac{\mathrm{d}}{\mathrm{d}t} d_{pr} = \frac{\mathrm{d}}{\mathrm{d}t}[a(t)F(r)] = \dot{a}(t)F(r) + a(t)\dot{F}(r)\ . \tag{1.14}$$

Because of the time-independence of the term $F(r)$, the previous relation becomes:

$$v_r = \dot{a}(t)F(r) = \frac{\dot{a}(t)}{a(t)} d_{pr} = H(t) d_{pr}\ , \tag{1.15}$$

which is the well known *Hubble Law*, where we have defined the *Hubble Parameter* as $H(t) \equiv \dot{a}/a$. $H(t)$ is a function of time and has the same value across the Universe at a given cosmic time. Wang et al. (2017) performed a recent estimate of the Hubble constant $H_0 \equiv H(t = t_0)$ using the latest baryonic acoustic oscillations (BAO) measurements from galaxy surveys, finding a value of:

$$H_0 = 69.13 \pm 2.34\ \mathrm{km\ s^{-1}Mpc^{-1}}\ .$$

It is conventional to introduce a dimensionless parameter, h, redefining the Hubble parameter as:

$$H_0 \equiv 100h\ \mathrm{km\ s^{-1}Mpc^{-1}}\ .$$

We call the global motion of objects in the Universe with respect to each other the *Hubble Flow*. Being H_0 expressed in units of s^{-1}, the inverse of the Hubble parameter may provide a rough estimate of the age of the Universe (the most recent estimates lead to a more accurate value of 13.9 Gyr), by taking the simplified assumption that for all its history the Universe has expanded with the same rate.

Since on large scales all objects are affected by this expansion, their motion will result in a reddening of their observed spectrum, caused by the shift towards longer wavelengths. The *redshift* is defined as the relative difference between the observed, λ_{obs}, and emitted, λ_{em}, wavelengths:

$$z \equiv \frac{\lambda_{obs} - \lambda_{em}}{\lambda_{em}} = \frac{\Delta\lambda}{\overline{\lambda}} \ . \tag{1.16}$$

Let us consider a source emitting a photon with wavelength λ_{em} at time t_{em}. An observer located at a distance d will receive the signal with wavelength λ_{obs} at t_{obs}. By definition photons move along null geodesics ($ds^2 = 0$ for massless particles) during the expansion of the Universe. Taking once again the FRW metric in polar coordinates expressed in equation (1.6) and considering $\mathrm{d}\phi = \mathrm{d}\theta = 0$ for simplicity we have:

$$c^2\mathrm{d}t^2 - a^2(t)\frac{\mathrm{d}r^2}{\sqrt{1-\kappa r^2}} = 0 \ . \tag{1.17}$$

Integrating the metric along the path, the previous equation becomes:

$$\int_{t_{em}}^{t_{obs}} \frac{c \ \mathrm{d}t}{a(t)} = \int_0^r \frac{\mathrm{d}r'^2}{\sqrt{1-\kappa r'^2}} = F(r) \ . \tag{1.18}$$

We suppose now that a second photon is emitted from the source at $t'_{em} = t_{em} + \delta t_{em}$ and reaches the observer at $t'_{obs} = t_{obs} + \delta t_{obs}$. Since $F(r)$ does not change because of the assumption of comoving coordinates, the difference between the two photon paths is given only in terms of time:

$$\int_{t'_{em}}^{t'_{obs}} \frac{c \ \mathrm{d}t}{a(t)} = F(r) \ . \tag{1.19}$$

If the time intervals δt_{em} and δt_{obs} are small, $a(t)$ can be considered almost constant, so the equivalence between Equations (1.18) and (1.19) implies:

$$\frac{\delta t_{obs}}{a(t_{obs})} = \frac{\delta t_{em}}{a(t_{em})} \ . \tag{1.20}$$

Since $\delta t = 1/\nu$ and $\lambda = c/\nu$, we obtain:

$$1 + z = \frac{a_{obs}}{a_{em}} \tag{1.21}$$

or, more generally, for an observer located at present time and an emitting source at a generic instant t, we have:

$$1 + z = \frac{a_0}{a(t)} \ . \tag{1.22}$$

The redshift is generally exploited to measure the distance of extragalactic sources.

1.4 Friedmann equations

Without any assumption on the geometry of the Universe, we can apply the FRW metric (1.6) to the Einstein's Equations (1.2). Of the resulting system of equations only two of them are independent. The two solutions, with the hypotheses of perfect fluid and of the CP, provide the time evolution of $a(t)$ and describe the dynamic growth of the Universe. They are called the *First* and the *Second Friedmann Equations* and can be expressed as follows:

$$\ddot{a} = -\frac{4\pi}{3} G \left(\rho + \frac{3p}{c^2} \right) a \ , \tag{1.23}$$

$$\dot{a}^2 + \kappa c^2 = \frac{8\pi}{3} G \rho a^2 \ . \tag{1.24}$$

Each of these two equations can be recovered from the other one by applying the adiabatic condition:

$$\mathrm{d}\mathcal{U} = -p \mathrm{d}V \ ,$$

where $\mathcal{U}$ is the internal energy of the Universe. Its validity persists as long as the Universe is considered as a closed system, that expands and evolves without losing energy. Equation (1.4) can also be expressed as follows:

$$\mathrm{d}(\rho c^2 a^3) = -p \mathrm{d}a^3 \ , \tag{1.25}$$

$$\dot{p} a^3 = \frac{\mathrm{d}}{\mathrm{dt}} \left[a^3 (\rho c^2 + p) \right] \ , \tag{1.26}$$

$$\dot{\rho} + 3 \left(\rho + \frac{p}{c^2} \right) \frac{\dot{a}}{a} = 0 \ . \tag{1.27}$$

The density, ρ, in these equations has to be considered as the sum of all the densities of the components of the Universe.

1.4.1 Friedmann Models

Equations (1.23) and (1.24) were proposed by Alexander Friedmann in 1922 as solutions of Einstein's Field Equations. Since their first proposal, they have been studied and improved, giving birth to a set of different cosmological models. From equation (1.23) we can deduce that the evolution of a Universe described by this relation can not be static unless the following unphysical condition is verified:

$$\rho = -\frac{3p}{c^2} \ . \tag{1.28}$$

A Universe of this type is destined to collapse under the effect of this own gravity. Since Albert Einstein was firmly convinced that the Universe should be static, he applied the most general but simplest possible modification of the equation (1.2) by introducing the so-called *cosmological constant* Λ:

$$R_{\mu\nu} - \frac{1}{2} g_{\mu\nu} R - \Lambda g_{\mu\nu} = \frac{8\pi G}{c^4} T_{\mu\nu} \ . \tag{1.29}$$

As we shall see, an appropriate choice of Λ can imply a static model of the Universe. We can also re-write equation (1.29) by modifying the energy-momentum tensor:

$$R_{\mu\nu} - \frac{1}{2} g_{\mu\nu} R = \frac{8\pi G}{c^4} \tilde{T}_{\mu\nu}, \tag{1.30}$$

where the new tensor is formally given by:

$$\tilde{T}_{\mu\nu} \equiv T_{\mu\nu} + \frac{\Lambda c^4}{8\pi G} g_{\mu\nu} \ , \tag{1.31}$$

which implies a new definition for the pressure and the density:

$$\tilde{p} \equiv p - \frac{\Lambda c^4}{8\pi G} \quad \text{and} \quad \tilde{\rho} \equiv \rho + \frac{\Lambda c^2}{8\pi G}, \tag{1.32}$$

called now *effective pressure* and *effective density*, respectively.

When Edwin Hubble finally discovered the expansion of the Universe in 1922, Einstein regretted the introduction of the cosmological constant. Nevertheless, models with Λ have been reintroduced at the end of the 20th century to describe the observed accelerated expansion of the Universe. The action of Λ is to contrast the attractive pull of gravity behaving as a repulsive force. Nowadays, the origin of this "push" is commonly assigned to the Dark Energy and is considered is a valid method to account for the observed cosmic acceleration.

In order to solve the Equations (1.23) and (1.24), it is necessary to introduce an equation of state (EoS) for the fluid composing the Universe.

Adopting the perfect fluid approximation, the EoS of such fluid can be expressed by the general form:

$$p = w\rho c^2 \ , \tag{1.33}$$

where w is defined so that the sound speed is:

$$c_s \equiv \left(\frac{\partial p}{\partial \rho}\right)_S^{1/2} = c\sqrt{w} \ .$$

The parameter w lies in the so-called *Zel'dovich interval*:

$$0 \leq w < 1 \ , \tag{1.34}$$

in which c_s maintains a physical sense. The value of w changes depending on the type of the considered component. The "ordinary" components of the Universe can be divided into two big main families: relativistic and non-relativistic. The first case is represented by dust, having $w \simeq 0$, i.e. with negligible pressure, while a non-degenerate and ultra-relativistic fluid has an EoS with $w = 1/3$. This is the case for a radiative fluid or, more generally, for photons and relativistic particles like neutrinos. For what concerns Λ, it is defined to behave as a perfect fluid with $w = -1$ and it follows the equation (1.29), in analogy to the other components.

With these definitions, we can write the energy-momentum tensor as the sum of all the components i:

$$T_{\mu\nu} \equiv \sum_i T_{\mu\nu}^{(i)} \ .$$

From the combination of Equations (1.25) and (1.33), it is possible to derive the following relations:

$$\rho_w \propto a^{-3(1+w)} \propto (1+z)^{3(1+w)} \ , \tag{1.35}$$

which describe how the densities of the different components vary through cosmic time. As a result of the previous relations, we can assert that different components have dominated through the succession of the cosmic epochs, prevailing one over the others.

Equation (1.24) can be re-written to derive the curvature of the Universe previously inserted in the FRW metric:

$$\frac{\kappa}{a^2} = \frac{1}{c^2}\left(\frac{\dot{a}}{a}\right)^2 \left(\frac{\rho}{\rho_c} - 1\right) \ , \tag{1.36}$$

where

$$\rho_c(t) \equiv \frac{3}{8\pi G}\left(\frac{\dot{a}}{a}\right)^2 = \frac{3H^2(t)}{8\pi G} \tag{1.37}$$

is called the *critical density* and corresponds to the density requested to obtain a flat Universe ($\kappa = 0$). For $\rho < \rho_c$ the expansion of the Universe will go on indefinitely, while for $\rho > \rho_c$ it will be halted and then followed by a contraction. The critical density can be used to define the dimensionless *density parameter*:

$$\Omega(t) \equiv \frac{\rho(t)}{\rho_c(t)} \ , \tag{1.38}$$

which can be defined for each single component (Ω_w); the total density parameter (Ω_{TOT}) is the sum of all of them. In a flat Universe, $\Omega_{TOT} = 1$, while in open or closed universes it is $\Omega_{TOT} < 1$ and $\Omega_{TOT} > 1$, respectively. Now it is useful to re-write the equation (1.24) in terms of Ω, H and z, which are more representative parameters of the observable Universe. By combining the Second Friedmann Equation with the definition of the density parameter, the Hubble Law and the equation (1.22), we obtain:

$$H^2(z) = H_0^2(1+z)^2\left[1 - \sum_i \Omega_{0,w_i} + \sum_i \Omega_{0,w_i}(1+z)^{1+3w_i}\right] \ , \tag{1.39}$$

in which $H(z)$ is the Hubble parameter at a generic redshift and $\sum_i \Omega_{0,w_i} = \Omega_{TOT}$ is the total sum of all i-th components with corresponding w_i value. The quantity $1 - \sum_i \Omega_{0,w_i} \equiv \Omega_{0,\kappa}$ is related to the curvature of the Universe and it is called *curvature density parameter*.

Instead, re-writing the Second Friedmann Equation for a single component by applying the equation (1.2), we obtain:

$$\ddot{a} = -\frac{4\pi}{3} G\rho(1+3w)a \ . \tag{1.40}$$

This last equation implies that, if w belongs to the Zel'dovich interval, $\ddot{a} < 0$ for each t. From the Hubble law we can conclude that $a(t)$ grows monotonically, given the positivity of $H(t)$. This implies that, going back in time, there is an instant at which $a(t)$ is equal to zero, at some finite time in the past. This event is currently called the *Big Bang* (BB). All possible models of the Universe, assuming it is composed of a single fluid with $-1/3 < w < 1$, have necessarily an instant at which $a(t)$ vanishes, while the density and the expansion speed diverge. Note that the expansion of the Universe emerging from the BB model is a result of the initial conditions of homogeneity and isotropy and it is not due to pressure, which here acts to decelerate the expansion, contrary to what we may expect.

Generic w	$w = 0$	$w = 1/3$
$a(t) = a_0\left(\frac{t}{t_0}\right)^{\frac{2}{3(1+w)}}$	$a(t) \propto t^{2/3}$	$a(t) \propto t^{1/2}$
$t = t_0(1+z)^{\frac{-3(1+w)}{2}}$	$t \propto (1+z)^{-3/2}$	$t \propto (1+z)^{-2}$
$H(t) = \frac{2}{3(1+w)}t^{-1}$	$H(t) = \frac{2}{3t}$	$H(t) = \frac{1}{2t}$
$t_0 = \frac{2}{3(1+w)}\frac{1}{H_0}$	$t_0 = \frac{2}{3H_0}$	$t_0 = \frac{1}{2H_0}$
$\rho = \frac{1}{6\pi G(1+w)^2}\frac{1}{t^2}$	$\rho = \frac{1}{6\pi G}\frac{1}{t^2}$	$\rho = \frac{3}{32\pi G}\frac{1}{t^2}$

Table 1.1: Dependencies obtained for the EdS Universe in three different cases: for a generic component (with EoS parameter w, *first column*), for a matter-dominated Universe, (with $w = 0$, *second column*) and for a radiation dominated Universe (with $w = 1/3$, *third column*).

1.4.2 Flat, open and closed models

Since we have already demonstrated that at different cosmic epochs different components (matter, radiation and Λ) can become dominant, we can assume that our Universe is entirely composed by only one type of fluid, at any time. We can consider this approximation valid in periods far from the moments of equivalences. A generic model that includes the hypothesis of mono-component fluid and that assumes a flat geometry ($\kappa = 0$) is called *Einstein-de Sitter Model* (EdS). In this model the equation (1.39) reduces to:

$$H(z) = H_0(1+z)^{\frac{3(1+w)}{2}} \; . \tag{1.41}$$

In Table 1.1 we reported a list of some useful dependencies derived assuming the EdS model. These relations are computed both for a generic fluid and for matter-dominated epoch and radiation-dominated epoch. The approximation of flat Universe can be considered accurate at high redshifts. In particular, considering a critical value z^*, defined as in the following equation:

$$|1 - \Omega_0| = \Omega_0(1+z^*)^{1+3w} \; , \tag{1.42}$$

we can see that, for $z \gg z^*$, equation (1.39) reduces to:

$$H(z) = H_0\sqrt{\Omega_0}(1+z)^{\frac{3(1+w)}{2}} \; .$$

This equation is similar to the solution found for EdS models, except for the factor $\sqrt{\Omega_0}$. So we can conclude that our Universe behaves as an EdS

Universe (thus with flat geometry) in young epochs. On the other hand, for $z \ll z^*$ the potential curvature of the Universe prevails, producing effects on the geometry of the Universe. In the case of an *open* model ($\kappa = 1$) the Universe will expand asymptotically at a constant rate, since gravity is not strong enough to stop the expansion. Therefore this type of Universe is destined to reach the thermal death, the so-called "Big Freeze". A *closed* model ($\kappa = -1$) is instead characterised by an inversion of the expansion that occurs at the instant t_M. After this moment the scale factor a begins to decrease, leading to the so-called "Big Crunch". The ultimate fate of a closed Universe is so to collapse in a second singularity, symmetrical in time with respect to the BB. figure 1.1 shows the possible evolutions of the parameter a for the scenarios of the Universe we have just described.

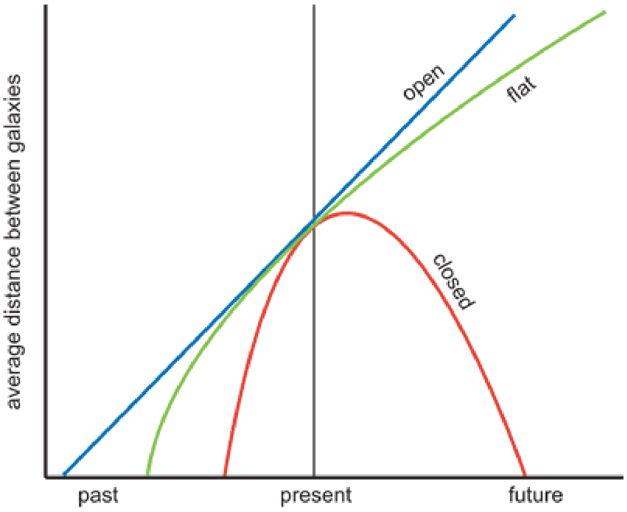

Figure 1.1: Evolution of the scale factor a as a function of time for three possible scenarios: open, flat and closed Universe. Credits to: `http://sci.esa.int/education/35775-cosmology/?fbodylongid=1706`

1.5 The Standard Cosmological Model

The ΛCDM is the cosmological model commonly accepted from the beginning of the 21^{st} century. This model is supported by a set of observational data and describes very well the large scale structures of the Universe. Moreover, the cosmological parameters with which it is defined are constantly constrained by experiments. It predicts also the existence of the *Cosmic Microwave Background* (CMB), which is the thermal radiation background with a temperature today of 2.726 ± 0.005 K, generated after the phenomenon of the recombination. This scenario establishes that the major components of the present-day Universe (so at $z = 0$) are the cosmological constant (Λ) and a dust component called Cold Dark Matter (CDM). The density of the radiative fluid, composed by all the relativistic particles (like photons and neutrinos), has a negligible contribute at $z = 0$. In particular, the density parameter of photons can be estimated by the measure of the temperature of the CMB and has a value of $\Omega_{0,r} \approx 10^{-5}$. The matter component is divided in two main typologies: baryonic and non-baryonic matter (i.e. DM). What discriminates between these components is their interactions. Both of them interact gravitationally, but only the ordinary baryonic matter can interact with observable electromagnetic radiation. Since it does not interact directly with photons, the detection of DM is extremely difficult and its direct observation impossible with standard experiments based on the emission of light. However, there are strong evidences of its existence, e.g. by the measures of the rotation curves of disk galaxies (Fuchs, 2001; Bosma, 1999) and of the velocity dispersion of elliptical galaxies (Loewenstein and White, 1998; Mamon and Łokas, 2005), by the gravitational anomalies found in galaxy clusters (Bradač, 2009), by the distortion of light during the phenomenon of gravitational lensing (Li et al., 2016; Wallis et al., 2017; Gilman et al., 2018) and by the analysis of the CMB's black body spectrum (Galli et al., 2011; Natarajan, 2013). Fritz Zwicky was the first scientist that, in 1937, proposed the existence of another kind of matter to explain the dynamics of galaxies in the Coma cluster (Zwicky, 1937). He found a discrepancy in the mass of the cluster estimated using luminosities and the measured velocity dispersion of the galaxies forming the cluster, and concluded that a quantity of DM should be present in a much greater density than luminous matter. Since the Zwicky's works of the 1930s, many studies have been done in order to understand the complex and elusive nature of DM. A large list of DM particle candidates have been proposed so far. Candidates for non-baryonic DM are hypothetical particles such as axions, sterile neutrinos, *weakly interacting massive particles* (WIMPs), *gravitationally-interacting massive particles* (GIMPs), or supersymmetric particles (Khlopov, 2017). Other candidates of DM are the *massive astrophysical compact halo objects* (MACHOs) (Alcock, 1997; Brandt, 2016): these objects, including neutron stars, and brown and white dwarfs, are composed of ordinary matter but do not emits significantly light. Other studies investigated new theories of modified gravity to describe the observations without having to assume any form of "additional" non-visible matter (for a review, see Clifton et al., 2012).

The idea of the cosmological constant was initially proposed by Albert Einstein (Einstein, 1915), but its reintroduction in the cosmological models was performed only in the 1990s, with the measure of the galaxy correlations on large scales (Efstathiou et al., 1990) and the final discovery of the accelerated expansion of the Universe, making use of type Ia supernovae as standard candles (Riess et al., 1998; Perlmutter et al., 1999). As consequence, the model of flat matter-dominated Universe was brought into question, and the DE component was introduced. Nowadays, the ΛCDM model is broadly accepted, but despite the refinements and the remarkable success it achieved, its theoretical roots still remain poorly understood. In particular, the real nature of DE and the physical origin of the accelerated expansion are still unknown.

To understand the effect of the cosmological constant Λ in the Universe, let us consider again the modified Einstein's field equation of GR, reported in equation (1.30). If we set $T_{\mu\nu} = 0$ in equation (1.31), the remaining term will represent the *energy of vacuum*, which acts as a repulsive force, opposite to the one of the gravity. In the ΛCDM model, Λ is defined as a constant and is described by a state parameter $w = -1$. From equation (1.39) it is possible to demonstrate that matter and radiation components have densities that evolve as $\propto (1+z)^3$ and $\propto (1+z)^4$, respectively. The value of the contribution of the Λ component to the density parameters remains instead constant throughout the expansion of the Universe, with a value of $\rho_\Lambda = \Lambda c^2/8\pi G$.

Let us now define the deceleration parameter as follows:

$$q(t) := -\frac{a(t)\ddot{a}(t)}{\dot{a}^2(t)} \equiv -\frac{1}{H^2(t)}\frac{\ddot{a}(t)}{a(t)} \ . \tag{1.43}$$

The deceleration parameter of a mono-component matter Universe ($w = 0$ and $p = 0$), from the First Friedmann Equation, is equal to $q = \Omega_M/2$, which implies $q > 0$. This corresponds to a decelerated expansion of the Universe, in contrast to the current observations. On the other hand, considering a multi-component model composed by matter and Λ, the First Friedmann Equation leads to:

$$\ddot{a} = -aH^2\frac{\Omega_M}{2} + aH^2\Omega_\Lambda \ ,$$

with $\Omega_\Lambda \equiv \Lambda c^2/3H(t)^2$. Now, from the definition of the deceleration parameter:

$$q = \frac{\Omega_M}{2} - \Omega_\Lambda \ .$$

To obtain an accelerated expansion ($q < 0$), we have to impose the condition:

$$\Omega_\Lambda > \frac{\Omega_M}{2} \ .$$

Inserting in the last formula the values of the parameters currently accepted ($\Omega_M \approx 0.3$ and $\Omega_\Lambda \approx 0.7$) we achieve a value of $q \approx -0.55$, so the condition imposed to have an accelerated expansion is satisfied. As confirmed by recent measurements, our Universe is approximately flat. In fact, summing the individual values of the density parameter Ω_{0,w_i}, we obtain $\sum_i \Omega_{0,w_i} \simeq 1$.

In Subsection 1.4.2 we stated that the early Universe is well described by an EdS model, so with $\ddot{a} < 0$. Having established now that in recent times the Universe is experiencing an accelerated expansion, $\ddot{a} > 0$, we must admit the presence of a flex in the function $a(z)$, corresponding to an inversion of the expansion rate. It can be easily demonstrated that this change of expansion rate occurs at $z_f \approx 0.7$. Instead, the moment corresponding to the equivalence between matter and cosmological constant $\Omega_M(z_{eq,\Lambda}) = \Omega_\Lambda(z_{eq,\Lambda})$, coincides with $z_{eq} \approx 0.33$. This result implies that DE and DM are currently of the same order of magnitude and that the contribution of the cosmological constant became relevant only at recent times. This is what is generally called the cosmological *Coincidence Problem*.

1.6 The Jeans Theory

In 1902, Jeans demonstrated how the existence of an instability in evolving clouds of gas can lead to the formation of galaxies and large-scale structure, currently observed in the Universe. According to his theory (called *gravitational Jeans instability* or simply *Jeans Theory*), the small inhomogeneities present in the fluid are amplified and can evolve in time, when the internal gas pressure is unable to counteract the gravitational pull.

From the current observations, the Universe appears to be quite inhomogeneous at Mpc scales and shows the characteristics of a highly non-linear evolution. On scales of collapsed objects, fluctuations of density are on average approximately of 10^2. However, from the amplitude of the fluctuations in the temperature power spectrum it is possible to derive the amplitude of the density perturbations in the cosmic fluid at the time of recombination. In particular:

$$\frac{\delta T}{\overline{T}} \approx 10^{-5} ,$$

where $\overline{T}$ is the mean black body temperature of the CMB. Therefore we can conclude that the amplitude of the density fluctuations were very small in this epoch and the Universe was almost homogeneous. The effect of gravity must be such as to make the already existing perturbations grow with a sufficient rate. The overdense regions of the Universe are capable to attract matter, which, in turn, is evacuated from the underdense ones creating increasingly larger voids. The Jeans theory provides an analytical description of this phenomenon, as long as the structures analysed remain in the linear regime. To describe the behavior of the collapsed matter in non-linear regime, we generally rely on the numerical simulations, since its analytical treatment becomes very complex.

The aim of the Jeans theory is therefore to describe of how fast an initial perturbation has to grow to reproduce the inhomogeneities observed today. The results derived in this theory are applied to non-relativistic matter and on scales not exceeding the cosmological horizon, that represents the sphere that comprehends all the volume of the Universe that is casually connected with an observer. The cosmological horizon is defined as:

$$R_H \equiv a(t) \int_{t_{BB}}^{t} \frac{c\ \mathrm{d}t'}{a(t')}\ , \tag{1.44}$$

where time $t_{BB} = 0$ identifies the beginning of the expansion with the Big Bang. The cosmological horizon separates the Universe in two different regions: on scales beyond R_H gravity is the only force in action and the growth of the perturbation has to be treated with the relativistic theory, while on smaller scales the Jeans theory provides a reliable description of this phenomenon in an expanding Universe. Since on scales larger than R_H there are no relevant forces except gravity, the density fluctuations can always grow, giving birth to collapsed structures.

The Jeans Theory describes the dynamic and the evolution of a self-gravitating fluid. In the next section we will start studying the case of a collisional gas in a static background and subsequently we will extend the description to the scenario of the expanding Universe, towards the non-linear regime.

1.6.1 Jeans instability in a Static Universe

We assume a homogeneous and isotropic background, composed by a fluid having a constant matter density $\rho(\mathbf{x}, t)$ embedded in a static (non-expanding) Universe. The equations of motion of such a fluid, in the Newtonian approximation, are the following:

$$\frac{\partial \rho}{\partial t} + \nabla \cdot (\rho \mathbf{v}) = 0 \qquad \text{continuity equation} \tag{1.45a}$$

$$\frac{\partial \mathbf{v}}{\partial t} + (\mathbf{v} \cdot \nabla)\mathbf{v} = -\frac{1}{\rho}\nabla \rho - \nabla \Phi \qquad \text{Euler equation} \tag{1.45b}$$

$$\nabla^2 \Phi = 4\pi G \rho \qquad \text{Poisson Equation} \tag{1.45c}$$

$$p = p(\rho, S) = p(\rho) \qquad \text{equation of state} \tag{1.45d}$$

$$\frac{\mathrm{d}S}{\mathrm{d}t} = 0 \qquad \text{adiabatic condition} \tag{1.45e}$$

where $\mathbf{v}$ is the velocity vector of a fluid element, Φ is the gravitational potential, p the pressure and S represents the entropy. Let us suppose a generic background solution for the set of Equations (1.45):

$$\begin{cases} \rho_B = const \\ p_B = const \\ \Phi_B = const \\ \mathbf{v} = 0 \end{cases} . \tag{1.46}$$

We can now define the dimensionless density perturbation, the so-called *density contrast*:

$$\delta(\mathbf{x}, t) \equiv \frac{\delta\rho(\mathbf{x}, t)}{\rho_B} . \tag{1.47}$$

Introducing a small perturbation δ in each variable of the system (1.45), thus:

$$\begin{cases} \rho = \rho_B + \delta\rho \\ p = p_B + \delta p \\ \Phi = \rho_B + \delta\Phi \\ \mathbf{v} = \delta\mathbf{v} \end{cases} \tag{1.48}$$

and imposing $\delta \ll 1$ for all perturbations we can obtain the hydrodinamic system for a fluctuation in the density field that can be linearised. We made the request that both the systems (1.46) and (1.48) are the solution of the initial Equations (1.45). The solving equation for density becomes a differential equation which in Fourier space has the form:

$$\ddot{\delta_\mathbf{k}} + (k^2 c_s^2 - 4\pi G \rho_B)\delta_\mathbf{k} = 0 \tag{1.49}$$

where $k = |\mathbf{k}|$ represents the absolute value of the wavenumber, $\delta_\mathbf{k} = \delta_k(t)$ is the Fourier transform of $\delta(\mathbf{x}, t)$ and $c_s = \sqrt{\partial p / \partial \rho}$ is the sound speed. The previous differential equation has two independent solutions, with the form:

$$\delta_\mathbf{k} \propto \exp(\pm i \omega t) , \tag{1.50}$$

where

$$\omega(k) = \sqrt{k^2 c_s^2 - 4\pi G \rho_B} \ . \tag{1.51}$$

The solutions are of two types, according to the value of the wavelength $\lambda = 2\pi/k$ with respect to the *Jeans length*:

$$\lambda_J \equiv \frac{2\pi}{k} = c_s \left(\frac{\pi}{G\rho_B} \right)^{1/2} \ . \tag{1.52}$$

If $\lambda < \lambda_J$ we obtain $w^2(k) > 0$, so the perturbation propagates as a sound wave with constant amplitude and with a phase velocity $c_{ph} = \omega/k$, that tends to become equal to c_s for $\lambda \ll \lambda_J$. On the other hand, for $\lambda > \lambda_J$ the pulsation becomes imaginary and the solution is a stationary (non-propagating) wave with an amplitude that increases or decreases exponentially. Of these two solutions, we are interested to the increasing one, which can lead to the collapse of the perturbation and the formation of the structures. In the end, for very large scales ($\lambda \gg \lambda_J$), gravity dominates and the fluctuation grows rapidly with an exponential behavior, tending to a *free-fall collapse* with typical time $\tau_{ff} \sim 1/\sqrt{G\rho_0}$. Summarising, according to the Jeans Theory, the density fluctuations below the Jeans scale, λ_J, propagate as a wave of constant amplitude, while the ones on sufficiently larger scales can grow exponentially.

1.6.2 Jeans instability in an expanding Universe

Now we want to analyse the case of a perturbation embedded in an expanding homogeneous and isotropic Universe. In this framework the background density is a function of time, $\rho_B = \rho_B(t)$, so the continuity equation (1.45a) becomes:

$$\dot{\rho_B} + 3H(t)\rho_B = 0 \ . \tag{1.53}$$

Moreover the velocities are no longer null, since the fluid has a peculiar velocity and it is also subjected to the Hubble flow. Therefore we obtain a double component velocity with the form:

$$\mathbf{u} = \dot{\mathbf{x}} = H(t)\mathbf{x} + v_p \ , \tag{1.54}$$

where $\mathbf{x}$ indicates the position vector of the fluid. Now, introducing a fluctuation in the set of Equations (1.45) in the same way described in the previous section, it is possible to recover the solution for every Fourier mode of the type $\delta = \delta_{\mathbf{k}}(t) \exp(i\mathbf{k}\mathbf{x})$:

$$\ddot{\delta_{\mathbf{k}}} + 2H(t)\dot{\delta_k} + (k^2 c_s^2 - 4\pi G\rho_B)\delta_{\mathbf{k}} = 0 \ . \tag{1.55}$$

The last equation is the so-called *dispersion relation*, where the term $2H(t)\dot{\delta}_k$ is related to the Hubble friction, while the term $k^2c^2\delta_{\mathbf{k}}$ accounts for the characteristic velocity field of the fluid. Both these terms tend to dissipate the fluctuations, hampering their growth. This is a second-order differential equation for $\delta(\mathbf{x}, t)$ and we can separate the behavior of its solutions depending on the scale:

$$\lambda_J \simeq c_s \left(\frac{\pi}{G\rho_B} \right)^{1/2} \quad . \tag{1.56}$$

For $\lambda < \lambda_J$ the fluctuation propagate as stationary waves, as we previously found for a static Universes. On the other hand, for $\lambda > \lambda_J$ the dispersion relation has growing and decaying mode solutions:

$$\delta(\mathbf{x}, t) = A(\mathbf{x})D_+(t) + B(\mathbf{x})D_-(t) \ , \tag{1.57}$$

where A and B are two functions depending on the comoving coordinates, while D_+ and D_- represent respectively the growing and decaying modes and are time-dependent. Applying now the dependencies for EdS Universes reported in Table 1.1 (with $\Omega_M = 1$) we obtain the following trends:

$$D_+(t) \propto t^{2/3} \propto a(t)$$

and

$$D_-(t) \propto t^{-1} \propto a^{-3/2} \ .$$

We are interested to the growing solution, since the decaying one does not give rise to gravitational instability.

For a generic Universe, the growing solution has an integral form given by the following equation:

$$D_+(z) = H(z) \int_z^{\infty} \frac{\mathrm{d}z'(1+z')}{H^3(z')} \quad . \tag{1.58}$$

The previous integral has no analytical solution. We can provide a parametric solution to approximate its trend:

$$f = \frac{\mathrm{d}\log D_+}{\mathrm{d}\log a} \simeq \Omega_M^{0.55} + \frac{\Omega_\Lambda}{70} \left(1 + \frac{1}{2}\Omega_M \right) \quad . \tag{1.59}$$

From this formula we can see that there is a strong dependence on the quantity of matter present in the Universe, while we can conclude that Λ does not play a crucial role for the growth of the fluctuations.

1.6.3 Primordial density fluctuations

In the previous section we have studied the linear evolution of a single perturbation of the density field $\delta(\mathbf{x},t) = D_+(t)\delta(\mathbf{x})$. This representation is useful because a generic perturbation can be represented in Fourier space as a superposition of such plane waves, that have the advantage to be independent during the evolution. In more realistic cases we expect fluctuations to exist on a variety of mass or length scales, so the final collapsed structures will depend on the growth of perturbations on different scales relative to each other. This approach requires a statistical treatment of the initial perturbations.

The spatial Fourier transform of $\delta(\mathbf{x})$ has the form:

$$\delta(\mathbf{k}) = \frac{1}{(2\pi)^3}\int \mathrm{d}^3\mathbf{x}^{-i\mathbf{k}\cdot\mathbf{x}}\delta\mathbf{x} \ . \tag{1.60}$$

Let us define the *Power Spectrum* of the density field as the variance of the amplitudes at a given value of $\mathbf{k}$:

$$\langle\delta(\mathbf{k})\delta^*(\mathbf{k}')\rangle = (2\pi)^3 P(k)\delta_D^{(3)}(\mathbf{k}-\mathbf{k}') \ , \tag{1.61}$$

where $\delta_D^{(3)}$ is the 3-dimensional Dirac delta function and $\delta^*(\mathbf{k}) = \delta(\textbf{-k})$ because of the reality of δ. The power spectrum is related via a Fourier transform to its analogous quantity in the real space, the *two-point correlation function* (2PCF) $\xi(r)$:

$$\xi(r) = \frac{1}{(2\pi)^3}\int \mathrm{d}^3\mathbf{k}P(k)e^{i\mathbf{k}\cdot\mathbf{x}} \ , \tag{1.62}$$

which quantifies the spatial clustering of the objects and it is defined as:

$$\langle\delta(\mathbf{x})\delta(\mathbf{x}')\rangle = \xi(|\mathbf{x}-\mathbf{x}'|) = \xi(\mathbf{r}) = \xi(r) \ , \tag{1.63}$$

where r is the comoving distance between $\mathbf{x}$ and $\mathbf{x}'$, and $\xi(\mathbf{r}) = \xi(r)$ is due to the CP. We can interpret $\xi(r)$ also as the probability excess $\mathrm{d}P_{12}$ of finding a pair of objects separated by a comoving distance $\mathbf{r}$, in two independent volume elements $\mathrm{d}V_1$ and $\mathrm{d}V_2$, with respect to a random uniform distribution of objects:

$$\mathrm{d}P_{12} = n^2[1+\xi(r)]\mathrm{d}V_1\mathrm{d}V_2 \ . \tag{1.64}$$

According to the inflation models[1], the primordial density perturbations are generated by stochastic quantum fluctuations in a scalar field (i.e *inflaton*)

---

[1] The inflation theory predicts a phase of exponential expansion of the Universe, set in the early stages after the BB. For further information, see Guth (1981).

(Guth and Pi, 1982), therefore their amplitudes are described by a Gaussian distribution. With this assumption, the power spectrum defines uniquely the distribution of fluctuations. Since during the inflation there is no preferred scale, the initial spectrum follows a power law given by:

$$P(k) = Ak^n \ , \tag{1.65}$$

where the spectral index n is generally assumed to be close to unity (Zeldovich, 1972). While the shape of the power spectrum can be considered to be fixed, the amplitude A is not and has to be constrained with observations. In particular, the most reliable measure of A is obtained from the analysis of the temperature fluctuations in the CMB.

Since the amplitudes of the fluctuations have a Gaussian distribution in real space, the mean value of perturbations is statistically null by definition. Instead, its variance σ^2 is defined by:

$$\sigma^2 = \langle|\delta(\mathbf{x})^2)|\rangle = \sum_{\mathbf{k}} \langle|\delta_{\mathbf{k}}|^2\rangle = \frac{1}{V_u}\sum_{k} \delta_k^2 \ , \tag{1.66}$$

where the average is taken over an ensemble of realisations of volume V_u. By considering the limit $V_u \to \infty$ and assuming the validity of the CP, we obtain:

$$\sigma^2 \to \frac{1}{2\pi^2}\int_0^\infty P(k)k^2 \mathrm{d}k \ . \tag{1.67}$$

Since in the previous equation the variance is defined for each point of the space, to measure σ^2 it is necessary to reconstruct the entire density field, which is obviously not possible in practice. Therefore it is convenient to describe the fluctuation field "filtering" on some resolution scale R, instead of using a punctual variance.

Let us define $\langle M\rangle$ as be the mean mass found inside a spherical volume of radius R. In this way we can recover the density fluctuation from a discrete distribution of tracers as:

$$\delta_M = \frac{M - \langle M\rangle}{\langle M\rangle} \ . \tag{1.68}$$

Using this definition in combination with equation (1.66), we obtain the *mass variance*:

$$\sigma_M^2 = \langle\delta_M^2\rangle = \frac{\langle(M - \langle M\rangle)^2\rangle}{\langle M\rangle^2} \ , \tag{1.69}$$

which is related to the convolution of the punctual density with a *window function* W of radius R (corresponding to M):

$$\delta_M(\mathbf{x}) = \delta(\mathbf{x}) \otimes W(\mathbf{x}, R) \ . \tag{1.70}$$

From the last two equations and using the convolution theorem, it is possible to express the mass variance, passing in the limit expressed by the equation (1.67):

$$\sigma_M^2 = \frac{1}{(2\pi)^3}\int \mathrm{d}^3\mathbf{k}P(k)\hat{W}^2(\mathbf{k},R)\ , \tag{1.71}$$

where $\hat{W}$ is the Fourier-transform of the window function and which is a function of R and therefore of M. We can also note that:

$$\begin{cases} \sigma_M^2 \to \sigma^2 & \text{for } R \to 0 \\ \sigma_M^2 \to 0 & \text{for } R \to \infty\ , \end{cases} \tag{1.72}$$

that is, smaller is the scale R we use to filter more the variance tends to its punctual value. On the other hand, filtering on larger scales, the density fluctuations are more and more smoothed and the Gaussian distribution of their amplitude tends to degenerate into a Dirac delta function, having so a null variance. σ_M^2 is therefore dominated by perturbation components with wavelength $\lambda \simeq k^{-1} > R$, since the higher values of k tend to be averaged out within the window volume. The *Zel'dovich spectrum* defined in equation (1.65) (with $n = 1$) is a growing function of k, which means that waves with large λ have a small contribute.

1.6.4 Spherical evolution

In the previous sections we studied the evolution of a primordial density perturbation. This is described by the Jeans theory, which preserves its validity until $\delta(\mathbf{x}, t) \ll 1$. Since the large-scale structures of the Universe are characterised by a wide range of degrees of non-linearity, the Jeans theory fails in the reconstruction of their entire evolution. Nevertheless, analytical solutions exist in the case of a *isolated spherically symmetric* perturbation. This is the simplest approach to the non-linear evolution and it requires the assumption that the perturbation is spherical. This treatment is not particularly interesting for the reconstruction of the evolution of structures like galaxies or galaxy clusters because the real fluctuations are expected to be highly irregular and random, but it constitutes a valid model for the study of cosmic voids (see chapter 2).

Let us consider a spherical top-hat perturbation. We can model it as a set of concentric shells, uniform and without substructures. An important feature of this case is that the evolution of the perturbation only depends on the total energy embedded in the shell, on its peculiar velocity, and not on the radial distribution of the density field inside it (Sheth and van de Weygaert, 2004).

At some initial time t_i, the mean density field of the background Universe determines the subdivision of the volume of the Universe in *overdense* $\delta(\mathbf{x}, t_i) > 0$, and *underdense* $\delta(\mathbf{x}, t_i) < 0$ regions. We expect that, if a perturbation has a sufficiently high density contrast, it will decouple from the Hubble flow and collapse. On the other hand, an underdensity is subject to a repulsive effect of the gravity, that leads to the expansion of the perturbation, which will be intensified by the Hubble flow. So, an underdense shell will expand faster than the Hubble flow, evacuating the matter content outward.

Assuming one more time the validity of the CP, we can suppose that each perturbation can be treated as an independent Friedmann Universe, until it evolves adiabatically. So the only interaction we have to take into account is the gravitational one.

The initial density distribution of our model can be expressed as follows:

$$\rho(r, t_i) = \rho_B(t_i) + \delta\rho(r_i, t_i) = \rho_B(t_i)[1 + \delta_i(r)] \ , \tag{1.73}$$

where $\delta_i(r) \equiv \delta(r, t_i)$ is the initial density contrast embedded in the shell. Since we are dealing with a spherical perturbation, it is convenient to make use of the proper radial coordinate $r = a(t)|\mathbf{x}|$, where $\mathbf{x}$ is the comoving coordinate.

Let us consider a concentric shell of infinitesimal thickness at distance r from the centre. The motion of the matter included in this shell can be described by the following equation:

$$\frac{\mathrm{d}^2 r}{\mathrm{d}t^2} = -\frac{GM}{r^2} = -\frac{4\pi G}{3}\rho(1 + \Delta)r \ , \tag{1.74}$$

where

$$M = \frac{4\pi}{3} r_i^3 \rho_B (1 + \Delta_i) \ , \tag{1.75}$$

$$\Delta_i = \frac{3}{r_i^3} \int_0^{r_i} \delta_i(r) r^2 \mathrm{d}r \ , \tag{1.76}$$

with r_i the initial radius of the shell with enclosed mass M and Δ_i the average value of δ_i within r_i at time t_i. Equation (1.76) is analogous to the First Friedmann Equation (1.23) for an Universe formed by only one component:

$$\frac{\mathrm{d}^2 a}{\mathrm{d}t^2} = -\frac{4\pi G}{3}\rho_B a \ , \tag{1.77}$$

thanks to the similarity of these two equations we can conclude that the perturbation evolves fundamentally like a Universe of a different mean density, but preserving the same expansion rate.

From equation (1.74), the first integral of motion can be written as:

$$\frac{1}{2}\left(\frac{\mathrm{d}r}{\mathrm{d}t}\right)^2 - \frac{GM}{r} = \frac{1}{2}\left(\frac{\mathrm{d}r}{\mathrm{d}t}\right)^2 - \frac{4\pi G}{3}\rho_B(1+\Delta)r^2 = E \ , \tag{1.78}$$

where E is the total energy of the perturbation. From the previous equation we can conclude that the value of E determines the fate of the given mass shell. In fact, if $E < 0$, r increases and $\dot{r}$ will eventually become zero and later negative. This will lead to the collapse of the perturbation. On the other hand, if $E > 0$, then $\dot{r}^2$ will always be positive and the shell will expand forever, decoupling from the Hubble flow.

Analogously to what we found for before, equation (1.78) can be compared to the Second Friedmann Equation (1.24):

$$\frac{1}{2}\left(\frac{\mathrm{d}a}{\mathrm{d}t}\right)^2 - \frac{4\pi G}{3}\rho_B a^2 = -\frac{K}{2} \ , \tag{1.79}$$

which describes the expansion rate of the Universe. The constant K, as we have seen in section 1.2, is the curvature parameter. Note that equation (1.79) is obtained from the First Friedmann Equation (1.23) applying the adiabatic condition (1.27).

Having established these similarities, we can proceed deriving the parametric solutions of the Friedmann equations for curved universes. The parametric solutions relative to a mass shell are the following:

$$r = A(\cosh\theta - 1) \ , \qquad t = B(\sinh\theta - \theta) \ , \qquad E > 0; \tag{1.80a}$$

$$r = A(1 - \cos\theta) \ , \qquad t = B(\theta - \sin\theta) \ , \qquad E < 0; \tag{1.80b}$$

where the constants A and B related by:

$$A^3 = GMB^2 \ . \tag{1.81}$$

The parameter θ is called *development angle* and it parameterises all the physical relevant quantities relating to the mass shell.

Let us assume a homogeneous background has we have done in the Jeans theory. We choose the expansion parameter $a(t) = r_B(t)$ so that it encloses the same mass M as in equations (1.80). Therefore we obtain:

$$r_B = A_B(\cosh\eta - 1) \ , \qquad t = B_B(\sinh\eta - \eta) \ , \qquad K > 0; \tag{1.82a}$$

$$r_B = A_B(1 - \cos\eta) \ , \qquad t = B_B(\eta - \sin\eta) \ , \qquad K < 0; \tag{1.82b}$$

where A_B and B_B are two constants related by:

$$A_B^3 = GMB_B^2 \ . \tag{1.83}$$

The solutions for the EdS Universes (equivalent to the case $E = 0$) are the same we reported in Table 1.1.

We can now calculate the mean density inside a shell applying $\rho = 3M/(4\pi r^3)$ and substituting with the dependencies in system (1.80) and in equation (1.83), we obtain

$$\rho(r,t) = \begin{cases} \frac{3}{4\pi G t^2}\frac{(\sinh\zeta-\zeta)^2}{(\cosh\zeta-1)^3} & \text{open} \\ \frac{3}{4\pi G t^2}\frac{2}{9} & \text{critical} \\ \frac{3}{4\pi G t^2}\frac{(\zeta-\sin\zeta)^2}{(1-\cos\zeta)^3} & \text{closed} \end{cases} . \tag{1.84}$$

The density contrast of a perturbation in a monocomponent Universe can be expressed in the most general form with the following expression:

$$1 + \Delta(r,t) = \frac{\rho(r,t)}{\rho_B(r,t)} = \frac{f(\theta)}{f(\eta)} \tag{1.85}$$

where θ and η are the development angles of the perturbation and of the background Universe, respectively. We can define the *cosmic density function* $f(\zeta)$ as:

$$f(\zeta) = \begin{cases} \frac{(\sinh\zeta-\zeta)^2}{(\cosh\zeta-1)^3} & \text{open} \\ \frac{2}{9} & \text{critial} \\ \frac{(\zeta-\sin\zeta)^2}{(1-\cos\zeta)^3} & \text{closed} \end{cases} . \tag{1.86}$$

In addiction, the velocity of expansion or contraction of a spherical shell can be expressed in terms of θ and η. Let us consider the peculiar velocity of a shell:

$$v_p(r,t) = v(r,t) - H(t)r(t) \ , \tag{1.87}$$

where $v(r,t)$ represents the total velocity of the shell and $H(t)$ the Hubble parameter of the background Universe. Now we define a general Hubble parameter H_s for an unspecified shell with the following equation:

$$H_s(t) = \frac{\dot{r}}{r} = \frac{1}{r}\frac{\mathrm{d}r}{\mathrm{d}t} = \frac{1}{t}g(\zeta) \ , \tag{1.88}$$

where $g(\zeta)$ is the *cosmic velocity function* and it is defined as:

$$g(\zeta) = \begin{cases} \frac{\sinh\zeta(\sinh\zeta-\zeta)}{(\cosh\zeta-1)^2} & \text{open} \\ \frac{2}{3} & \text{critial} \\ \frac{\sin\zeta(\zeta-\sin\zeta)}{(1-\cos\zeta)^2} & \text{closed} \end{cases} . \tag{1.89}$$

The peculiar velocity expressed in equation (1.87) can then be rewritten as

$$v_p(r,t) = H(t)r(t)\left[\frac{g(\theta)}{g(\eta)} - 1\right] . \tag{1.90}$$

With the equations (1.85) and (1.90) we obtained explicit expressions for the evolution of a spherical perturbation in FRW backgrounds, without taking into to account the effect of the cosmological constant. In the next sections we will analyse the case of a spherical overdense and underdense perturbation, evolving in an EdS background Universe.

Overdensities

Let us consider the evolution of an initially overdense shell in a EdS Universe. Such a shell will initially expand slower than the Hubble flow. Then it will gradually halts its expansion, reaching a maximum radius r_m. After this instant, t_{ta}, it turns around and it starts to collapse. Since at the moment of turn-around the velocity of the shell is $v(r_m, t_{ta}) = 0$, for the closed case equation (1.89) gives a velocity equals to:

$$v(r,t) = H_s(r,t) r(t) \propto \frac{\sin\theta}{1-\cos\theta} \ . \tag{1.91}$$

From the relation in equation (1.91) we obtain that at the turn-around $\theta_{ta} = \pi$, the resulting density is:

$$1 + \Delta(r_m, t_{ta}) = (3\pi/4)^2 \approx 5.6 \ , \tag{1.92}$$

which is highly non-linear and implies the shell has expanded by a factor of $5.6^{1/3} \approx 1.8$ with respect to its initial value. The last relation suggests that, at the moment of turn-around, the collapsing region is nearly 6 times denser than the background Universe. This corresponds to a density contrast of $\Delta \approx 4.6$ which is already in the non-linear regime. Now it is useful to calculate the corresponding value of Δ in linear regime. For a spherical overdensity with initial peculiar velocity $v_p(t_i) = 0$ in an EdS Universe, we need to consider both the growing ($D_+ \propto t^{2/3}$) and decaying ($D_- \propto t^{-1}$) mode, in order to describe the evolution of the density contrast:

$$\delta = \delta_+(t_i)\left(\frac{t}{t_i}\right)^{2/3} + \delta_-(t_i)\left(\frac{t}{t_i}\right)^{-1} \ , \tag{1.93}$$

where $\delta_\pm(t_i)$ are the growing (+) and decaying (−) fraction of the initial perturbation δ_i.

Now we can reasonably assume that the decaying mode will become negligible after a short time. Then the remaining perturbation is $\delta \approx \delta_+(t_i)$. Therefore, in linear approximation, the *turn-around density contrast* is:

$$\delta_{ta} = \frac{3}{5}\left(\frac{3\pi}{4}\right)^{2/3} \approx 1.062 \ . \tag{1.94}$$

Full collapse is instead associated with $\theta = 2\pi$ and the linearly extrapolated initial overdensity reaches the *collapse density contrast* at the value:

$$\delta_c = \frac{3}{5}\left(\frac{3\pi}{2}\right)^{2/3} \approx 1.686 \ . \tag{1.95}$$

Nevertheless, even though a strictly gravitational description implies that the comoving radius of the overdensity shrinks to zero ($r(2\pi) = 0$), in reality the matter in the collapsing object will eventually virialise. In fact, the more at smaller radii, the approximation of independently evolving shells can be considered valid anymore. The hydrodynamical interactions (for the baryonic matter) or the increase of the dispersion velocity of the particles (for the DM) within the shell will lead towards an equilibrium configuration. Therefore, it is usual to assume that the final size of a collapsed spherical object corresponds to its virial radius.

Underdensities

The evolution of an underdense spherical region is different from that of its overdense counterpart. We can generally define these regions as *voids*. In this case, the net radial acceleration is directed outward with respect to the centre of the sphere and it is directly proportional to the mean density contrast $\Delta(r, t)$ of the void. Since the inner shells are more underdense, they are affected by a stronger outward acceleration than the outer shells.

In the case of an EdS model ($\Omega = 1$), we can obtain the evolution of the density from equation (1.85):

$$1 + \Delta(r, t) = \frac{f_{open}(\theta)}{f_{EdS}(\eta)} = \frac{9}{2}\frac{(\sinh\theta - \theta)^2}{(\cosh\theta - 1)^3} \ . \tag{1.96}$$

Once again, we want to compare this result to the corresponding linear initial density deficit $\Delta^L(r, t)$:

$$\Delta^L(r, t) = \Delta^L(z) = \frac{\Delta_i}{1 + z} = \frac{1}{1 + z}\left(\frac{3}{5}\Delta_{+,i} + \frac{2}{5}\Delta_{-,i}\right) \approx \frac{3}{5}\frac{\Delta_{+,i}}{1 + z} \ , \tag{1.97}$$

where we considered only the growing solution $\Delta_{+,i}$, since the decaying solution $\Delta_{-,i}$ gradually tends to zero.

The constants in equation (1.80) are:

$$A = \frac{r_i}{2\Delta_i} \ , \tag{1.98}$$

$$B = \frac{3}{4}\frac{t_i}{\Delta_i^{3/2}} \ , \tag{1.99}$$

where r_i and t_i represent the initial coordinates of the perturbation (Blumenthal et al., 1992). Equation (1.97), with the equations (1.98) and (1.99) and considering also the solutions from Table 1.1, leads to:

$$\Delta_i^L(\theta) = -\left(\frac{3}{4}\right)^{2/3} \frac{3}{5}(\sinh\theta - \theta)^{2/3} \ . \tag{1.100}$$

A direct consequence of the differential outward expansion and of the radial decrease of the expansion rate, is the accumulation of shells near the boundary of the void. The density deficit $\Delta(r)$ of the void decreases as a function of radius r and reaches its minimum at the centre. Shells that were initially close to the centre will ultimately catch up the shells further outside, until they eventually pass them. This marks the phenomenon called *shell-crossing*. The shell-crossing defines a characteristic moment that defines the formation of the void at a non-linear level.

For an ideal top-hat underdensity, this process also leads to the formation of an infinitely dense ridge in the outermost region of the void. From this moment on the evolution of the void can be described by a self-similar outward moving shell (Suto et al., 1984).

The solutions in equation (1.80) represent a family of trajectories labeled by r_i and parameterised by θ. We can find out the position and the moment in which shell-crossing first occurs by differentiating the parametrised solutions with respect to r and θ, and requiring that $\mathrm{d}r$ and $\mathrm{d}t$ vanish:

$$\begin{bmatrix} A_{11} & A_{12} \\ A_{21} & A_{22} \end{bmatrix} \begin{bmatrix} \mathrm{d}r/r \\ \mathrm{d}\theta \end{bmatrix} = 0 \ , \tag{1.101}$$

where A_{ij} are functions of Δ_i and θ (Jennings et al., 2013). The homogeneous system of linear equations (1.101) has non-zero solutions when $\det A = 0$, thus the shell-crossing condition is:

$$\frac{\sinh\theta_{sc}(\sinh\theta_{sc} - \theta_{sc})}{(\theta_{sc} - 1)^2} = \frac{8}{9} \ . \tag{1.102}$$

Therefore shell-crossing first occurs at a development angle $\theta_{sc} \approx 3.49$. In addiction we can note that, from equation (1.88) and from the relation (1.102), at shell-crossing the void has a fixed excess Hubble expansion rate: $H_{sc} = (4/3)H(t_{sc})$.

Substituting θ_{sc}, we can now obtain all the relevant values to deal with voids. As first, the non-linear (NL) density contrast is given by equation (1.85):

$$1 + \delta_v^{NL}(r, t) \approx 0.21 \ . \tag{1.103}$$

It follows that $|\delta_{sc}| \approx 0.8 \lesssim 1$, which means that a void is only nearly non-linear. This is due to the fact that there is a physical limit, $(\delta\rho/\rho)_{lim} = -1$, to the underdensity degree that a region can reach. An underdensity which evolved towards shell-crossing, has expanded by a factor $(1+\delta_{sc}^{NL})^{1/3} \approx 1.72$ with respect to its initial size.

In the end, from equation (1.100) we obtain the linearly extrapolated underdensity of a void:

$$\delta_v \approx -2.71 \ , \tag{1.104}$$

which is the underdense counterpart of the threshold found in equation (1.95).

Icke (1984) demonstrated that voids tend to assume a spherical form, differently from collapsing objects, which tendentially evolve into filamentary or sheet-like structures. Moreover, since the expansion of a void can be considered as the time reversal of the collapse of an overdensity, it follows that, in the underdense case, the eventual initial asphericities are cancelled.

1.6.5 Non-linear evolution

The cosmic structures present in today's Universe, such as galaxies, clusters and DM haloes, are the result of gravitational instabilities occurred throughout the cosmological history. In order to describe the formation of these objects the the small-perturbations approximation can not be applied anymore, since they are characterised by a strongly non-linear regime given by $\delta \gg 1$. After the linear regime breaks down, therefore when δ becomes comparable to unity, the weakly non-linear (WNL) regime sets in. Already in the WNL stage, the fluctuation distribution function starts to deviate from the Gaussian shape. Even if some approximated analytical models have been proposed to describe what happens during this phase, we generally rely on N-body simulations in order to model accurately non-linear regimes.

Moreover, we have to take into account that also the spatial distribution of baryons changes during the history of the Universe. Its evolution is different from the DM one, because of several further phenomena. For example as a result of hydrodynamical effects, star formation, SNe's explosion, AGN's feedback. All of these phenomena make it difficult to construct a full and solid theory. An alternative solution to the development of semi-analytical models to describe these effects, is to assume that the discrete distribution of objects (as galaxies, clusters or haloes) $n(\mathbf{r}) = \sum_i \delta_D^{(3)}(\mathbf{r} - \mathbf{r}_i)$ is connected by a simple functional relationship to the underlying DM $\delta(r)$. It is generally believed that relative fluctuations in the object number counts and matter density fluctuations are proportional to each other, at least on sufficiently large scales. This is expressed by the following relation:

$$\frac{\delta n(\mathbf{r})}{\langle n \rangle} = b \frac{\delta \rho(\mathbf{r})}{\langle \rho \rangle} \ , \tag{1.105}$$

where the factor b is called the *linear bias parameter* and it quantifies the difference between mass and object (e.g. galaxy) clustering. Assuming this approximation, the linear theory can be extended on large scales to relate galaxy clustering statistics to those of the underlying density fluctuations, by means of $\sigma_g^2 = b^2 \sigma_M^2$.

It can be demonstrated that the effective bias has a direct dependency on the mass and the redshift of the cosmological objects. This can be explained by considering the decomposition of the density field of the Universe in short and long wavelengths. In particular, the formation of the structures occurs when a given density threshold is exceeded, therefore on those scales characterized by a peak of the long wavelength. This can be interpreted as the tendency of the more massive objects of being more clustered. Then, given the hierarchical formation of the structures, the massive objects were rarer in the past, they appear more clustered at higher redshifts. The accurate prediction of the value of b as a function of the mass M and the redshift z of the DM haloes can be obtained with analytical treatments, which lead to the formula:

$$b(M, z) := \sqrt{\frac{\xi_{halo}(r, z, M)}{\xi(r, z)}} = 1 + \frac{1}{\delta_c} \left(\frac{\delta_c^2}{\sigma_M^2 D_+^2} - 1 \right) \ , \tag{1.106}$$

where $\delta_c = 1.686$ is the critical linear overdensity, σ_M is the mass variance and D_+ is the growing factor, expressed in equation (1.58). (Mo and White, 1996). We will give a more complete description of these arguments in chapter 4.

1.6.6 The Zel'dovich approximation

The Zel'dovich approximation can be used to extend the linear theory to the weakly non-linear regime (i.e. to the case of density perturbations slightly larger than unity). It provides a good representation for structures that have not reached the full non-linear regime yet ($\delta \gg 1$), though it is based on some strict assumptions.

A cosmological fluid can be described in the Lagrangian coordinates, tracing the path of a fluid element into space and time. Given the position $\mathbf{q}$ of an element at t_0, its location at subsequent instants can be written in terms of the Lagrangian displacement field[2], $\mathbf{\Psi}$, as follows:

$$\mathbf{r} = a(t)\mathbf{q} + \mathbf{\Psi}(\mathbf{q}, t) \ , \tag{1.107}$$

where the first term describes the expansion of the Universe. The Zel'dovich approximation is conventionally considered as a first-order Lagrangian perturbations theory. It is based on the hypotesis that the position and the time dependencies of the displacement between the initial position and the final one are independent, so that they can be separated. Moreover, we are supposing that particles move along straight line trajectories with a kind of inertial motion. This approximation can be considered valid as long as two points cross each other (*shell-crossing*), since their mutual gravitational interaction is not considered in this treatment.

1.7 N-body simulations

The formation of cosmic structures can be approximated as the dynamical evolution of a system of particles, tracers of the underlying mass distribution. The treatment of this system is generally too complicated to be studied analytically. For this reason, N-body simulations are employed by cosmologists, in order to analyse the large scale structures (LSS) of the Universe with numerical methods. One of the most important advantages of the numerical simulations is the possibility of setting the cosmology-defining parameters as the user wishes, producing theoretical results that can be compared with observations. Moreover, N-body simulations allow the study of the non-linear regime of perturbation growth without the necessary simplifications adopted to reach analytical solutions. Since gravity is the dominant interaction on large scales, the LSS evolution is dominated by the effect of the DM, so at first order it will be sufficient to analyse the behavior of this component. However, to obtain a more realistic description of the LSS, the hydrodynamic consequences of the presence of the baryonic matter has to be taken into account.

The simplest kind of N-body simulations, which considers only gravita-

---

[2] The displacement field is an assignment to all the points of a region of displacement vectors, which specify the position of a point or a particle in reference to an origin or to a previous position.

tional effects, solves the following dynamical equation system:

$$\begin{cases} \mathbf{F}_i = GM_i \sum_{i \neq j} \frac{M_j}{r_{ij}^2} \hat{\mathbf{r}}_{ij}^2 \\ \ddot{\mathbf{x}}_i = \frac{\mathrm{d}\mathbf{v}_i}{\mathrm{d}t} = \frac{\mathbf{F}_i}{\mathrm{M}_i} \\ \dot{\mathbf{x}}_i = \frac{\mathrm{d}\mathbf{x}_i}{\mathrm{d}t} = \mathbf{v}_i \end{cases} , \tag{1.108}$$

where $\mathbf{F}_i$ is the gravitational force of the i-th particle, G is the gravitational constant, M_i is the i-th particle mass, $\mathbf{x}_i$ are the comoving coordinates of the i-th particle, $\mathbf{v}_i$ are the velocity components of the i-th particle, r_{ij} is the comoving distance between the i-th and j-th particles, and $\hat{r}_{ij}$ is the related versor. Given the system (1.108), the Euler equation of motion in equation (1.45) can be re-written as:

$$\frac{\mathrm{d}\mathbf{x}_i}{\mathrm{d}t} + 2\frac{\dot{a}}{a}\mathbf{v}_i = -\frac{1}{a^2}\nabla\Phi = -\frac{G}{a^3}\sum_{i,j \neq i} m_j \frac{\mathbf{x}_i - \mathbf{x}_j}{|\mathbf{x}_i - \mathbf{x}_j|^3} = \frac{\mathbf{F}_i}{a^3} , \tag{1.109}$$

where a is the scale factor. Applying the Second Friedman Equation (1.24), the Poisson Equation (1.45) becomes:

$$\nabla^2\Phi = 4\pi G\bar{\rho}(t)a^2\delta = \frac{3}{2}H_0^2\Omega_0\frac{\delta}{a} , \tag{1.110}$$

where $\bar{\rho}(t)$ is the average non-relativistic matter density of the Universe, δ the local density contrast, H_0 is the Hubble parameter and Ω_0 the non-relativistic matter density parameter.

A N-body simulation consists in the integration of the dynamical equations over discretised time steps, δt. At every time interval, the total gravitational force of the system, $\mathbf{F}_i$, is calculated. Then, the motion equation is evaluated by numerical integration and the new positions, $\mathbf{x}_i(t \pm \delta t)$, and velocities, $\mathbf{v}_i(t \pm \delta t)$, are obtained. At each step also the time is updated, $t = t + \delta t$. The choice of δt has to follow a suitable criterion and it has to be chosen the larger one from the set of possible time steps that satisfy the requirements. There is a wide number of possible criteria that can be suitable for different approaches. They can basically be divided into three main categories: *(i)* total energy conservation, *(ii)* convergence of final positions and velocities and *(iii)* reproducibility of the initial conditions (Bagla and Padmanabhan, 1997). The final output of a N-body simulation is a set of snapshots, that represent at each instant the evolution of the system of particles, as a result of the action of the gravitational force.

There are several computational techniques for developing a N-body simulation, differing in implementation, CPU efficiency, both spatial and mass resolutions, and more. In the following, we provide a brief description of some of the most used techniques.

- Particle-Particle (PP): this computational technique allows to compute the force acting on the i-th particle, as the sum of all the forces generated by all the other particles of the considered system. Since the number of required operations scales as $\mathcal{O}(N_p^2)$, this class of methods is the most time consuming, but also the most accurate, due to the force being directly computed for each particle.

- Particle Mesh (PM): this method determines the total gravitational force of a particle system, by implementing a grid, where all the relevant quantities are computed in each cell. In particular, the Poisson Equation is solved for the grid in the Fourier domain, and the force is applied to each particle again in the real space. This method is faster than the PP one, but it is less accurate, due to the limited resolution of the considered grid.

- Particle-Particle Particle Mesh (P^3M): this technique is based on the PM one, but it enhances the latter by introducing a direct-summation of the forces (like in the PP method) within a sphere with fixed-radius R around each particle (Efstathiou et al., 1985). This algorithm is more accurate than the PM: particles directly interact with each other in presence of zones with strong clustering. However, it implies an increasing of computational cost, which locally tends to be proportional to $\mathcal{O}(N_p^2)$. A way to reduce this problem is the implementation of an adaptive mesh, so that it is possible to redefine the local spatial resolution of overcrowded regions. The computational cost of the adaptive P^3M scales as $\mathcal{O}(N_p n(R)))$, where $n(R)$ is the average number of particles within R.

- Tree code: the simulation volume is divided in a hierarchical tree of subregions characterised by a proper centre of mass. The acting force from distant particles is then approximated to the force exerted by the centre of mass of those regions. The total number of required operations scales as $\mathcal{O}(N_p log(N_p))$.

Chapter 2

Statistical properties of cosmic voids

The fact that a widespread and unique definition of cosmic voids has not yet been provided represents one of the main issues in their cosmological usage. Moreover their identification is obviously not trivial, since their shape and position have to be reconstructed starting from the distribution of luminous tracers arranged mostly on their boundaries. Despite these major problems, cosmic voids gained increasingly popularity in the last decades thanks to some really intriguing features: voids are for their nature only mildly non-linear and tend to become more spherical as they evolve, which suggests that their evolution should be easier to reconstruct than that of positive perturbations. These characteristics allow us to predict the void statistical distribution as a function of size of voids. This property is particularly important to constrain cosmological parameters and makes voids fundamental probes that can be exploited to improve upon current constraints on dark energy and to discriminate between competing cosmological models (Pisani et al., 2015).

In this section, we will discuss the void definition adopted in this work. Then we propose a brief review of the excursion-set formalism that, in combination with the spherical collapse model, provides insights into many aspects of halo formation and can be used to predict the DM halo abundances and clustering. The analogous spherical expansion model can likewise be used to make excursion-set predictions for voids (Sheth and van de Weygaert, 2004), leading to the statistical distribution of voids as a function of their size. Finally, we overview the main features associated to the density profiles of cosmic voids.

2.1 Void definition

The spherical evolution model provides a complete description of the non-linear evolution of a spherically symmetric top-hat density perturbation. One of the main features of this model is that the evolution does not depend on the initial size of the region, i.e. on the initial radius or on the enclosed mass, but only on the amplitude of the initial top-hat overdensity (Jennings et al., 2013). In the overdensity case, a halo is said to have formed in the moment its density contrast reaches a level corresponding to either the virialisation of the spherical perturbation (the well-known critical linear overdensity $\delta_c \approx 1.686$ (see equation (1.95)), for an EdS Universe) or, with a milder assumption, when the perturbation reaches the *turn-around* (i.e. the linear density contrast at which a spherical perturbation inverts its expansion motion, that for an EdS Universe happens at $\delta_t \approx 1.06$, see equation (1.94)), and detaches from the overall expansion of the Universe. On the other hand, underdensities do never detach from the overall expansion, but instead they expand with a *Super-Hubble flow*. The expansion rate is inversely proportional to the embedded density, therefore shells centred around the same point are expected to expand faster as more they are close to the centre. This eventually leads to the inner shells reaching the outer ones, causing the event called *shell-crossing*. In spherically symmetric negative perturbations, we can consider the evolution to be linear ($|\delta\rho/\rho| \ll 1$) up to when shell-crossing occurs, then it will continue its evolution in a mildly non-linear regime. From this moment on we can assume that the void is formed.

Therefore in this work we will define voids as underdense, spherical, non-overlapping regions, which have gone through shell-crossing, that, in linear theory, occurs at a fixed level of density contrast ($\delta_v \approx -2.71$ for an EdS Universe, see equation (1.105)).

Beyond the void definition adopted in this work, other methods to define and detect cosmic voids have been proposed by the scientific community. In particular, voids can be simply identified as regions empty of galaxies, or at least with densities lower than a given fraction of the mean cosmic density (Micheletti et al., 2014; Elyiv et al., 2013). Alternatively, voids can be defined based on their geometry, such as as underdense geometrical structures, composed by polyedra, spheres or tessellations (Sutter et al., 2015; Platen et al., 2007; Neyrinck, 2008). Otherwise, we can rely on dynamical criteria in which mass tracers (e.g galaxies) are used to reconstruct the velocity density field (Elyiv et al., 2015; Lavaux and Wandelt, 2010; Forero-Romero et al., 2009). In the latter case, the void centres are defined as the points from which particles escape with the maximal velocity. These different definitions have all been employed in the development of void finder algorithms during the last decades. An analysis of the different classes of void finders will be presented in section 3.2.

2.2 Excursion-set formalism

The excursion-set formalism is built on the knowledge of the statistical properties of the linear density field. In real space, the linear density fluctuation field smoothed on a scale R is given by:

$$\delta(\mathbf{x}, R) = \int \frac{d^3k}{(2\pi)^3} \delta(\mathbf{k}) W(\mathbf{k}, R) e^{-i\mathbf{k}\cdot\mathbf{x}} ,$$

where $\delta(\mathbf{k})$ is the Fourier transform of the density perturbation $\delta(\mathbf{x}) \equiv [\rho(\mathbf{x}) - \rho_m]/\rho_m$, $\rho(\mathbf{x})$ is the local density at the comoving position $\mathbf{x}$, ρ_m is the background matter density and $W(\mathbf{k}, R)$ is a window function in Fourier space. It is common to relate the smoothing scale R to the corresponding variance of the linear density field, computed in terms of the size of the considered region:

$$\sigma^2(R) \equiv S(R) = \frac{1}{2\pi} \int \mathrm{d}k \, k^2 P(k) |W(k, R)|^2 ,$$

where $P(k)$ is the matter power spectrum in linear perturbation theory. We can refer to a trajectory $\delta(x, S)$ as a sequence of overdensities given by subsequent increases in the smoothing scale by increments ΔS. When a top-hat filter in k-space is used then $\delta(x, S)$ executes a random walk. Given an underlying Gaussian distribution for the linear density field, the excursion-set formalism allows us to associate probabilities to random walks that satisfy a given set of criteria for the smoothing scale at which they cross various density thresholds. For the collapse of perturbations, the spherical evolution model in combination with the excursion-set provides a good description of the statistics of DM haloes. As discussed in the previous section, a collapse occurs when the linear density fluctuation reaches a critical value or barrier δ_c. We can then use the excursion-set formalism to determine the fraction of trajectories that cross this barrier for the first time, accounting for the *cloud-in-cloud* process[1]. Then we can extend the model to underdense regions in the initial density field, that are naturally associated with voids in

---

[1] In the excursion-set formulation of halo abundance and evolution, the *cloud-in-cloud* problem consists in counting as haloes only those objects which are not embedded in larger ones. With the study of random walks, we can say that when a trajectory pierces the δ_c barrier more than once, only the crossing with the smallest value of $\sigma(M)$ has to be considered. For details see Sheth and van de Weygaert (2004).

the evolved density field today. This method leads to the modelling of the theoretical void size function, which is described in the next section.

2.3 Size function

The distribution of cosmic voids as a function of their size has been modelled for the first time by Sheth and van de Weygaert (2004) (hereafter SvdW model), with the same excursion-set approach used for the mass function of DM haloes (Press and Schechter (1974); Bond et al. (1991)).

The excursion-set theory applied to underdensities (Sheth and van de Weygaert (2004); Jennings et al. (2013)) predicts that the fraction of the Universe occupied by cosmic voids is given by:

$$f_{\ln\sigma} = 2\sum_{j=1}^{\infty} j\pi x^2 \sin(j\pi\mathcal{D}) \exp\left[-\frac{(j\pi x)^2}{2}\right] , \tag{2.1}$$

where

$$x \equiv \frac{\mathcal{D}}{|\delta_v|}\,\sigma\,,$$

and

$$\mathcal{D} \equiv \frac{|\delta_v|}{\delta_c + |\delta_v|}\,.$$

In the previous equations σ is the square root of the mass variance and the two parameters δ_v and δ_c represent the shell-crossing threshold (fixed at $\delta_v = -2.71$) and the critical value for the collapse of an overdense shell in an EdS Universe, respectively. The latter is expected to vary within $1.06 \leq \delta_c \leq 1.686$, since both the turn-around or the collapse density contrast value can be considered acceptable assumptions.

Equation (2.1) can be simplified by applying the approximation (used in the CBL library, see section 3.1) proposed by Jennings et al. (2013), which is accurate at the 0.2% level or better everywhere:

$$f_{ln\sigma}(\sigma) = \begin{cases} \sqrt{\frac{2}{\pi}}\frac{|\delta_v|}{\sigma}\exp\left(-\frac{\delta_v^2}{2\sigma^2}\right), & x \leq 0.276 \\ 2\sum_{j=1}^{4} j\pi x^2 \sin(j\pi\mathcal{D}) \exp\left[-\frac{(j\pi x)^2}{2}\right] & x > 0.276\,. \end{cases} \tag{2.2}$$

With the kernel probability distribution given in Eq. (2.1), it is straightforward to obtain the number density distribution of voids as a function of their size in linear theory by applying:

$$\left.\frac{\mathrm{d}n}{\mathrm{d}\ln r}\right|_{linear} = \frac{f_{\ln\sigma}(\sigma)}{V(r)}\frac{\mathrm{d}\,\ln\sigma^{-1}}{\mathrm{d}\,\ln r}\;. \tag{2.3}$$

In order to derive the void size function in the non-linear regime, a conservation criterion has to be applied. The model of the void size function developed by SvdW relies on the assumption that, when going from linear to non-linear, the total number of voids is conserved. While reaching shell-crossing, underdensities are expected to have expanded by a factor $a \propto \delta_v^{-3}$, thus a correction in radius by this factor is required:

$$\left.\frac{\mathrm{d}\,n}{\mathrm{d}\,\ln r}\right|_{\mathrm{SvdW}} = \left.\frac{\mathrm{d}\,n}{\mathrm{d}\,\ln(a\,r)}\right|_{linear}\;. \tag{2.4}$$

The SvdW size function takes into account the *void-in-cloud* side effect (i.e. the squeezing of voids that happen to evolve within larger scale overdensities). This is considered by defining $\mathcal{D}$ in equation (2.1) as a function of both the overdensity and the underdensity threshold. On the other side, the *void-in-void* side effect (i.e. the expansion of voids within larger scale underdensities) is not considered in the SvdW model. Jennings et al. (2013) argued that, since multiple countings of voids in the same region leads to a volume fraction occupied by underdensities which is larger than the total volume of the Universe, the SvdW is unphysical. They thus introduce a *volume conserving* model (hereafter Vdn model) which embeds a prescription to account for this: it is assumed that the total volume occupied by cosmic voids is conserved in the transition from linearity to non-linearity. Nonetheless, when shell-crossing is reached, voids recover the overall expansion rate, and continue growing with the Hubble flow (Sheth and van de Weygaert (2004), Blumenthal et al. (1992)). The conservation of volume is achieved by applying

$$\left.\frac{\mathrm{d}\,n}{\mathrm{d}\,\ln r}\right|_{\mathrm{Vdn}} = \left.\frac{\mathrm{d}\,n}{\mathrm{d}\,\ln r}\right|_{\mathrm{linear}}\frac{V(r_L)}{V(r)}\frac{\mathrm{d}\,\ln r_L}{\mathrm{d}\,\ln r}\;, \tag{2.5}$$

where the subscript L indicates a value derived in linear theory (i.e. not accounting for the conversion factor a). A comparison between the theoretical void size functions computed with the models described above is reported in figure 2.1.

The SvdW model has been tested on both simulated DM density fields and mock halo catalogues, finding that it systematically overpredicts the comoving number density of cosmic voids, as we can see in figure 2.2. To overcome this mismatch the underdensity threshold δ_v is commonly left as a free parameter, tuned on simulated halo catalogues. This severely affects

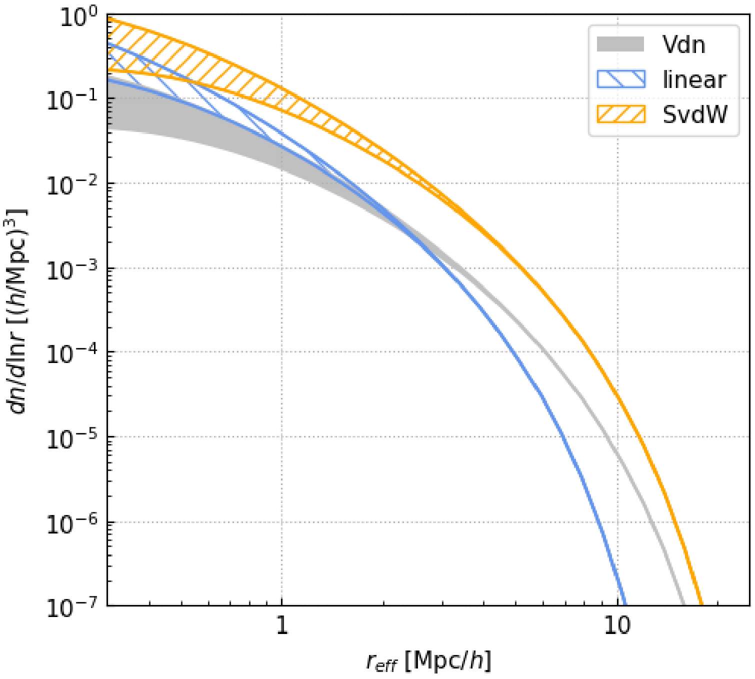

Figure 2.1: Comparison between different void size function models. The Vdn model is represented in grey, the linear model in blue, and the SvdW model in orange. The shaded or hatched regions are obtained varying δ_c in the range $1.06 \leq \delta_c \leq 1.686$. We can note that this variation changes the abundances significantly only at $r_{eff} \lesssim 1$ Mpc/h. These results are obtained by exploiting the CBL functions (see section 3.1) assuming a ΛCDM model characterised by $\Omega_M = 0.26$, $h = 0.715$, $\sigma_8 = 0.8$, $\Omega_{DE} = 0.74$, $\Omega_b = 0.044$ and $n_s = 0.96$ (spectral index).

the possibility of using the void size function as a cosmological probe. Jennings et al. (2013) have shown that the Vdn model does not require such a fine-tuning of the size function parameters, as long as the void catalogue is appropriately cleaned from spurious voids. Their results obtained analysing a large set of N-body simulations (see Table 2.3) are though limited to the case of cosmic voids detected on simulated DM (i.e. unbiased) distributions. In the next chapter we will extend their study to the case of samples of biased tracers, such as mock DM halo catalogues, which are more representative of the realistic case of galaxy surveys.

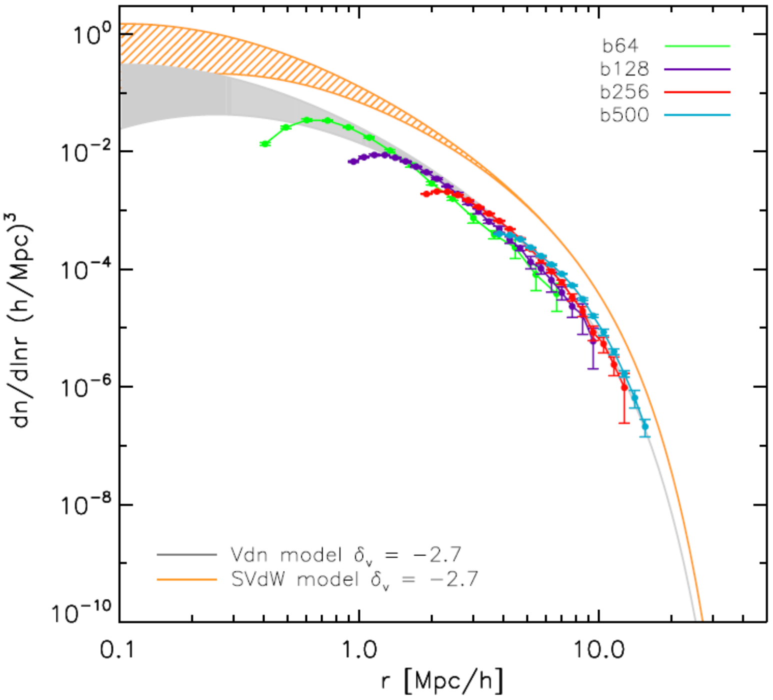

Figure 2.2: Void abundance in simulations versus predictions. The results refer to the DM distribution in simulations for the ΛCDM model with different box sizes: 64 Mpc/h (green), 128 Mpc/h (purple), 256 Mpc/h (red) and 500 Mpc/h (cyan). The error bars represent the scatter on the mean from eight different realizations of this cosmology for each box size. The range in predictions cover the parameter interval $\delta_c = [1.06, 1.686]$ with $\delta_v = -2.7$ and are consistent with simulations for the Vdn model (grey shaded), but not for the SVdW model (orange hatched). Credits: Jennings et al. (2013).

In figure 2.3 we show the effects of the variation of the cosmological parameters on the theoretical void size function computed with the Vdn

Model	Ω_M	h	σ_8	L_{box}[Mpc/h]	N_p	N_{sim}	z
ΛCDM	0.26	0.715	0.8	$64, 128, 256$	256^3	8	$0, 0.5, 1$
				500	400^3	1	0
				500	400^3	8	0
ΛCDM	0.26	0.715	0.9	$64, 128, 256$	256^3	8	$0, 0.5, 1$
EdS	1	0.715	0.8	$64, 128, 256$	256^3	8	0

Table 2.1: Relevant quantities of the cosmological simulations employed by Jennings et al. (2013). These simulations were carried out at the University of Chicago using the TreePM simulation code GADGET-2 (Springel, 2005). From left to right, the columns represent the cosmological model, the matter density parameter, the reduced value of the Hubble constant, the amplitude of the (linear) power spectrum on the scale of 8Mpc/h, the box size, the number of particles, the number of simulations and the redshift. The other cosmological parameters are set as follows: $\Omega_{DE} = 0.74$, $\Omega_b = 0.044$ and $n_s = 0.96$.

model. In particular, we choose the WMAP7 cosmology (see Table 5.1), performing the variation of the quantities σ_8, Ω_{DE} and Ω_M. As we can see, these changes of the cosmological parameters cause visible effects on the theoretical size function. This method will be analysed in details in chapter 5.7.

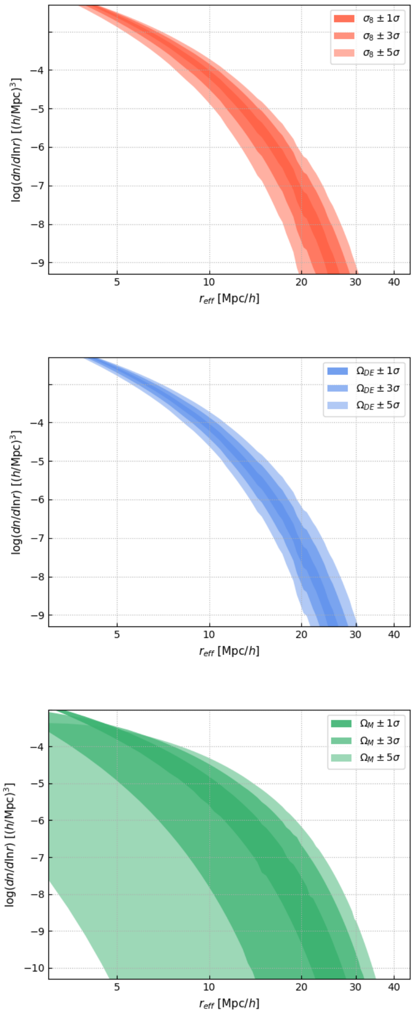

Figure 2.3: Effects of the variation of the cosmological parameter on the theoretical void size function. In the *upper* panel is represented the variation of σ_8. In particular, this quantity is modified with $\pm 1\sigma$, $\pm 3\sigma$ and $\pm 5\sigma$, where σ in the value of the uncertainty relative to that parameter in the WMAP7 cosmology. The modifications on the size function are represented with different shades of red. In the *middle* panel the parameter that we varied is Ω_{DE}, with the same prescription described above, this time represented with shades of blue. In the *bottom* panel the parameter that we varied is Ω_M, with the same prescription described above, this time represented with shades of green.

2.4 Void density profiles

Another fundamental quantity to describe the structure of cosmic voids in a statistical sense is their spherically averaged density profile. Void density profiles have been studied in detail in the recent literature (e.g. Sutter et al., 2014; Ricciardelli et al., 2014; Hamaus et al., 2016). Void profiles typically exhibit a few very characteristic features: a deep under-dense core with central density increasing with void size, and an over-dense ridge (compensation wall) that exceeds the mean density of the Universe and then stabilises around $\delta \simeq 0$. The height of the compensation wall decreases with void size, causing the inner profile slope to become shallower. The shape of the spherically averaged density void profiles $\langle n_{vt} \rangle$ can be described by a simple empirical formula (Hamaus et al., 2016):

$$\frac{n_{vt}(r)}{\langle n_t \rangle} - 1 = \delta_c \frac{1 - (r/r_s)^{\alpha}}{1 + (r/r_v)^{\beta}} \ ,$$

where δ_c is the central density contrast at $r = 0$, r_s is a scale radius at which the density equals the average density of tracers $\langle n_t \rangle$, and α, β describe the inner and outer slopes of the profile, respectively. Figure 2.4 shows the stacked density profiles for voids with different mean effective radii. These result are obtained by applying VIDE to ΛCDM N-body simulations (Warren, 2013) and derived mock galaxy catalogues.

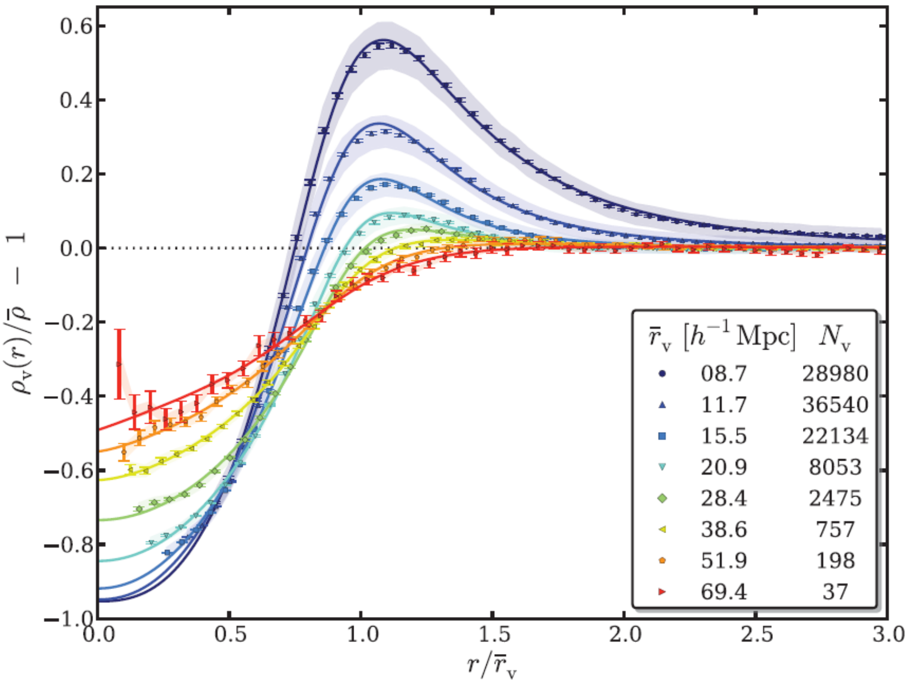

Figure 2.4: Stacked real-space density profiles of voids at $z = 0$ with mean effective radii and void counts, N_v, indicated in the inset. Shaded regions depict the standard deviation σ within each of the stacks (scaled down by 20 for visibility), while error bars show standard errors on the mean profile $\sigma/\sqrt{N_v}$. Solid lines represent individual best-fit solutions. Credits: Hamaus et al. (2016).

Chapter 3

Numerical tools to construct cosmic void catalogues

In this chapter, we will explain the methodology used for the data analysis presented in this thesis work. In particular, we will present the set of numerical libraries used for all the calculations and for the statistical treatment of the data. Finally, we will describe the numerical algorithms used to create and to clean the void catalogues.

3.1 CosmoBolognaLib

The CosmoBolognaLib (hereafter CBL) is a large set of *free software* C++ /Python libraries, that provide an efficient numerical environment for cosmological investigations of the large-scale structure of the Universe (Marulli et al., 2016). This software is particularly suited to handle with catalogues of astronomical objects, both real and simulated. Thanks to the large amount of functions recently implemented (Ronconi et al., in preparation), the CBL offers the necessary tools to analyse void catalogues and to perform many of the statistical analyses requested for this work. In particular we make use of these libraries to manage the DM particle, halo and void catalogues, and to measure and model the halo bias and the void size function.

3.2 Void finders

Since there is not general concordance in the definition of voids yet, many different void finders have been proposed and exploited in the last decades (see Colberg et al. (2008) for a cross-comparison of the different techniques).

Following the strategy of Lavaux and Wandelt (2010) we can classify void finding algorithms in three main classes, on the basis of the type of criterion applied:

- *Density criterion.* These algorithms define voids as regions empty of tracers or with local density below a fixed value (Micheletti et al., 2014; Elyiv et al., 2013). Furthermore, tracers are divided in *wall tracers* and *field tracers* depending on the density of the region in which they are localised ("strongly overdense" regions and "mildly underdense" regions, respectively).

- *Geometrical criterion.* This class includes void finders that identify voids as geometrical underdense structures like spherical cells or polyhedra (Sutter et al., 2015; Platen et al., 2007; Neyrinck, 2008). In particular, these algorithms search for specific features in the continuous 3D distribution of cosmic tracers. Then, making use of these features, the density field is reconstructed and the local density minima are used to obtain the void distribution.

- *Dynamical criterion.* These void finders are based on dynamical criteria in which tracers are not exploited to reconstruct underlying mass distribution but are used as test particles of the cosmic velocity field. Therefore, in these algorithms, a void is defined as a region in which the matter is evacuated (Elyiv et al., 2015; Lavaux and Wandelt, 2010; Forero-Romero et al., 2009).

In this thesis work, we make use of the Void IDentification and Examination toolkit (VIDE) (Sutter et al., 2015) to construct our void catalogues. VIDE belongs to the class of algorithms based on geometrical criteria and it implements an enhanced version of the ZOnes Bordering On Voidness (ZOBOV) algorithm (Neyrinck, 2008). ZOBOV is a popular publicly available code that finds density depressions in a three-dimensional set of points, without any free parameter or assumption about the void shape. The void finding procedure consists of three main steps:

1. As a first step, the finder reads in the tracer positions and associates to each tracer a cell of volume that is closer to it than to any other tracer. This procedure is referred to as *Voronoi tessellation*, and the resulting cells are denoted *Voronoi* cells. Then the algorithm associates a density to each Voronoi cell that is, assuming equal weights for all particles, the inverse of the Voronoi cell volume. In this way a well-defined density field is obtained.

2. As a second step, local density minima are found and their surrounding basins identified. Density minima are defined as the cells whose density is lower than the density of every other adjacent cell. Then, starting from these density minima, the surrounding Voronoi cells are merged consecutively if their individual density is above the one of the previously merged cell. The process of merging is stopped once a cell of lower density is encountered. The result of this procedure in the creation of local density basins, called *zones*. A representation of this procedure is reported in figure 3.1.

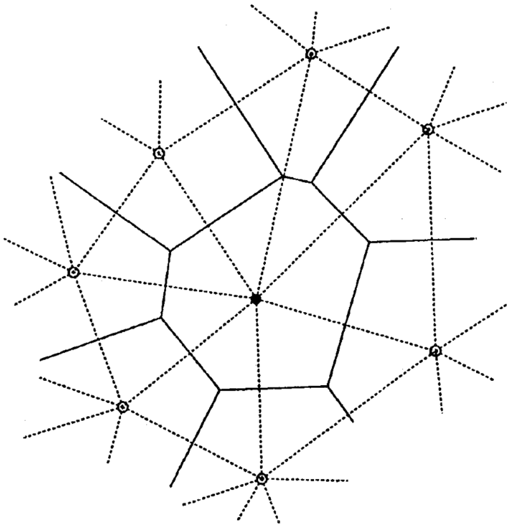

Figure 3.1: Natural Neighbours of a point. The black dot represents the central point, the open circles its Natural Neighbours. The solid edges mark the Voronoi cell surrounding the central point, along with the connecting Voronoi edges. Credits: Platen et al. (2007)

3. Finally, zones are merged to become voids making use of the so-called *watershed algorithm* (e.g. Platen et al. 2007). This method , illustrated in figure 3.2, consists of rising a density threshold starting from each zone's local density minimum. During the raising, all the surrounding regions, that have a value of density lower than the threshold, are added to the basin of a starting minimum. As long as shallower zones are added to the original zone, the final void consists of all such merged zones, which are still recorded as its sub-voids. When a deeper zone is encountered, the process is stopped.

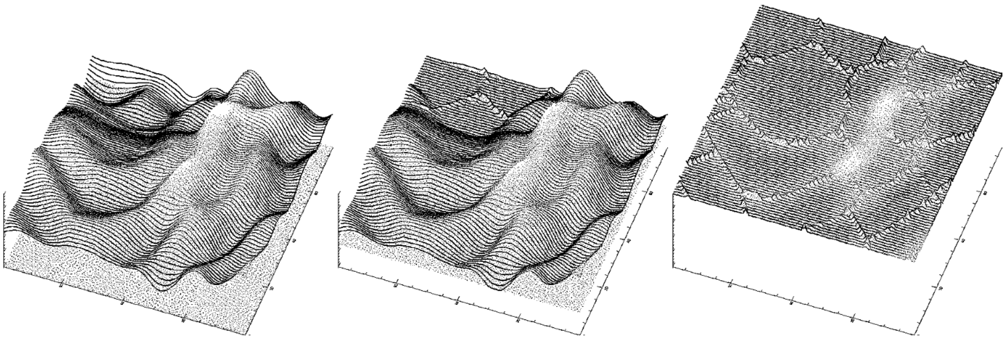

Figure 3.2: Principle of the watershed technique represented in three panels. The *left panel* shows the shape of the density field. Starting from the local minima, the surrounding basins of the surface start to flood as the water level continues to rise (dotted plane initially below the surface). Where two basins meet up near a ridge of the density surface, a “dam” is erected (*central frame*). Ultimately, in the *right frame* the entire surface is flooded, leaving a network of dams which defines a segmented volume and delineates the corresponding cosmic web. Credits: Platen et al. (2007)

Therefore, the set of voids created with this technique is naturally organised with a hierarchical structure of nested voids. Each of the voids found with VIDE has its centre defined as volume-weighted barycentre, $\overline{X}$, of the N Voronoi cells that define the void,

$$\overline{X} = \frac{\sum_{i=1}^{N} \overline{x}_i V_i}{\sum_{i=1}^{N} V_i} \ ,$$

where $\overline{x}_i$ are the coordinates of the i-th tracer of that void, and V_i the volume of its associated Voronoi cell. The effective void radius, r_v, is calculated from the total volume of the void, V_v. It is defined as the radius of a sphere having the same volume:

$$V_v \equiv \sum_{i=1}^{N} V_i = \frac{4\pi}{3} r_v^3 \ .$$

This centre does not necessarily coincide with the position of a tracer.

In order to make a comparison between different void finders, that will presented in section 3.4 we present also the algorithm developed by Cannarozzo et al. (in preparation), which is already implemented in CBL. This void finder is based on dynamical criteria and can divided in three steps:

1. The aim of the first step is to reconstruct dynamically the displacement field of cosmic tracers. This is performed exploiting the *Zel’dovich*

Approximation (see Subsection 1.6.6), to reconstruct the initial tracers Lagrangian positions by randomising the Eulerian coordinates. The random distribution is then used to obtain a displacement field, that approximates the velocity field of cosmic structures.

2. The second step consists in performing several reconstructions of the density field, that are then averaged by using a Gaussian filter. Making use of the watershed technique, the code finds the local density minima, corresponding to the sources of maximum displacement. Therefore, cosmic voids are considered as *sinks* in the reverse streamlines of tracers.

3. Finally, once all subvoids are identified, the algorithm provides a void catalogue, in which are reported centres and radii of the voids.

In this algorithm the void centre is identified as the absolute minimum value of the divergence field within a void:

$$\mathbf{r}_{void} = \min(\boldsymbol{\nabla} \cdot \mathbf{v})_{void} \tag{3.1}$$

This type of procedure has the advantage of employing Lagrangian coordinates, which considerably reduces the *shot noise* problem, caused by the discrete mass tracers. In fact, this algorithm does not need to perform the reconstruction of the density field. This void finder has been tested by Cannarozzo on a DM halo catalogue extracted from the DEMNuni (Dark Energy and Massive Neutrino Universe) simulations (Castorina et al., 2015), finding a reasonable agreement between the theoretical size function computed with the Vdn model and the measured size distribution of voids, once the voids have been opportunely re-scaled by the cleaning correction method proposed by Ronconi and Marulli (2017), that will be analysed in the next section.

3.3 Cleaning algorithm

As said, many different definitions of cosmic voids have been proposed during the years. It is thus particularly important to adopt the same definition when detecting voids and modelling their statistics or, alternatively, to clean properly the void catalogues detected with standard methods. This latter approach is the one that we choose to follow. As widely described in Ronconi and Marulli (2017), a new algorithm has been recently implemented in the CBL environment to clean void catalogues and make them directly comparable to model predictions. It is important to highlight that the cleaning procedure is totally independent of the void finder adopted to build the catalogue, since it makes use only of the positions of void centres. The cleaning algorithm can be divided in three main steps:

- The *spurious* voids are removed from the catalogue, with the following criteria: *(i)* voids whose effective radius do not belong to a selected range $[R_{min}, R_{max}]$ and *(ii)* voids whose central density is higher than $(1+\delta_v^{NL})\overline{\rho}$, where δ_v^{NL} is a given non-linear underdensity threshold, and $\overline{\rho}$ is the mean density of the sample.

- The effective radius of voids is re-scaled: the algorithm reconstructs the density profile of each void and, treating the void as a growing sphere located at its centre, the value of the radius is increased until the sphere reaches the shell-crossing density threshold $\delta_{sc} = -0.795$.

- Check for overlaps: when two voids do overlap, the one of them with higher density contrast is rejected, avoiding double countings.

The effect of these steps on a void catalogue built with VIDE is reported in figure 3.3. The sample of voids is extracted from a ΛCDM N-body simulation with 256^3 DM particles and box side of length $128\text{Mpc}/h$. This procedure provides a set of spherical voids that enclose the shell-crossing density contrast, as requested by the spherical evolution model. This is crucial in order to standardize the outcome of void finders of different types, aligning the definition of voids to the one employed to derive the theoretical size function.

This methodology has been tested systematically by Ronconi et al. (in preparation), applying it on a set of N-body simulation snapshots. The DM simulations analysed, whose characteristics are reported in Table 3.1, have different resolution and boxside length; different redshifts have been considered. The results of these tests are shown in figure 3.4. The coloured symbols mark the void size distribution measured in the simulation snapshots while the grey shaded region represents the model prediction. We can see that the size distribution of voids is fully consistent with the theoretical predictions.

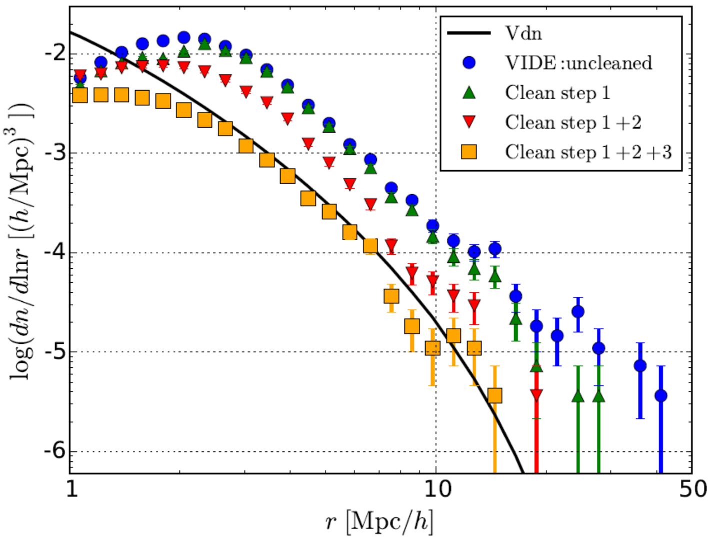

Figure 3.3: The effect of the different steps of the cleaning algorithm on the void size function. The theoretical one is reported as black solid line and represents the Vdn model predictions for the cosmological model here considered (ΛCDM with cosmological parameters defined in Table 5.1). The blue dots show the distribution of voids detected by VIDE from a ΛCDM N-body simulation. The green triangles, the red upside-down triangles and the orange squares are the size distribution of voids after the application of the first, the second and the third steps of the cleaning procedure, respectively. Credits: Ronconi and Marulli (2017)

L_{box} [Mpc/h]	N_p	m.p.s. [Mpc/h]	mass [10^{10} $M_\odot/h$]
500	256^3	≈ 2.00	56.06
256	256^3	1.00	7.52
128	256^3	0.50	0.94
64	256^3	0.25	0.12
1000	$2 \cdot 1024^3$	1.00	5.84

Table 3.1: Relevant quantities of the cosmological simulations employed by Ronconi et al. (in preparation). From left to right, the columns report the box size, the number of particles, the mean particle separation (m.p.s.) and the mass resolution of each simulation.

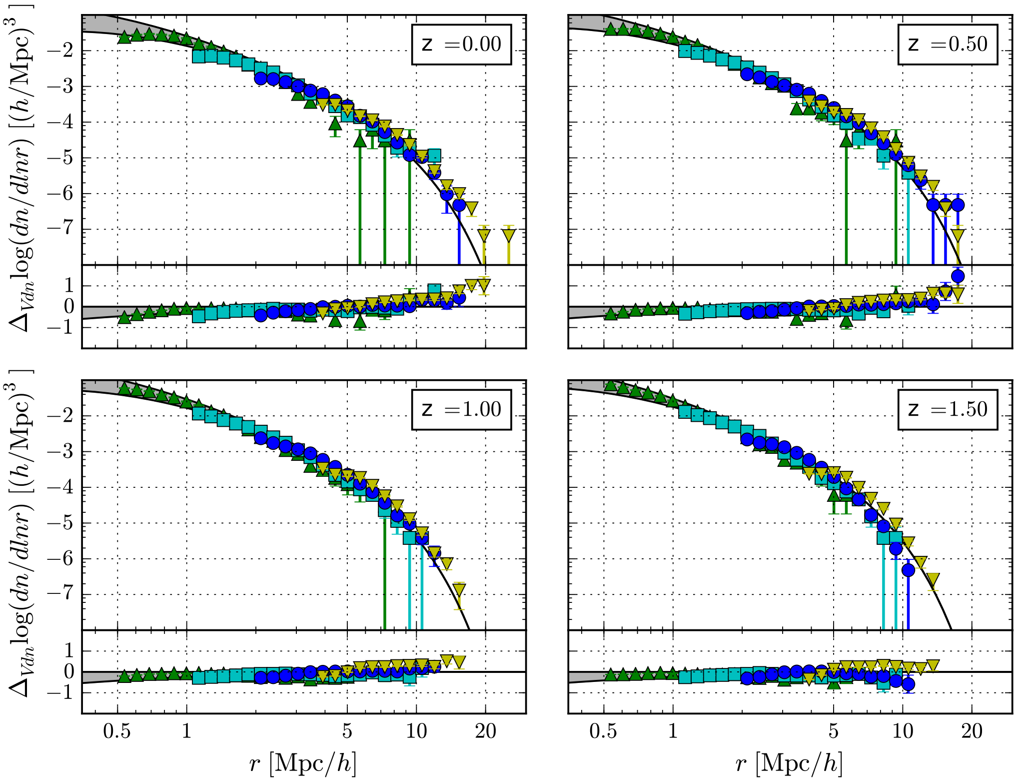

Figure 3.4: Theoretical void size function computed with the Vdn model (gray shaded region) at four different redshifts (panels) compared with the distribution of cosmic voids after having applied the cleaning procedure. *Lower part of each panel*: Logarithmic difference between the Vdn model prediction and the measured distribution. All the catalogues employed are extracted from ΛCDM simulations with cosmology defined in Table 5.1. Credits: Ronconi et al. (in preparation).

3.4 An application of the void finder and cleaning methods

Here we present a comparison between the size functions of void catalogues detected with two different void finders: VIDE and the dynamical CBL void finder (see section 3.3). The halo catalogue is build with the method that will be described in section 5.1, assuming the ΛCDM cosmology, with the parameters defined in Table 5.1. Then we apply the cleaning algorithm described in section 3.3 to the voids belonging to both the catalogues. With this procedure, the different void definitions adopted by the two void finders are made uniform to a specific criterion.

As we can see from figure 3.5, the two methods are consistent, except for small radii. The reason of this apparent discrepancy will be accurately examined in a forthcoming future project. In the following analysis we will make use of the catalogues created applying the VIDE algorithm.

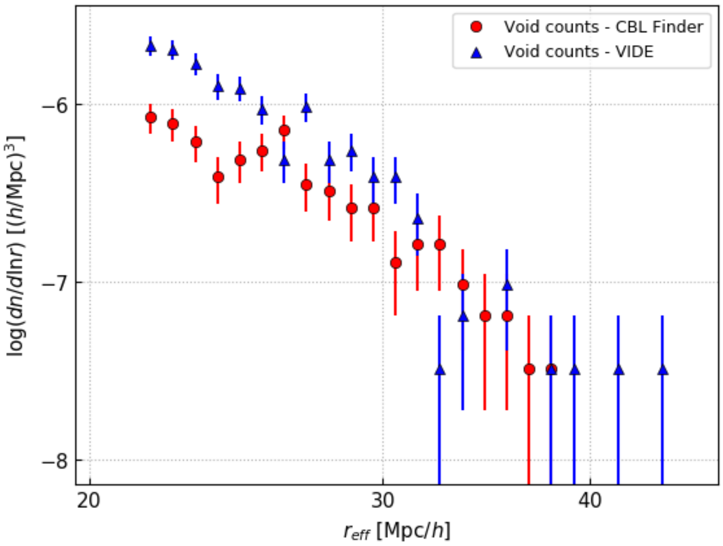

Figure 3.5: Comparison between the results of two different void finders applied to the same distribution of biased tracers. Red dots represent the void size function obtained for a void catalogue built with VIDE, while the blue triangles represent the size function of voids extracted with the void finder implemented in the CBL. The void finder algorithms are applied to halo catalogues built as described in section 5.1, with the cosmological parameters reported in Table 5.1. Both the catalogues are cleaned with the algorithm described in section 3.3.

Chapter 4

Cosmic voids in the distribution biased tracers

The tracer bias must be taken into account in order to extract robust cosmological constraints from the number counts of cosmic voids detected in galaxy redshift surveys (see e.g. Pollina et al., 2017). In fact, the size and the comoving number density of voids traced by the DM distribution are significantly different with respect to the ones of the voids traced by a biased DM halo density field. To handle with this problem, the bias trend inside cosmic voids has to be taken into account. On small scales the bias is scale-dependent. On the other hand, at large scales density fluctuations are in the linear regime, so the tracer bias behaves as a simple constant offset in the clustering amplitude. The latter is known as the *linear bias* and it depends on a number of properties of the tracers, one of the most important being the mass of its host haloes: more massive halos exhibit a higher clustering bias (see e.g. Marulli et al., 2013, and references therein).

4.1 Correlation function

The 2PCF measures the degree of clustering of a tracer population. The probability that a tracer A in the volume dV_A is separated from another tracer B in the volume dV_B by a comoving distance r is given by:

$$d^2P = \langle n_A \rangle \langle n_B \rangle [1 + \xi_{AB}(r)] \; \mathrm{d}V_A \mathrm{d}V_B \ , \tag{4.1}$$

where $\langle n_A \rangle$ and $\langle n_B \rangle$ are the mean comoving densities of the two kind of tracers. The spatial 2PCF, $\xi_{AB}(r)$, is thus the deviation of such probability from that expected from a random distribution of tracers (Peebles, 1980).

When we compare tracers of the same population, we refer to ξ as the auto-correlation function while, if we compare two kinds of tracers, we refer to ξ as the cross-correlation function. In the linear regime, the bias can be derived in terms of the auto-correlation function as follows:

$$b = \sqrt{\xi_{tt}/\xi_{mm}}\,, \tag{4.2}$$

or, in terms of the cross-correlation function as:

$$b = \xi_{tm}/\xi_{mm}\,, \tag{4.3}$$

where ξ_{mm} is the matter auto-correlation function, ξ_{tm} is the tracer-matter cross-correlation function, and ξ_{tt} is the tracer auto-correlation function.

4.2 Ratio of density contrasts as bias estimators

The density contrast, δ, can be obtained by dividing the number density within a given sphere (top-hat filter) by the mean number density of the sample:

$$\delta = \frac{n(r)}{\langle n \rangle} - 1\,. \tag{4.4}$$

If we assume that the tracer density contrast, $\delta_t = f(\delta)$, is a linear function of the underlying DM density contrast on some scale, then we can define the linear tracer bias, b, as the ratio between the mean overdensity of tracers and the mean overdensity computed on the dark matter field :

$$b = \frac{\delta_t(r)}{\delta_m(r)}\,. \tag{4.5}$$

This value is equivalent to the ratio of the void-tracer cross-correlation function (ξ_{vt}) relative to the corresponding void-matter cross-correlation function (ξ_{vm}), with void positions identified by their centres (e.g Pollina et al., 2017):

$$b = \frac{\xi_{vt}}{\xi_{vm}} = \frac{\frac{n_{vt}(r)}{\langle n_t \rangle} - 1}{\frac{n_{vm}(r)}{\langle n_m \rangle} - 1}\,. \tag{4.6}$$

So we can conclude that the void-tracer cross-correlation function encodes the same information as the void density profile.

4.3 Theoretical bias

The effective bias of DM haloes with masses in a given range and at a given mean redshift can be computed as:

$$b_{eff}(z) = \frac{\int_{M_{min}}^{M_{max}} \mathrm{d}M \, b(M,z)\Phi(M,z)}{\int_{M_{min}}^{M_{max}} \mathrm{d}M \, \Phi(M,z)} \ , \tag{4.7}$$

where $\Phi(M,z)$ is the halo mass function, and M_{min} and M_{max} are the lowest and largest masses in the sample, respectively. In chapter 5 we will make use of specific models to compute the mass function $\Phi(M,z)$ and the bias $b(M,z)$ in order to evaluate the theoretical bias of halo catalogues. In particular, in our work equation (4.7) is estimated with the CBL, using the Code for Anisotropies in the Microwave Background (CAMB, http://camb.info) to compute the matter power spectrum and mass variance, and the Tinker et al. (2008) and Sheth et al. (2001) (SMT) models to compute the halo mass function and linear bias, respectively. Specifically, the mass function is computed as follows:

$$\Phi(M,z)_{Tinker} = \frac{\mathrm{d}n}{\mathrm{d}M} = A\left[\left(\frac{\sigma}{b}\right)^{-a} + 1\right] \frac{\overline{\rho}_m(z)}{M} \frac{dln(\sigma)^{-1}}{dM} \ , \tag{4.8}$$

where $\overline{\rho}_m$ is the mean density of the Universe, σ is the square root of the variance and a, A, b are parameters calibrated using N-body simulations Viceversa the linear bias is computed as:

$$\begin{aligned} b(\nu)_{SMT} = 1 + \frac{1}{\sqrt{a}\delta_c} \sqrt{a}(a\nu^2) + \sqrt{a}b(a\nu^2)^{1-c} \\ - \frac{(a\nu^2)^c}{(a\nu^2)^c + b(1-c)(1-c/2)} \ , \end{aligned} \tag{4.9}$$

where $a = 0.707$, $b = 05$, $c = 0.6$ are parameters tuned to work in N-body simulations.

Figure 4.1 reports the trend of bias as function of the halo mass, comparing the results obtained with simulations with the theoretical bias computed with different analytical methods.

4.4 Estimating the tracer bias

In order to estimate the tracer bias from the 2PCF of the DM haloes of our simulations, we follow the prescription described in Marulli et al. (2018), which makes use of functions implemented in the CBL.

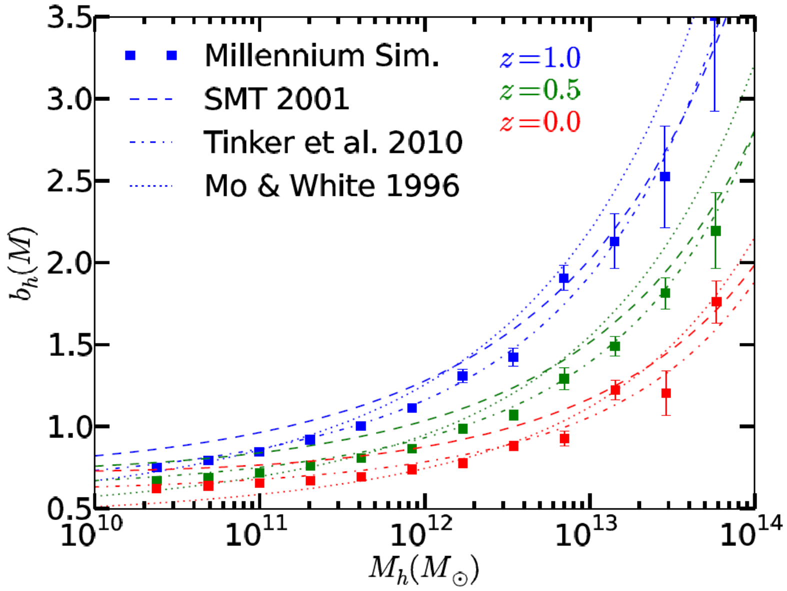

Figure 4.1: Halo bias as a function of mass, at three different redshifts, compared to the theoretical predictions obtained with different models. The squares show the bias measurements from the *Millennium Simulation* (Springel, 2005), assuming the following cosmology: $\Omega_M = 0.25$, $\Omega_b = 0.045$, $h = 0.73$, $\Omega_\Lambda = 0.75$, $n = 1$ and $\sigma_8 = 0.9$. Dashed lines show the analytic model of Sheth et al. (2001) (see equation 4.8), dashed-dotted lines correspond to the Tinker et al. (2010) model, and dotted lines are the analytic model of Mo and White (1996). The redshift values are represented with different colours, as specified in the labels. Credits: Pujol and Gaztañaga (2014).

In this work we measure the angle-averaged 2PCF $\hat{\xi}(r)$ using the Landy and Szalay (1993) estimator, which is expressed by the following equation:

$$\hat{\xi}(r) = \frac{N_{RR}}{N_{CC}}\frac{CC(r)}{RR(s)} - 2\frac{N_{RR}}{N_{CR}}\frac{CR(s)}{RR(s)} + 1 \ , \tag{4.10}$$

where $CC(r)$, $RR(r)$; and $CR(r)$ are the binned numbers of object-object, random-random, and object-random pairs with distance $r \pm \Delta r$, while $N_{CC} = N_C(N_C - 1)/2$, $N_{RR} = N_R(N_R - 1)/2$ and $N_{CR} = N_C N_R$ are the total numbers of object-object, random-random, and object-random pairs in the sample, respectively. The Landy and Szalay (1993) estimator provides an unbiased estimate of the 2PCF in the limit $N_R \to \infty$, with minimum variance.

In order to estimate the 2PCF with equation 4.10, we need to construct a random catalogue, with the same geometry of the halo catalogue. Once the random catalogue is built, we compute the covariance matrix $C_{i.j}$, which measures the variance and correlation between the different bins of the 2PCF. The covariance is defined as follows:

$$C_{i,j} = \mathcal{F} \sum_{k=1}^{N_R} (\xi_i^k - \overline{\xi}_i)(\xi_j^k - \overline{\xi}_j) \ , \tag{4.11}$$

where the subscripts i and j run over the 2PCF bins, while k refers to the 2PCF of the k-th of N_R catalogue realisations, and $\hat{\xi}$ is the mean 2PCF of the N_R samples. $\mathcal{F}$ is the normalisation factor, which takes into account the fact that the N_R realisations might not be independent (see Norberg et al., 2009).

Finally, we perform a Bayesian statistical Markov chain Monte Carlo (MCMC) analysis of the 2PCF. We make use of the commonly used likelihood function $\mathcal{L}$, defined as:

$$-2\ln\mathcal{L} = \sum_{i=1}^{N} \sum_{j=1}^{N} (\xi_i^d - \xi_i^m) C_{i,j}^{-1} (\xi_j^d - \xi_j^m) \ , \tag{4.12}$$

where $C_{i,j}^{-1}$ is the inverse of the covariance matrix estimated from the data, N is the number of comoving separation bins at which the 2PCF is estimated, and the superscripts d and m stand for "data" and "model" respectively. The 2PCF model, $\xi^m(s)$, is computed as follows:

$$\xi_m(r) = b_{eff}^2 \xi_{DM}(r) \ , \tag{4.13}$$

where $\xi_{DM}(r, z)$ is the DM 2PCF, which is estimated by Fourier transforming the power spectrum, $P_{DM}(k, z)$, computed with CAMB. By sampling the posterior distribution of the effective bias parameter, b_{eff}, we obtain an accurate estimate of its best-fit value and uncertainty.

Chapter 5

The size function of cosmic voids

With the knowledge acquired in the previous chapters, we are now ready to extend the treatment of the void size function to cosmic voids selected in the distribution of biased mass tracers. This is the first time that the theoretical model of the size function is applied to voids identified in the mass distribution of cosmic tracers. The scientific research carried out until now has validated the theoretical predictions of the void size function only using DM catalogues, thus extracting voids from the total distribution of the DM particles. Having a reliable model to take into account the effect of bias on void catalogues is mandatory in order to extract cosmological constraints from the statistics of cosmic voids in real surveys. In fact, dealing with real data catalogues, the distribution of luminous tracers (e.g. galaxies, galaxy clusters, etc.) does not represent a perfectly faithful description of the underlying DM distribution. In order to predict the statistics of the total mass distribution, the value of the effective bias has to be estimated (e.g with the methods proposed in chapter 4). In this chapter we will demonstrate that this value is different inside cosmic voids, with respect to its value on large scales. Therefore, in order to compute a re-parametrisation of the void size function, the value of the bias that has to be taken in to account is the one measured inside voids. With this prescription, we are able to modify the theoretical size function model, according to the bias of the void tracers. Thanks to the achievements of this thesis work, we can now proceed towards the full exploitation of the proposed method on real data.

In this chapter we will describe the analysis performed on a set of DM halo mock catalogues, having different values of bias, from which void catalogues are extracted. We will compute the density profiles both in the distribution of haloes and in the underlying DM particle density field, calculating the

h_0	Ω_{CDM}	Ω_b	Ω_Λ	$\mathcal{A}_s$	n_s
0.7	0.226	0.0451	0.7289	$2.194 \cdot 10^{-9}$	0.96

Table 5.1: Fiducial WMAP7 cosmological parameters used in this work.

density contrast starting from the void centres. In this way we will be able to compare the theoretical bias to the one obtained with equation (4.5). Once the estimate of the bias has been performed, we will compare the theoretical size function to the one derived from the cleaned void catalogue. Finally, we will investigate the effect of varying some of the cosmological parameters used to compute the theoretical void size function.

5.1 Building the mock void catalogues

For this analysis, we make use of mock halo catalogues extracted from the Coupled Dark Energy Cosmological Simulations (CoDECS) (Baldi, 2012), a set of high resolution N-body simulations that cover a volume of $1(\mathrm{G}pc/h)^3$. Specifically, the simulation considered follows the dynamical evolution of $2 \cdot (1024)^3$ particles: half of them are DM particles and constitutes the haloes, the other half is composed by non-collisional gas particles. Only DM particles will be considered in the following analysis. The halo catalogues are built from the CoDECS with a FoF algorithm. The void catalogues are extracted using the code VIDE (see section 3.2), then cleaned with the algorithm described in section 3.3. For this study we assume the standard ΛCDM cosmology, with WMAP7 parameters (Komatsu et al., 2011), the same with which the CoDECS simulations are built (see Table 5.1). This analysis is performed only with catalogues at $z = 0$. In order to inspect different bias values, 3 different mass cuts are applied to the halo catalogues: $2 \cdot 10^{12}$, $5 \cdot 10^{12}$ and 10^{13} $M_\odot/h$.

5.2 Estimating the tracer bias

To measure the effective bias of the tracers (i.e. DM haloes) used to detect the cosmic voids, we model the tracer 2PCF by performing a MCMC posterior sampling technique, as described in section 4.4. We also compute the effective bias by simply estimating the mean of the ratio between the tracer and DM 2PCFs at large scales, as described in equation 4.2.

The two bias measurements are compared to the theoretical halo bias given by equation (4.7). The latter is estimated with the CBL, using CAMB to compute the matter power spectrum and mass variance, and the Tinker et al. (2008) and Sheth et al. (2001) models to compute the halo mass function and linear bias, respectively.

Figure 5.1 compares our bias estimates with theoretical predictions. As it can be seen, at scales larger than 10 Mpc/h, the bias is almost constant. The measured values are consistent with the theoretical predictions. Moreover, the bias estimate obtained with the ratio between the tracer and DM 2PCFs is perfectly in agreement with the value obtained with the full MCMC modelling of the 2PCF. For the following analysis, we choose to rely on the latter estimate, that is more accurate.

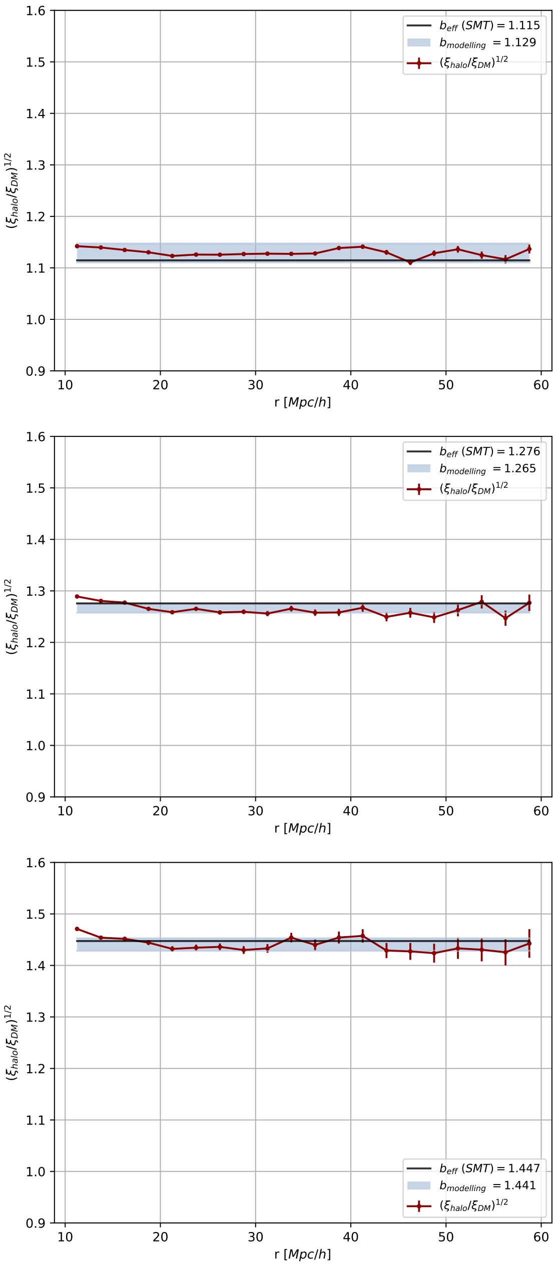

Figure 5.1: Comparison between different bias values of DM halo catalogues with different mass cuts: $2 \cdot 10^{12}\ M_\odot/h$ (*upper panel*), $5 \cdot 10^{12}\ M_\odot/h$ (*central panel*) and $10^{13}\ M_\odot/h$ (*lower panel*). The shaded areas show the bias value computed with the MCMC modelling, fitting in a range of radii of $[15 - 40]$ Mpc/h and considering an error of 5σ. The black solid line shows the value of the theoretical effective bias, computed with equation (4.7). The red line represents the trend of the ratio between the 2PCF of DM haloes and the theoretical one computed for DM.

5.3 Bias inside voids

To estimate the tracer bias inside the detected cosmic voids in the simulation, we divide each void sample, extracted from the different halo catalogues, in 80 radial bins, from R_{min} to R_{max}, that is the minimum and the maximum values of R_{eff} in each catalogue. We analysed only the R_{eff} bins with more than 20 voids, to have enough statistics. For each considered radial bin, the spherically averaged density contrasts of DM, δ_{DM}, and haloes, δ_{halo}, are computed as a function of the void radius. All the profiles inside each radial bin are then averaged. The radius of each void is then re-scaled, dividing it by the average effective radius, $\langle R_{eff} \rangle$, of the considered bin. For this reason, the size of the bins has to be narrow enough, in order to re-scale the radii properly, but at the same time wide enough to contain a sufficient number of voids. Finally, errors are computed as the standard deviation from the mean density profile. For this analysis, the DM catalogues have been diluted to 1% to avoid too long computing time, and because of the large amount of memory required by the adopted algorithm (that is optimised with a parallel chain-mesh code (Marulli et al., 2017)). Figure 5.2 presents the density contrast profiles obtained for voids traced by haloes and DM particles, computed from the void centres. The density profiles for each accepted effective radial bin, are shown with corresponding errors. In figure 5.3 we report again the density profiles (this time without error bars for clarity reasons) and the values of the ratio $\delta_{halo}/\delta_{DM}$ for each radial bin, comparing the slope with the bias value predicted by the theory.

These plots show a clear discrepancy between the theoretical effective bias measured at large scales, and the one computed as $\delta_{halo}/\delta_{DM}$ inside the detected cosmic voids. To shed light on this phenomenon, we investigate the trend of $\delta_{halo}(\delta_{DM})$ for each mass cut and for each radial bin, measuring the slope with a weighted fit. From now on, we consider the bias value estimated with the MCMC modelling technique.

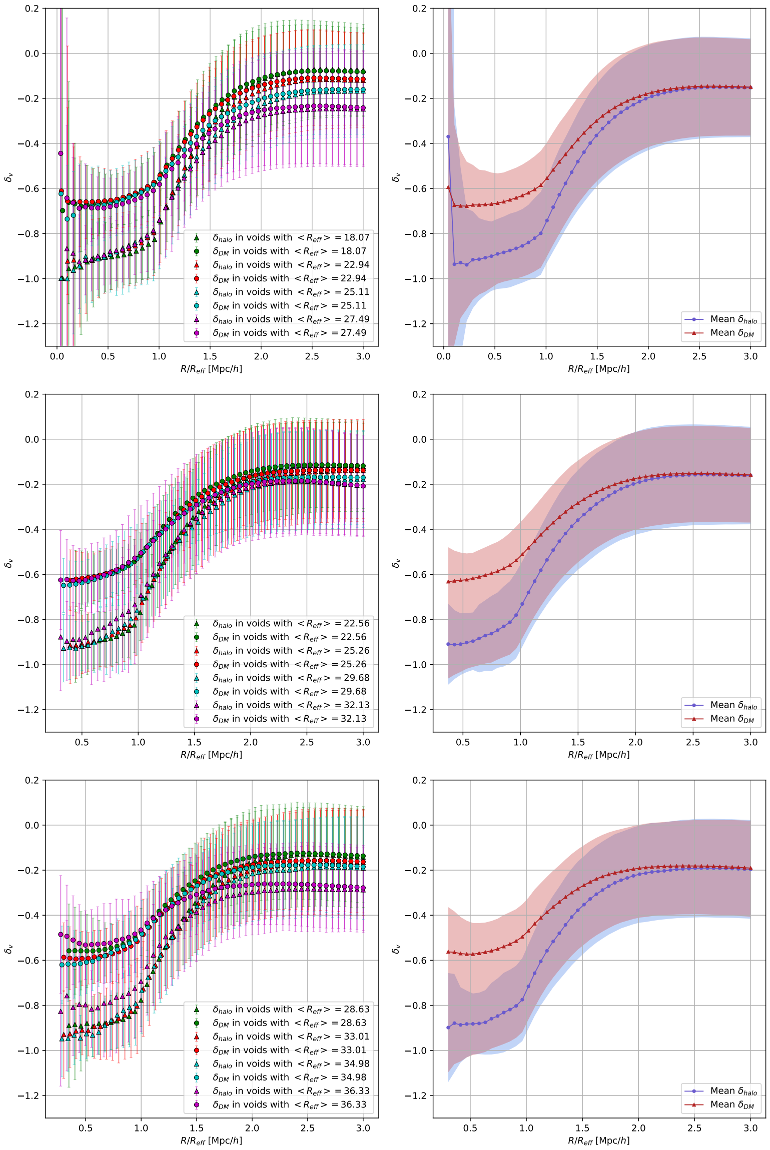

Figure 5.2: Comparison between halo and DM density contrast profiles considering halo catalogues with different mass cuts: $2 \cdot 10^{12}\ M_\odot/h$ (*upper panel*), $5 \cdot 10^{12}\ M_\odot/h$ (*middle panel*) and $10^{13}\ M_\odot/h$ (*lower panel*). In the *left* panels the halo and DM density contrast profiles are represented as a function of the distance from the void centre, in units of the effective void radius in the bin. Each profile is plotted with the corresponding error bars, computed as the standard deviation on the mean value in the bin. In the *right* panels the same profiles, but averaged considering all the profiles of the same type (red for DM and blue for haloes), are shown. The shaded regions correspond to the mean errors.

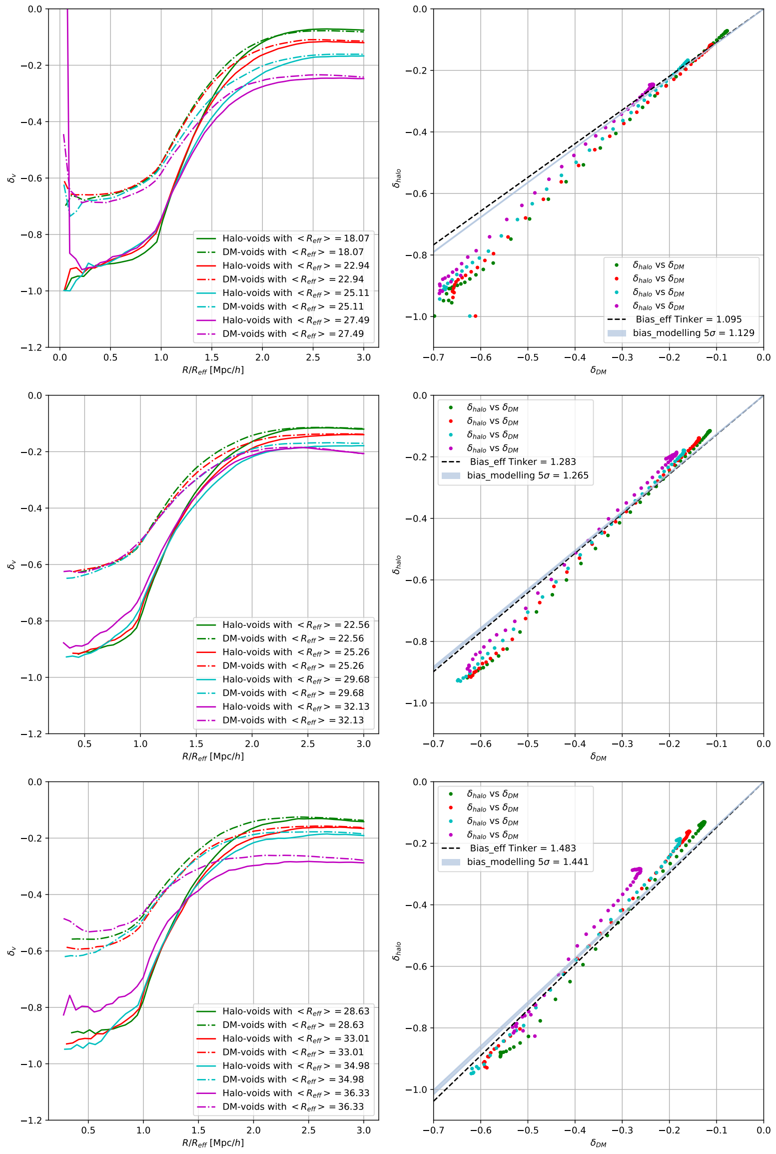

Figure 5.3: Comparison between halo and DM density contrast profiles considering halo catalogues with different mass cuts: $2 \cdot 10^{12}\ M_\odot/h$ (*upper panel*), $5 \cdot 10^{12}\ M_\odot/h$ (*middle panel*) and $10^{13}\ M_\odot/h$ (*lower panel*). In the *left* panels we report the halo and DM density contrast profiles divided by the mean effective void radius. In the *right* panels the values of δ computed for haloes and DM are plotted one against each other. Since the slope represents the bias, also the theoretical bias predictions are shown.

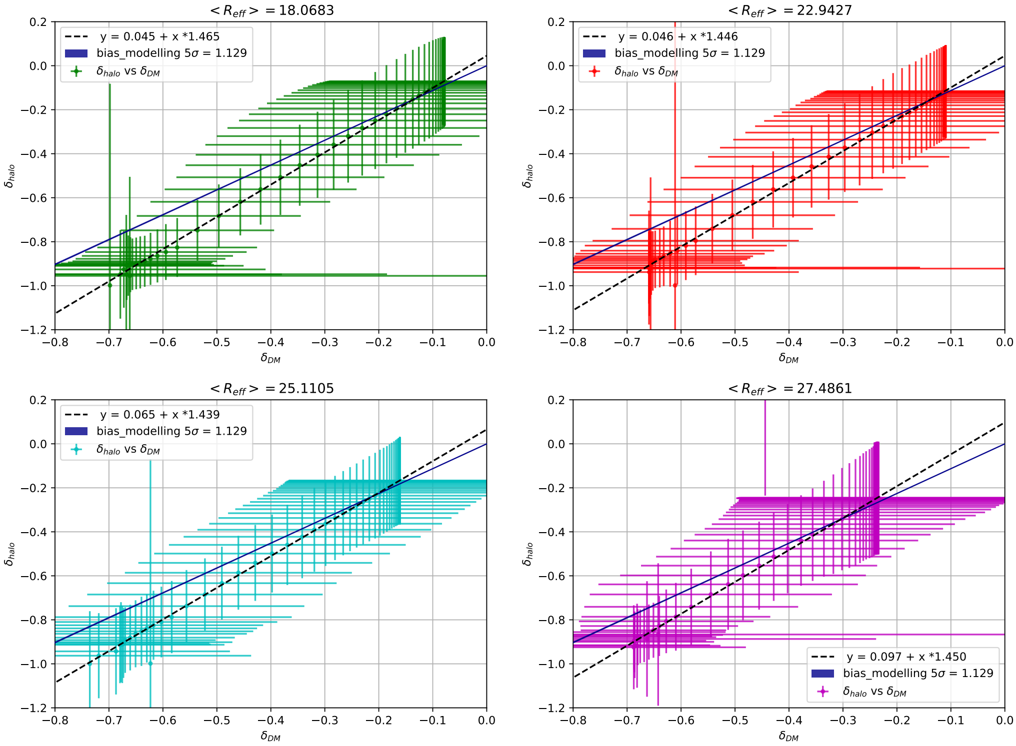

Figure 5.4: δ_{halo} vs δ_{DM} obtained for halo catalogues with a minimum of $2 \cdot 10^{12}\ M_\odot/h$. In each panel we show the results obtained from the profiles belonging to a specific bin of R_{eff} (the corresponding $\langle R_{eff} \rangle$ is reported above each plot) with errors computed as standard deviation. We also show the comparison between the weighed fit and the slope assessed from the modelling of the 2PCF.

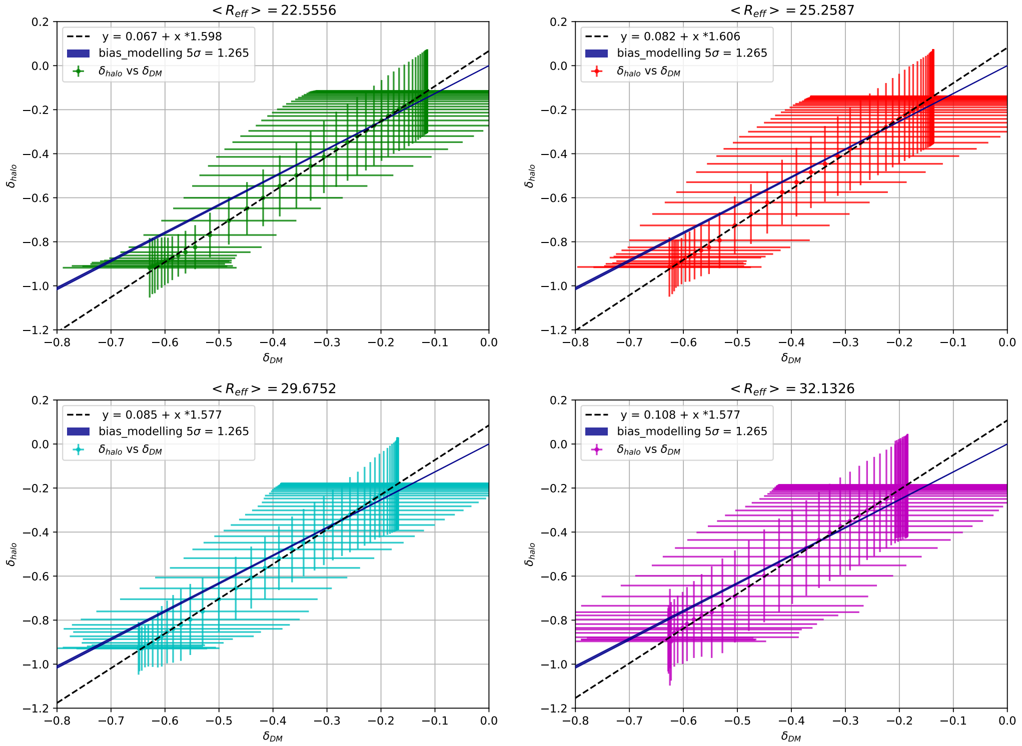

Figure 5.5: Same as figure 5.4, but for halo catalogues cutted to a minimum of mass of $5 \cdot 10^{12}\ M_\odot/h$.

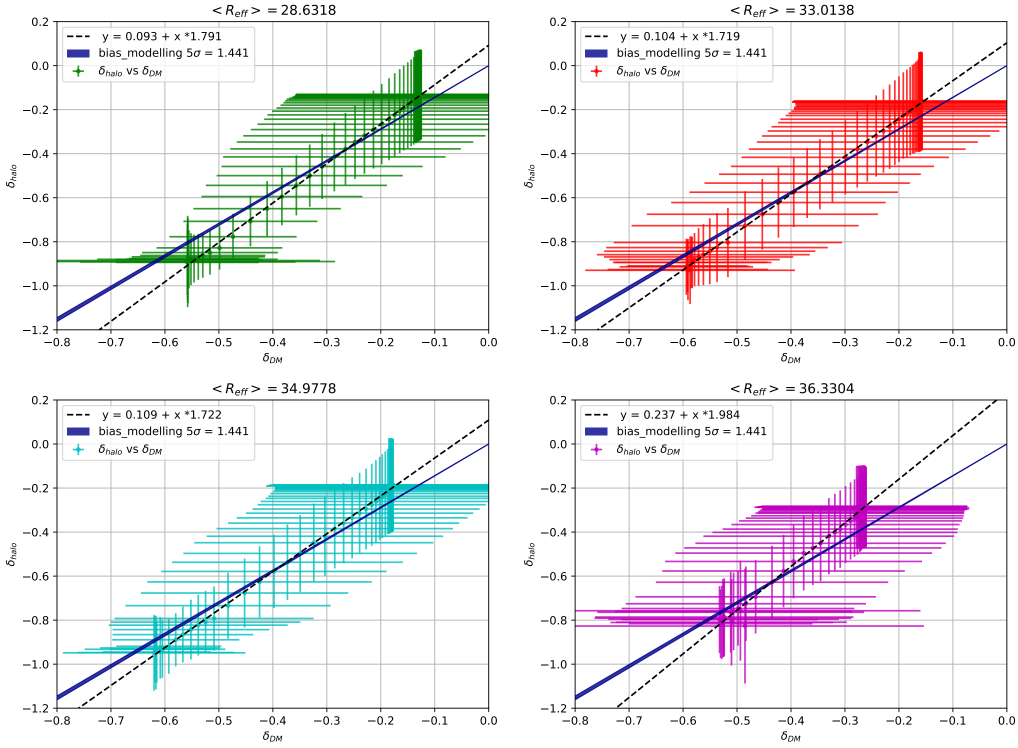

Figure 5.6: Same as figure 5.4, but for halo catalogues cutted to a minimum of mass of 10^{13} $M_\odot/h$.

5.4 Comparison between different bias estimates

Now it is important to highlight some of the main properties emerging from the previous plots:

- the ratio $\delta_{halo}/\delta_{DM}$ shows a well defined linear relation;
- the theoretical slope, i.e. the effective large-scale linear bias of the tracers, differs from the one obtained with a weighed fit (b_{slope});
- for every mass cut, the value of the slope of the fit seems to remain almost constant when the effective void radius is varied.

The latter point constitutes a quite unexpected result. Unfortunately, for each mass cut only 4 bins of effective radii are available, so we can not deduce reliable results from this analysis. Anyway, we can suppose that the trend of b_{slope} is independent of R_{eff}, at least in the restricted R_{eff} range considered. This is supported by figure 5.7, where we present the trend of b_{slope} as a function of R_{eff} for each mass cut, fitting the data with a constant. Except for the lower panel of figure 5.7, that shows a point deviating from this trend, b_{slope} seems to be almost constant with R_{eff}.

b_{slope} is the value we have to use to compute the theoretical void size function. When dealing with real catalogues, we usually have no access to the underling DM distribution, so we are not able to compute the bias as the ratio between the density contrasts of tracers and DM. For this reason, it is mandatory to find a relation between the linear effective bias (b_{eff}), measurable from the 2PCF at large scales, and the bias inside cosmic voids (b_{slope}). Figure 5.8 shows the mean value of b_{slope} as a function of b_{eff} for the three mass selections. The data have been fitted with a first-order polynomial. This represents a preliminary study that we plan to extend in the near future using a larger set of mock catalogues to accurately calibrate the relation. We will also investigate how this relation depends on redshift and on the cosmological parameters.

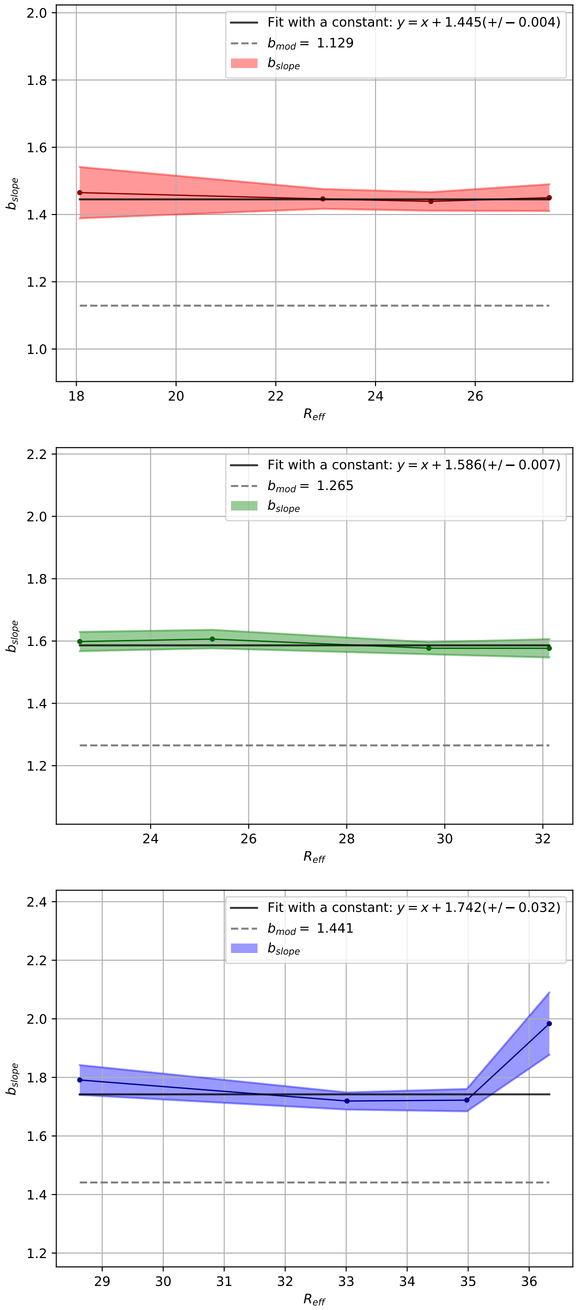

Figure 5.7: Trend of b_{slope} as a function of R_{eff} for each mass cut: with a minimum of $2 \cdot 10^{12}$ $M_\odot/h$ (*upper panel*), with a cut to a minimum of $5 \cdot 10^{12}$ $M_\odot/h$ (*middle panel*) and 10^{13} $M_\odot/h$ (*lower panel*). The shaded area represents a 5σ error (i.e. 5 times the error obtained fitting the data). The black solid line indicates the value of the weighted fit, while the grey dashed one represents the value of the bias obtained from the theoretical modelling.

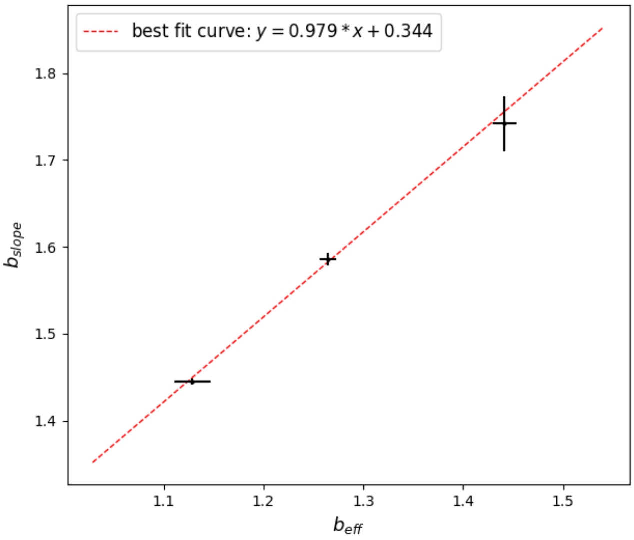

Figure 5.8: The behaviour of b_{slope} as a function of b_{eff} for each mass cut. The data are fitted with a first-order polynomial, weighting the data with the reciprocal of the errors (red dashed line).

5.5 Tests with uncleaned catalogues

Now we want to perform the same procedure described in the previous sections but applied, this time, to the void catalogues that have not been processed with the cleaning algorithm. In this way we want to check if the application of the cleaning procedure has unexpected consequences on the estimate of the bias inside voids.

First, we compute the mean density profiles for the uncleaned void catalogues extracted from the halo distribution with the following mass-cuts: *(i)* with a minimum of $2 \cdot 10^{12}\ M_\odot/h$, *(ii)* with a cut to a minimum of $5 \cdot 10^{12}\ M_\odot/h$) and *(iii)* $10^{13}\ M_\odot/h$. The results are showed in figure 5.9. As we can see from these plots, also in this case the profiles have a well-defined shape, as predicted by Hamaus et al. (2016). The main difference with respect to the profiles obtained with the cleaned catalogues is the value of the effective void radius. When the cleaning algorithm is applied, the radius of the voids extracted from the halo catalogues matches the density contrast of the shell-crossing $\delta_{sc} = -0.795$. Instead, analysing the profiles obtained with the uncleaned catalogues, we can see that the values of the void radii are shifted towards the compensation wall.

Figure 5.10 compares the DM and halo density constrast profiles in the two analysed cases, to make a direct comparison between the void profiles in cleaned and uncleaned void catalogues.

Finally, analogously to what we have done with the cleaned void catalogues, we estimated the tracer bias inside the cosmic voids extracted from the uncleaned catalogue, making use of equation (4.6). In this case, since the cleaning procedure has not been applied, there are more voids in the catalogues and their radii reach greater values. Therefore, we are able to evaluate the value of b_{slope} on larger ranges of radii. As we can see from figure 5.11, the trend of b_{slope} is still independent of the mean effective void radii, even in this larger radial range analysed. Also in this case, we found that b_{slope} is systematically larger than b_{eff}.

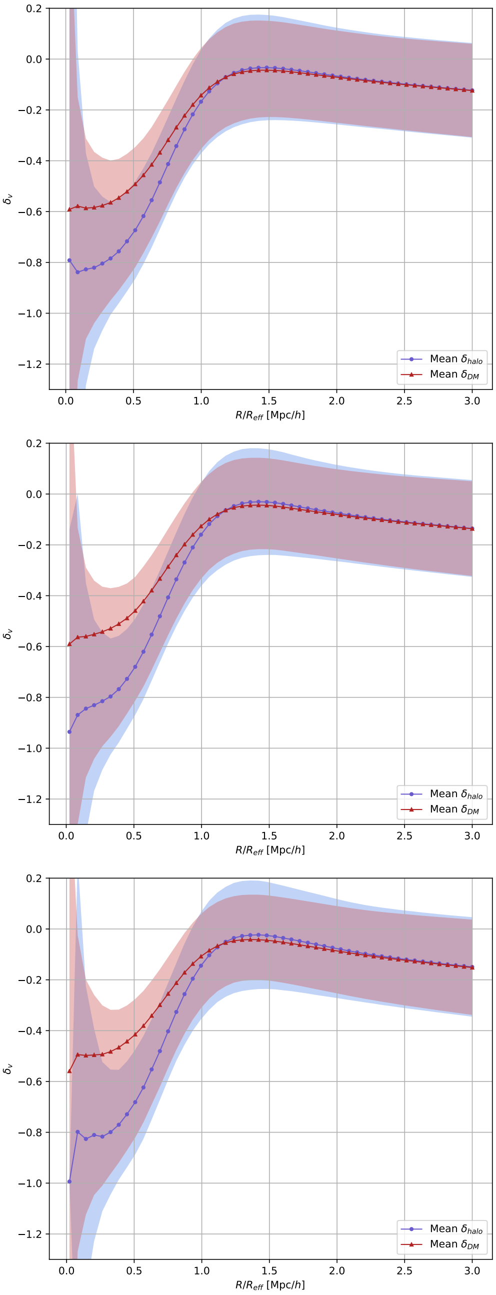

Figure 5.9: Comparison between halo and DM density contrast profiles obtained with uncleaned halo catalogues with different mass cuts: $2 \cdot 10^{12}\ M_{\odot}/h$ (*upper panel*), $5 \cdot 10^{12}\ M_{\odot}/h$ (*middle panel*) and $10^{13}\ M_{\odot}/h$ (*lower panel*). In these plots we show the halo (*blue*) and DM (*red*) mean density contrast profiles as a function of the radius, divided by the effective void radius. The shaded regions show to the errors on the mean.

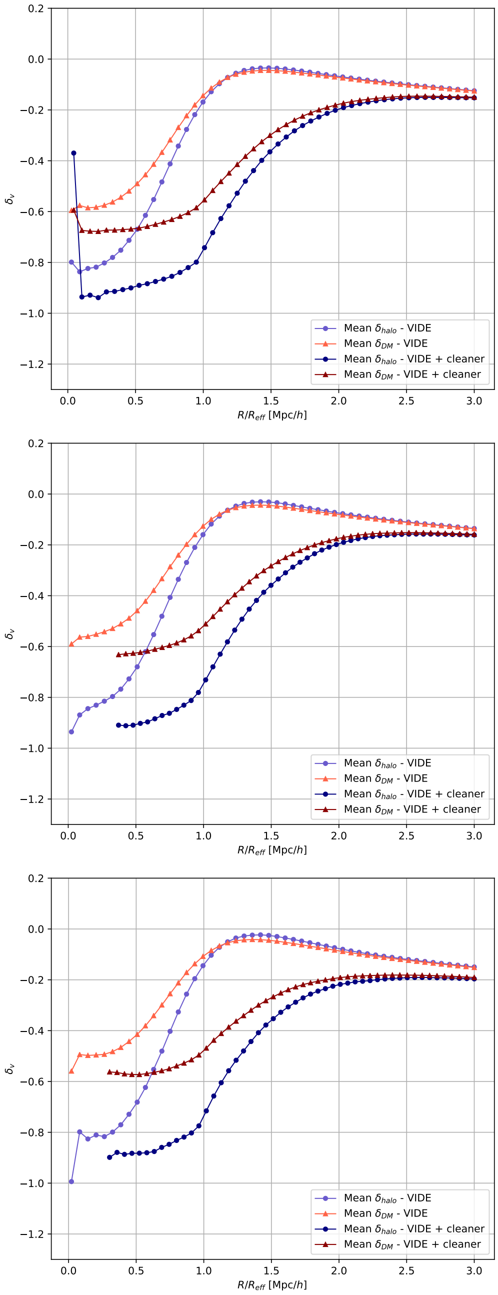

Figure 5.10: Comparison between halo and DM density contrast profiles obtained with cleaned and uncleaned halo catalogues, for different mass cuts: $2 \cdot 10^{12}\ M_{\odot}/h$ (*upper panel*), $5 \cdot 10^{12}\ M_{\odot}/h$ (*middle panel*) and $10^{13}\ M_{\odot}/h$ (*lower panel*). The profiles computed for the cleaned catalogues are represented in blue and in red for the haloes and DM distribution, respectively. Instead, the profiles obtained from the uncleaned catalogues are represented in orange and violet for the haloes and DM distribution, respectively.

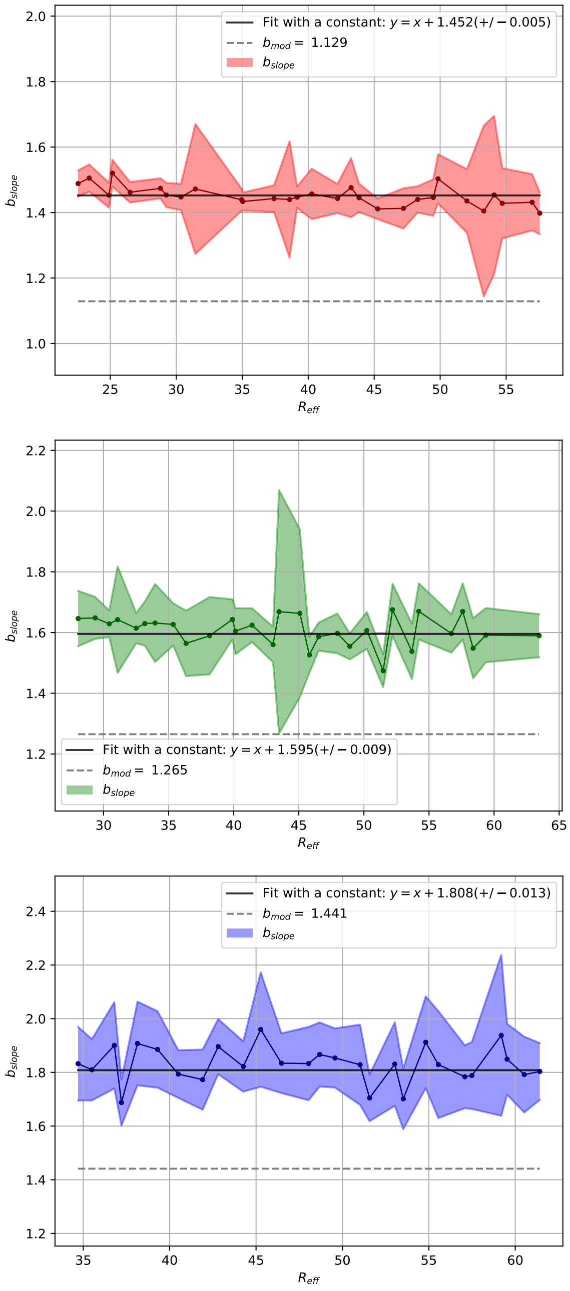

Figure 5.11: Trend of b_{slope} as an function of R_{eff} for uncleaned halo catalogues with the following mass cuts: $2 \cdot 10^{12}\ M_{\odot}/h$ (*upper panel*), $5 \cdot 10^{12}\ M_{\odot}/h$ (*middle panel*) and $10^{13}\ M_{\odot}/h$ (*lower panel*). The shaded area represents a 5σ error (i.e. 5 times the error obtained by fitting the data). The black solid line indicates the value of the weighted fit, while the grey dashed one represents the value of the bias obtained from the theoretical modelling.

5.6 Size function of voids from biased tracers

After this deep analysis of the tracer bias, both in the entire data sample and inside the cosmic voids, we are now ready to re-parametrise the theoretical void size function, in order to predict the size distribution of voids identified in the distribution of biased tracers. First, it is useful to remember the effect of the cleaning algorithm (see section 3.3) on the void catalogues. This procedure re-scales the void radii to a fixed threshold $\delta_{sc} = -0.795$, related to the phenomenon of the shell-crossing, which identifies the formation of a void. This value is predicted by the spherical evolution model (see section 1.6.4) but it refers to voids identified in the DM distribution. So, applying the cleaning algorithm on voids extracted from catalogue of biased tracers, the void radii will be re-scaled to the density contrast defined for the DM. This fact does not constitutes an inconsistency, as long as the theoretical size function is computed with this parameter.

Assuming the validity of the Vdn model (see section 2.3), we have to re-scale the density contrast threshold used to define the voids in the DM distribution. We have demonstrated that the DM density field within voids, $\delta^{NL}_{v,\,\mathrm{DM}}$, is linearly related to the density field defined by some biased tracer, $\delta^{NL}_{v,\,\mathrm{tr}}$, by a specific value of b (assumed to be a simple multiplicative constant):

$$\delta^{NL}_{v,\,\mathrm{tr}} = b\,\delta^{NL}_{v,\,\mathrm{DM}} \quad , \tag{5.1}$$

where the superscripts indicate that the values are computed in the non-linear theory. Therefore, dealing with catalogues of biased tracers, we have to re-scale the threshold density employed in the Vdn model following this relation. Since the Vdn model is computed with the density contrast in linear theory, we have to recover the linearly extrapolated value $\delta^{L}_{v,\,\mathrm{tr}}$. To do this, we use the fitting formula provided by Bernardeau (1994), which combined with equation (5.1), gives:

$$\delta^{L}_{v,\,\mathrm{tr}} = \mathcal{C}\left[1 - (1 + b\,\delta^{NL}_{v,\,\mathrm{DM}})^{-1/\mathcal{C}}\right] \;, \tag{5.2}$$

with $\mathcal{C} = 1.594$.

An alternative procedure to what we proposed in this section is the following. Instead of re-parametrise the Vdn model by ensuring that it predicts the size function of voids identified in biased tracers, we could re-scale properly the void radii making use of the cleaner algorithm. In particular, assuming that $\delta_{sc} = -0.795$ is the density contrast that defines the formation of a void in the DM distribution, we could simply change this threshold consistently with the bias value. In practice, we could find the density contrast at which a void extracted from the distribution of biased tracers reaches the same radius value of a void identified in the DM distribution. The problem with this method is that the density threshold we have to give to the cleaning algorithm should be computed as $\delta_{v,tr}^{NL} = -0.795\, b$ which, for high values of b ($b \gtrsim 1.258$), leads to $\delta_{v,tr}^{NL} < -1$. Since this implies a negative density within the void, this value is obviously not physical. It actually implies that we have reached a limit under which the tracers in the biased catalogue are not enough to give a reliable estimate of the density field. Thus, with this alternative method we could just give an upper limit to the void effective radii in samples with a bias value greater than 1.258. Therefore, re-parameterising the void size function is the only viable way to proceed in order to take into account the effect of bias in the size distribution of voids. The schematic procedure of these two different approaches is represented in figure 5.12.

Having re-parametrised the model in this way, we can now plot the size function of voids extracted from the halo catalogues, as described in section 2.3. The size functions are compute both with b_{slope} and with b_{eff} in order to make a comparison. The final results are reported in Figures 5.13, 5.14 and 5.15.

What clearly emerges from these plots is that b_{slope} represents a much more appropriate bias value in void environments. The theoretical size functions computed with this value is fully consistent with the measured size distribution of voids, contrary to the one computed with b_{eff}.

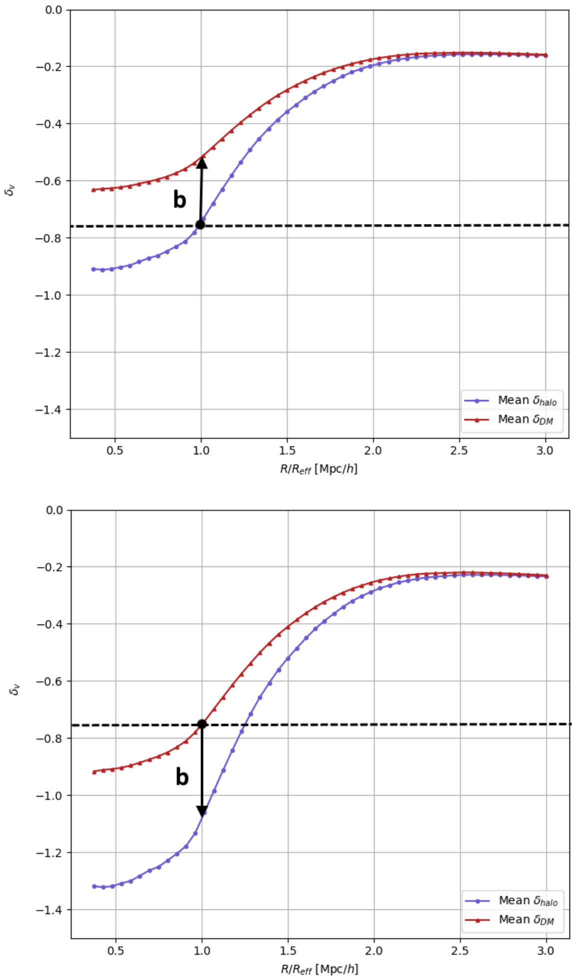

Figure 5.12: In the *upper panel* we show the procedure we applied in our work. It consists in rescaling the value of the void radii in order to match the density contrast corresponding to the value of the shell-crossing $\delta^{NL}_{v,tr} = -0.795$, represented by a black dotted line. In order to recover the size distribution of voids, the theoretical size function has then to be re-parametrised using b. In the *bottom panel* we show the alternative procedure that we discarded. In this case the void catalogue is cleaned to match the density contrast corresponding to $\delta^{NL}_{v,tr} = -0.795\ b$. In this way the model of the size function does not need a re-parametrisation, but, as it can be seen in this plot, for large values of b the density contrast can reach unphysical values (i.e. $\delta < -1$).

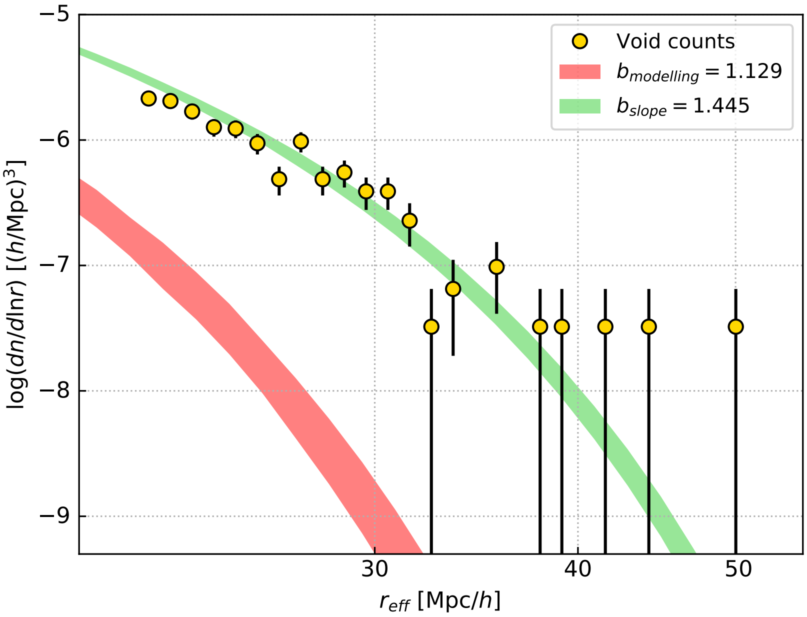

Figure 5.13: Size function of voids extracted from halo catalogues with a minimum mass of $2 \cdot 10^{12}$ $M_{\odot}/h$. The yellow dots represent the measured size function of voids in the catalogue, with relative uncertainties. Voids with $R_{eff} < 2.5$ times the mean inter-particle separation are rejected from the analysis. The green and red shaded areas represent the value of the theoretical size function computed with b_{slope} and with b_{eff} respectively, both with errors of 5σ.

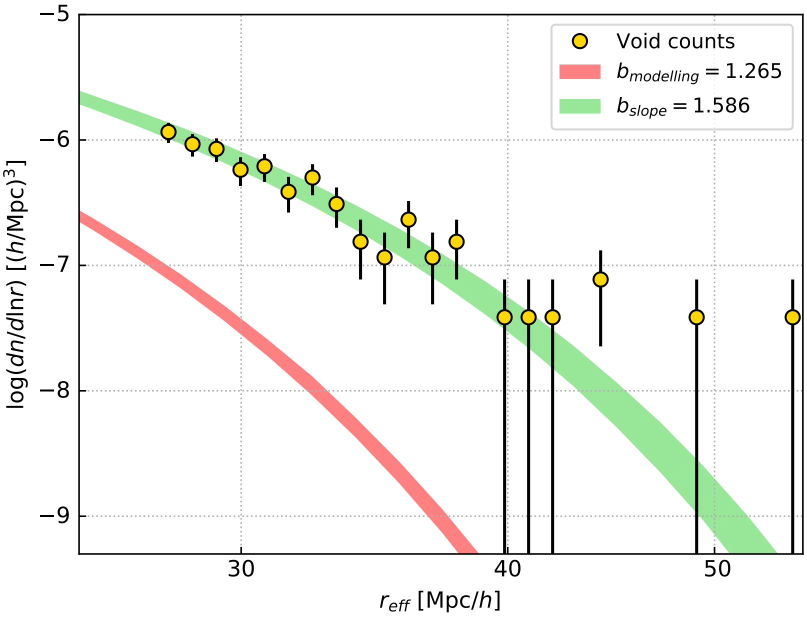

Figure 5.14: As figure 5.13, but for voids extracted from halo catalogues with a minimum mass of $5 \cdot 10^{12}\ M_\odot/h$.

5.7 Effects of the main cosmological parameters on the void size function

Finally, we investigate the effect of the main cosmological parameters on the void size function, paving the way for a forthcoming cosmological exploitation on real data. In particular, in this preliminary study, we consider three cosmological parameters of the ΛCDM model, σ_8, Ω_{DE} and Ω_m, investigating the effect of the variation of each of these quantities taken individually. The WMAP7 model is taken as the reference cosmological model for this analysis (see Table 5.1).

Figures 5.16, 5.17, 5.18 show the effect of varying these cosmological parameters in the void size function model by $\pm 1\sigma$, $\pm 3\sigma$ and $\pm 5\sigma$. Specifically, we show the size function of the cosmic voids detected from the DM halo mock catalogue with a minimum mass cut of $2 \cdot 10^{12}\ M_\odot/h$. Voids with $R_{eff} < 2.5$ times the mean inter-particle separation are rejected from the analysis. The Vdn model shown is re-parametrised with b_{slope} assuming WMAP7 cosmological parameters.

As these plots demonstrate, the variation of Ω_M produces more relevant differences on the theoretical size function, while the variation of σ_8 and Ω_{DE}

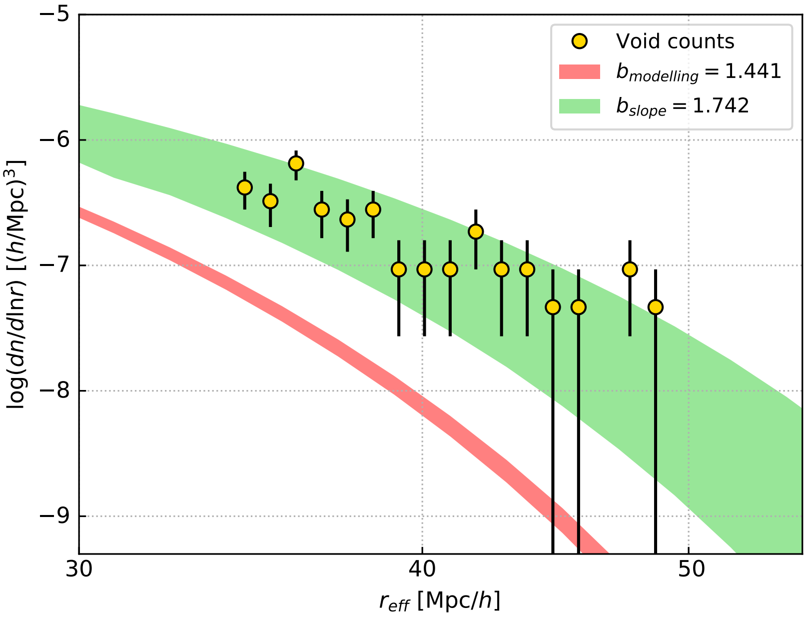

Figure 5.15: As figure 5.13, but for voids extracted from halo catalogues with a minimum mass of 10^{13} $M_\odot/h$.

causes comparable effects. Overall, the theoretical void size function is quite sensitive to the variation of the cosmological parameters considered. This statistics thus provides a powerful cosmological probe that will be exploited to put constraints to these parameters, and possibly to discriminate among alternative cosmological frameworks.

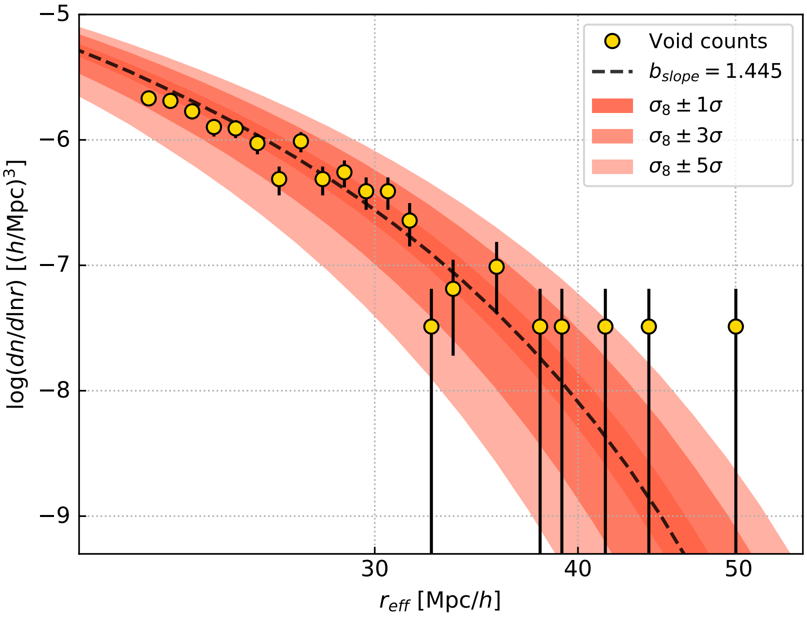

Figure 5.16: The size function of the cosmic voids detected from the DM halo mock catalogue with a minimum mass cut of $2 \cdot 10^{12}\ M_{\odot}/h$. The yellow dots represent the measured void size function, with relative uncertainties. Voids with $R_{eff} < 2.5$ times the mean inter-particle separation are rejected from the analysis. The black dashed line represents the Vdn model re-parametrised with b_{slope} (considered without uncertainties), assuming WMAP7 cosmological parameters, while the shaded regions show the predictions obtained by varying σ_8 by $\pm 1\sigma$, $\pm 3\sigma$ and $\pm 5\sigma$, where σ is the WMAP7 estimated uncertainty.

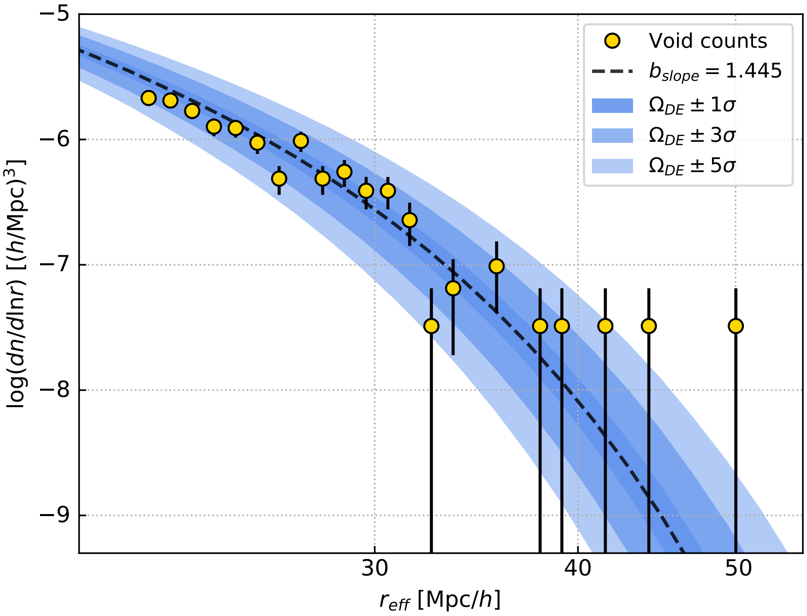

Figure 5.17: Same as figure 5.16, but for Ω_{DE}.

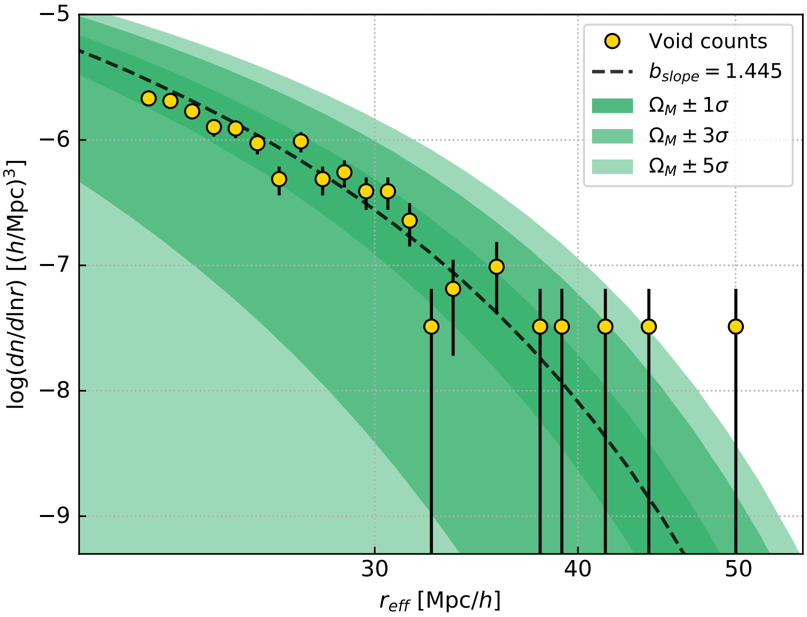

Figure 5.18: Same as figure 5.16, but for Ω_M.

Chapter 6

Discussion and conclusions

In this chapter we report the outline of this thesis work, recalling the scientific background on which it is based and depicting the importance of cosmic voids as cosmological probes. Then we summarise the obtained results, highlighting how they constitute a breakthrough and a development of the already existing methods to inspect the voids statistics. Finally, we propose some possible developments for our work, that will be extended also thanks to the new advancements that the future surveys will provide.

6.1 The scientific problem

The currently accepted flat-ΛCDM Standard Cosmological Model (described in section 1.5) is based on the solution of the Einstein's Field Equations, assuming the validity of the cosmological principle (see section 1.2). This model predicts the accelerating expansion and the flatness of the Universe and accounts for the existence of two major components, the cold DM and the dark energy. Despite the theoretical framework of the Standard Cosmological Model is well defined and generally accepted by the scientific community, there are still unresolved issues. They span from the understanding of the nature of DM and DE, to the physical description of the inflationary models and of the accelerated expansion.

The Standard Model is characterised by a set of cosmological parameters, which are constrained by constantly improving experiments. These parameters describe the energy content of the Universe and the primordial density fluctuation distribution, determining the characteristics of present-day large scale structures. Being galaxy clusters among the largest virialised structures of the Universe, their statistical properties can be effectively exploited to put constraints on the main cosmological parameters. This is generally performed by studying number counts, density profiles and clustering.

Analogously to galaxy clusters, it is possible to exploit cosmic voids as cosmological probes. In particular, voids emerge from the troughs of the primordial Gaussian field of density fluctuations and are among the largest structures of the Universe (with radii up to tens of Mpc). Their great potential for constraining DE and testing theories of gravity has already been widely demonstrated (see e.g. Pisani et al., 2015; Sahlén and Silk, 2016; Pollina et al., 2016; Hawken et al., 2017). The identification of voids is obviously not trivial because they are substantially underdense regions, so their centres and dimensions have to be derived from the discrete density field traced by luminous sources (e.g. galaxies and galaxy clusters). On the other hand, the cosmological exploitation of voids provides some relevant advantages with respect to the galaxy cluster one. In particular, voids are for their nature only mildly non-linear, since they are physically limited by a minimum of density contrast given by $\delta = -1$. This suggests that their evolution should be easier to reconstruct than the one of their positive counterparts, which can reach extremely non-linear amplitudes instead. Moreover, voids tend to be more spherical as they expand (Icke, 1984), so that the spherical evolution approximation should optimally describe their development. Despite their recently-gathered popularity in the scientific community, a gap of knowledge between the theoretical modelling of voids and their effective exploitation as cosmological probes still remains. In fact, though the model of size function proposed by Jennings et al. (2013) (see section 2.3), combined with the cleaning procedure developed by Ronconi and Marulli (2017) (see section 3.3), is able to predict accurately the void number counts in DM particle simulations, it fails in case cosmic voids are selected using biased mass tracers. This undermines the possibility of applying voids to real data (like galaxy catalogues), since they are naturally affected by a bias connecting the distribution of objects to the one of the underlying total mass. The aim of this thesis work is to develop a re-parametrisation of the existent theoretical void size function in order to correctly predict the size distribution of voids extracted from tracer catalogues. This procedure consists in re-scaling properly the density contrast threshold of the theoretical model in relation to the value of the linear effective bias of the tracers used to detect the voids. This constitutes the fundamental basis to extend the cosmological exploitation of voids to real data catalogues.

6.2 Procedure and results

In our work we made use of high-resolution N-body simulations, from which DM halo catalogues are extracted with a friend-of-friend algorithm. We applied different mass cuts in order to build halo catalogues composed by DM haloes with different values of the parameter bias. Among all the available void finders, we chose to employ VIDE, which identifies void centres as the minima of the density field. Our void catalogues have then been cleaned with the technique described in section 3.3. This procedure has the aim of removing from the the catalogues the spurious voids and re-scale void radii to a defined density threshold, in order to make them directly comparable to the model predictions.

Once the void catalogues are built and cleaned, we estimated the bias of the halo catalogues with different methods. Specifically, we made use of the functions implemented in the CBL in order to evaluate the linear effective bias, b_{eff}. Since the different techniques tested produced results consistent with each other, we chose to rely on the estimate of bias obtained with the modelling of the redshift-space 2PCF. We performed a MCMC posterior sampling technique in order to assess an accurate measure of the bias and of its statistical error. With these results we performed a re-parametrisation of the Vdn model, re-scaling the density contrast threshold according to the value of the effective bias. What we found with this prescription is an under-prediction of the size distribution of voids. In fact, according to Pollina et al. (2017, 2018), the value of the bias measured inside cosmic voids differs from the linear effective bias, for the small voids analysed in this work. In particular, we computed the bias inside voids as the ratio between the density contrasts of halos and the one of the underlying DM particles (we called this parameter b_{slope}, as in Pollina et al. (2018)), founding that this value is systematically larger than b_{eff}. Using the bias computed inside voids, we verified that the re-parametrised theoretical size function is fully consistent with the void size function measured in our simulations, for all the halo catalogues analysed.

The method proposed has then been exploited to investigate the cosmological constraining power of the void size function. In particular, varying the cosmological parameters with which the theoretical size function is computed, we could determine their effect on the void statistics. Finally, we searched for a relation between b_{eff} and b_{slope}, performing a weighted fit of our data. Having an accurately calibrated relation between these parameters is crucial in the perspective of extending this methodology to the real case. In fact, dealing with real data catalogues, it can be challenging to measure the value of bias inside voids, since it is not easy to investigate the underlying

DM distribution. On the other hand, the effective bias can be accurately estimated from clustering. Therefore, having an accurate relation between these parameters, we will be able to compute the theoretical void size function once the linear effective bias has been estimated from the theory.

6.3 Future perspectives

We are now ready to exploit the proposed method to derive cosmological constraints from void catalogues extracted from real data. In the next future, we will use larger and higher resolution simulations to investigate more accurately the relation between b_{eff} and b_{slope}. We will extend our work to different tracer catalogues with different redshifts, examining also alternative cosmological scenarios. Finally, we will exploit this technique on real void catalogues, such as the SDSS DR12 BOSS Void Catalogue (Mao et al., 2017), to improve current cosmological constraints, and possibly discriminate between alternative cosmological frameworks. Moreover, we will also provide forecasts for future missions, like Euclid (Laureijs et al., 2011; Amendola et al., 2013, 2018) and Large Synoptic Survey Telescope (LSST) (Graham et al., 2018; Ivezić, 2017; Abate et al., 2011).

Bibliography

A. Abate, A. Gorecki, R. Ansari, A. Barrau, S. Baumont, L. Derome, E. Gawiser, C. Magneville, M. Moniez, J. A. Newman, J. A. Tyson, H. Zhan, and LSST LSS Science Collaboration. Baryon Acoustic Oscillations in the LSST Photometric Survey. In *American Astronomical Society Meeting Abstracts #217*, volume 43 of *Bulletin of the American Astronomical Society*, page 252.19, Jan. 2011.

C. Alcock. The Search for MACHOS in the Galactic Dark Matter. In T. Kajino, Y. Yoshii, and S. Kubono, editors, *Origin of Matter and Evolution of Galaxies in the Universe '96*, page 101, 1997.

S. W. Allen, R. W. Schmidt, H. Ebeling, A. C. Fabian, and L. van Speybroeck. Constraints on dark energy from Chandra observations of the largest relaxed galaxy clusters. *Mon. Not. R. Astron. Soc.*, 353:457–467, Sept. 2004. doi: 10.1111/j.1365-2966.2004.08080.x.

L. Amendola, S. Appleby, D. Bacon, T. Baker, M. Baldi, N. Bartolo, A. Blanchard, C. Bonvin, S. Borgani, E. Branchini, C. Burrage, S. Camera, C. Carbone, L. Casarini, M. Cropper, C. de Rham, C. Di Porto, A. Ealet, P. G. Ferreira, F. Finelli, J. García-Bellido, T. Giannantonio, L. Guzzo, A. Heavens, L. Heisenberg, C. Heymans, H. Hoekstra, L. Hollenstein, R. Holmes, O. Horst, K. Jahnke, T. D. Kitching, T. Koivisto, M. Kunz, G. La Vacca, M. March, E. Majerotto, K. Markovic, D. Marsh, F. Marulli, R. Massey, Y. Mellier, D. F. Mota, N. J. Nunes, W. Percival, V. Pettorino, C. Porciani, C. Quercellini, J. Read, M. Rinaldi, D. Sapone, R. Scaramella, C. Skordis, F. Simpson, A. Taylor, S. Thomas, R. Trotta, L. Verde, F. Vernizzi, A. Vollmer, Y. Wang, J. Weller, and T. Zlosnik. Cosmology and Fundamental Physics with the Euclid Satellite. *Living Reviews in Relativity*, 16: 6, Sept. 2013. doi: 10.12942/lrr-2013-6.

L. Amendola, S. Appleby, A. Avgoustidis, D. Bacon, T. Baker, M. Baldi, N. Bartolo, A. Blanchard, C. Bonvin, S. Borgani, E. Branchini, C. Burrage, S. Camera, C. Carbone, L. Casarini, M. Cropper, C. de Rham, J. P.

Dietrich, C. Di Porto, R. Durrer, A. Ealet, P. G. Ferreira, F. Finelli, J. García-Bellido, T. Giannantonio, L. Guzzo, A. Heavens, L. Heisenberg, C. Heymans, H. Hoekstra, L. Hollenstein, R. Holmes, Z. Hwang, K. Jahnke, T. D. Kitching, T. Koivisto, M. Kunz, G. La Vacca, E. Linder, M. March, V. Marra, C. Martins, E. Majerotto, D. Markovic, D. Marsh, F. Marulli, R. Massey, Y. Mellier, F. Montanari, D. F. Mota, N. J. Nunes, W. Percival, V. Pettorino, C. Porciani, C. Quercellini, J. Read, M. Rinaldi, D. Sapone, I. Sawicki, R. Scaramella, C. Skordis, F. Simpson, A. Taylor, S. Thomas, R. Trotta, L. Verde, F. Vernizzi, A. Vollmer, Y. Wang, J. Weller, and T. Zlosnik. Cosmology and fundamental physics with the Euclid satellite. *Living Reviews in Relativity*, 21:2, Apr. 2018. doi: 10.1007/s41114-017-0010-3.

J. S. Bagla and T. Padmanabhan. Cosmological N-body simulations. *Pramana*, 49:161, Aug. 1997. doi: 10.1007/BF02845853.

M. Baldi. The CoDECS project: a publicly available suite of cosmological N-body simulations for interacting dark energy models. *Mon. Not. R. Astron. Soc.*, 422:1028–1044, May 2012. doi: 10.1111/j.1365-2966.2012.20675.x.

F. Bernardeau. The nonlinear evolution of rare events. *Astrophys. J.*, 427: 51–71, May 1994. doi: 10.1086/174121.

G. R. Blumenthal, L. N. da Costa, D. S. Goldwirth, M. Lecar, and T. Piran. The largest possible voids. *Astrophys. J.*, 388:234–241, Apr. 1992. doi: 10.1086/171147.

J. R. Bond, S. Cole, G. Efstathiou, and N. Kaiser. Excursion set mass functions for hierarchical Gaussian fluctuations. *Astrophys. J.*, 379:440–460, Oct. 1991. doi: 10.1086/170520.

A. Bosma. Dark Matter in Disk Galaxies. In D. R. Merritt, M. Valluri, and J. A. Sellwood, editors, *Galaxy Dynamics - A Rutgers Symposium*, volume 182 of *Astronomical Society of the Pacific Conference Series*, Aug. 1999.

M. Bradač. Dark Matter: Revealing the Invisible with 2 Cosmic Supercolliders the Bullet Cluster 1E0657-56 and MACSJ0025-1222. *Nuclear Physics B Proceedings Supplements*, 194:17–21, Oct. 2009. doi: 10.1016/j.nuclphysbps.2009.07.002.

T. D. Brandt. Constraints on MACHO Dark Matter from Compact Stellar Systems in Ultra-faint Dwarf Galaxies. *Astrophys. J. Lett.*, 824:L31, June 2016. doi: 10.3847/2041-8205/824/2/L31.

C. Cannarozzo. *A new void finder based on cosmic dynamics*. PhD thesis. URL `http://amslaurea.unibo.it/12826/`.

T. Cannarozzo et al. . in preparation.

E. Castorina, C. Carbone, J. Bel, E. Sefusatti, and K. Dolag. DEMNUni: the clustering of large-scale structures in the presence of massive neutrinos. *J. Cosm. Astro-Particle Phys.*, 7:043, July 2015. doi: 10.1088/1475-7516/2015/07/043.

T. Clifton, P. G. Ferreira, A. Padilla, and C. Skordis. Modified gravity and cosmology. *Phys. Rept.*, 513:1–189, Mar. 2012. doi: 10.1016/j.physrep.2012.01.001.

J. M. Colberg, F. Pearce, C. Foster, E. Platen, R. Brunino, M. Neyrinck, S. Basilakos, A. Fairall, H. Feldman, S. Gottlöber, O. Hahn, F. Hoyle, V. Müller, L. Nelson, M. Plionis, C. Porciani, S. Shandarin, M. S. Vogeley, and R. van de Weygaert. The Aspen-Amsterdam void finder comparison project. *Mon. Not. R. Astron. Soc.*, 387:933–944, June 2008. doi: 10.1111/j.1365-2966.2008.13307.x.

G. Efstathiou, M. Davis, S. D. M. White, and C. S. Frenk. Numerical techniques for large cosmological N-body simulations. *Astrophys. J. Suppl.*, 57: 241–260, Feb. 1985. doi: 10.1086/191003.

G. Efstathiou, W. J. Sutherland, and S. J. Maddox. The cosmological constant and cold dark matter. *Nature*, 348:705–707, Dec. 1990. doi: 10.1038/348705a0.

A. Einstein. Zur allgemeinen Relativitätstheorie. *Sitzungsberichte der Königlich Preußischen Akademie der Wissenschaften (Berlin), Seite 778-786.*, 1915.

A. Elyiv, F. Marulli, G. Pollina, M. Baldi, E. Branchini, A. Cimatti, and L. Moscardini. Cosmic voids detection without density measurements. *Mon. Not. R. Astron. Soc.*, 448:642–653, Mar. 2015. doi: 10.1093/mnras/stv043.

A. A. Elyiv, I. D. Karachentsev, V. E. Karachentseva, O. V. Melnyk, and D. I. Makarov. Low-density structures in the Local Universe. II. Nearby cosmic voids. *Astrophysical Bulletin*, 68:1–13, Jan. 2013. doi: 10.1134/S199034131301001X.

J. E. Forero-Romero, Y. Hoffman, S. Gottlöber, A. Klypin, and G. Yepes. A dynamical classification of the cosmic web. *Mon. Not. R. Astron. Soc.*, 396:1815–1824, July 2009. doi: 10.1111/j.1365-2966.2009.14885.x.

B. Fuchs. The Amount of Dark Matter in Spiral Galaxies. In H. V. Klapdor-Kleingrothaus, editor, *Dark Matter in Astro- and Particle Physics*, page 25, 2001.

S. Galli, F. Iocco, G. Bertone, and A. Melchiorri. Updated CMB constraints on dark matter annihilation cross sections. *Phys. Rev. D*, 84(2):027302, July 2011. doi: 10.1103/PhysRevD.84.027302.

D. Gilman, S. Birrer, T. Treu, C. R. Keeton, and A. Nierenberg. Probing the nature of dark matter by forward modeling flux ratios in strong gravitational lenses. *Mon. Not. R. Astron. Soc.*, Aug. 2018. doi: 10.1093/mnras/sty2261.

M. L. Graham, A. J. Connolly, Ž. Ivezić, S. J. Schmidt, R. L. Jones, M. Jurić, S. F. Daniel, and P. Yoachim. Photometric Redshifts with the LSST: Evaluating Survey Observing Strategies. *Astron. J.*, 155:1, Jan. 2018. doi: 10.3847/1538-3881/aa99d4.

A. H. Guth. Inflationary universe: A possible solution to the horizon and flatness problems. *Phys. Rev. D*, 23:347–356, Jan. 1981. doi: 10.1103/PhysRevD.23.347.

A. H. Guth and S.-Y. Pi. Fluctuations in the new inflationary universe. *Physical Review Letters*, 49:1110–1113, Oct. 1982. doi: 10.1103/PhysRevLett.49.1110.

N. Hamaus, A. Pisani, P. M. Sutter, G. Lavaux, S. Escoffier, B. D. Wandelt, and J. Weller. Constraints on Cosmology and Gravity from the Dynamics of Voids. *Physical Review Letters*, 117(9):091302, Aug. 2016. doi: 10.1103/PhysRevLett.117.091302.

A. J. Hawken, B. R. Granett, A. Iovino, L. Guzzo, J. A. Peacock, S. de la Torre, B. Garilli, M. Bolzonella, M. Scodeggio, U. Abbas, C. Adami, D. Bottini, A. Cappi, O. Cucciati, I. Davidzon, A. Fritz, P. Franzetti, J. Krywult, V. Le Brun, O. Le Fèvre, D. Maccagni, K. Małek, F. Marulli, M. Polletta, A. Pollo, L. A. M. Tasca, R. Tojeiro, D. Vergani, A. Zanichelli, S. Arnouts, J. Bel, E. Branchini, G. De Lucia, O. Ilbert, L. Moscardini, and W. J. Percival. The VIMOS Public Extragalactic Redshift Survey. Measuring the growth rate of structure around cosmic voids. *Astron. Astrophys.*, 607:A54, Nov. 2017. doi: 10.1051/0004-6361/201629678.

V. Icke. Voids and filaments. *Mon. Not. R. Astron. Soc.*, 206:1P–3P, Jan. 1984. doi: 10.1093/mnras/206.1.1P.

Ž. Ivezić. LSST survey: millions and millions of quasars. In A. Gomboc, editor, *New Frontiers in Black Hole Astrophysics*, volume 324 of *IAU Symposium*, pages 330–337, 2017. doi: 10.1017/S1743921316012424.

E. Jennings, Y. Li, and W. Hu. The abundance of voids and the excursion set formalism. *Mon. Not. R. Astron. Soc.*, 434:2167–2181, Sept. 2013. doi: 10.1093/mnras/stt1169.

M. Y. Khlopov. Particle Dark Matter Candidates. *ArXiv e-prints*, Apr. 2017.

E. Komatsu et al. Seven-year Wilkinson Microwave Anisotropy Probe (WMAP) Observations: Cosmological Interpretation. *Astrophys. J. Suppl.*, 192:18–+, Feb. 2011. doi: 10.1088/0067-0049/192/2/18.

S. D. Landy and A. S. Szalay. Bias and variance of angular correlation functions. *Astrophys. J.*, 412:64–71, July 1993. doi: 10.1086/172900.

S. J. LaRoque, M. Bonamente, J. E. Carlstrom, M. K. Joy, D. Nagai, E. D. Reese, and K. S. Dawson. X-Ray and Sunyaev-Zel'dovich Effect Measurements of the Gas Mass Fraction in Galaxy Clusters. *Astrophys. J.*, 652: 917–936, Dec. 2006. doi: 10.1086/508139.

R. Laureijs, J. Amiaux, S. Arduini, J. . Augueres, J. Brinchmann, R. Cole, M. Cropper, C. Dabin, L. Duvet, A. Ealet, and et al. Euclid Definition Study Report. *ArXiv e-prints*, Oct. 2011.

G. Lavaux and B. D. Wandelt. Precision cosmology with voids: definition, methods, dynamics. *Mon. Not. R. Astron. Soc.*, 403:1392–1408, Apr. 2010. doi: 10.1111/j.1365-2966.2010.16197.x.

R. Li, C. S. Frenk, S. Cole, L. Gao, S. Bose, and W. A. Hellwing. Constraints on the identity of the dark matter from strong gravitational lenses. *Mon. Not. R. Astron. Soc.*, 460:363–372, July 2016. doi: 10.1093/mnras/stw939.

M. Loewenstein and R. E. White, III. Do elliptical galaxies have dark matter? *Phys. Rept.*, 307:75–81, Dec. 1998. doi: 10.1016/S0370-1573(98)00059-3.

G. A. Mamon and E. L. Łokas. Dark matter in elliptical galaxies - II. Estimating the mass within the virial radius. *Mon. Not. R. Astron. Soc.*, 363: 705–722, Nov. 2005. doi: 10.1111/j.1365-2966.2005.09400.x.

Q. Mao, A. A. Berlind, R. J. Scherrer, M. C. Neyrinck, R. Scoccimarro, J. L. Tinker, C. K. McBride, D. P. Schneider, K. Pan, D. Bizyaev, E. Malanushenko, and V. Malanushenko. A Cosmic Void Catalog of SDSS DR12 BOSS Galaxies. *Astrophys. J.*, 835:161, Feb. 2017. doi: 10.3847/1538-4357/835/2/161.

F. Marulli, M. Bolzonella, E. Branchini, I. Davidzon, S. de la Torre, B. R. Granett, L. Guzzo, A. Iovino, L. Moscardini, A. Pollo, U. Abbas, C. Adami, S. Arnouts, J. Bel, D. Bottini, A. Cappi, J. Coupon, O. Cucciati, G. De Lucia, A. Fritz, P. Franzetti, M. Fumana, B. Garilli, O. Ilbert, J. Krywult, V. Le Brun, O. Le Fèvre, D. Maccagni, K. Małek, H. J. McCracken, L. Paioro, M. Polletta, H. Schlagenhaufer, M. Scodeggio, L. A. M. Tasca, R. Tojeiro, D. Vergani, A. Zanichelli, A. Burden, C. Di Porto, A. Marchetti, C. Marinoni, Y. Mellier, R. C. Nichol, J. A. Peacock, W. J. Percival, S. Phleps, M. Wolk, and G. Zamorani. The VIMOS Public Extragalactic Redshift Survey (VIPERS) . Luminosity and stellar mass dependence of galaxy clustering at 0.5 ¡ z ¡ 1.1. *Astron. Astrophys.*, 557: A17, Sept. 2013. doi: 10.1051/0004-6361/201321476.

F. Marulli, A. Veropalumbo, and M. Moresco. CosmoBolognaLib: C++ libraries for cosmological calculations. *Astronomy and Computing*, 14:35–42, Jan. 2016. doi: 10.1016/j.ascom.2016.01.005.

F. Marulli, A. Veropalumbo, L. Moscardini, A. Cimatti, and K. Dolag. Redshift-space distortions of galaxies, clusters, and AGN. Testing how the accuracy of growth rate measurements depends on scales and sample selections. *Astron. Astrophys.*, 599:A106, Mar. 2017. doi: 10.1051/0004-6361/201526885.

F. Marulli, A. Veropalumbo, M. Sereno, L. Moscardini, F. Pacaud, M. Pierre, M. Plionis, A. Cappi, C. Adami, S. Alis, B. Altieri, M. Birkinshaw, S. Ettori, L. Faccioli, F. Gastaldello, E. Koulouridis, C. Lidman, J.-P. Le Fèvre, S. Maurogordato, B. Poggianti, E. Pompei, T. Sadibekova, and I. Valtchanov. The XXL Survey: XVI. The clustering of X-ray selected galaxy clusters at z˜0.3. *ArXiv e-prints*, July 2018.

D. Micheletti, A. Iovino, A. J. Hawken, B. R. Granett, M. Bolzonella, A. Cappi, L. Guzzo, U. Abbas, C. Adami, S. Arnouts, J. Bel, D. Bottini, E. Branchini, J. Coupon, O. Cucciati, I. Davidzon, G. De Lucia, S. de la Torre, A. Fritz, P. Franzetti, M. Fumana, B. Garilli, O. Ilbert, J. Krywult, V. Le Brun, O. Le Fèvre, D. Maccagni, K. Małek, F. Marulli, H. J. McCracken, M. Polletta, A. Pollo, C. Schimd, M. Scodeggio, L. A. M.

Tasca, R. Tojeiro, D. Vergani, A. Zanichelli, A. Burden, C. Di Porto, A. Marchetti, C. Marinoni, Y. Mellier, T. Moutard, L. Moscardini, R. C. Nichol, J. A. Peacock, W. J. Percival, and G. Zamorani. The VIMOS Public Extragalactic Redshift Survey. Searching for cosmic voids. *Astron. Astrophys.*, 570:A106, Oct. 2014. doi: 10.1051/0004-6361/201424107.

H. J. Mo and S. D. M. White. An analytic model for the spatial clustering of dark matter haloes. *Mon. Not. R. Astron. Soc.*, 282:347–361, Sept. 1996. doi: 10.1093/mnras/282.2.347.

A. Natarajan. Bounds on Dark Matter from CMB Observations. In D. Cline, editor, *Springer Proceedings in Physics*, volume 148 of *Springer Proceedings in Physics*, page 67, 2013. doi: 10.1007/978-94-007-7241-0_10.

A. B. Newman, T. Treu, R. S. Ellis, D. J. Sand, J. Richard, P. J. Marshall, P. Capak, and S. Miyazaki. The Distribution of Dark Matter Over Three Decades in Radius in the Lensing Cluster Abell 611. *Astrophys. J.*, 706: 1078–1094, Dec. 2009. doi: 10.1088/0004-637X/706/2/1078.

M. C. Neyrinck. ZOBOV: a parameter-free void-finding algorithm. *Mon. Not. R. Astron. Soc.*, 386:2101–2109, June 2008. doi: 10.1111/j.1365-2966.2008.13180.x.

P. Norberg, C. M. Baugh, E. Gaztañaga, and D. J. Croton. Statistical analysis of galaxy surveys - I. Robust error estimation for two-point clustering statistics. *Mon. Not. R. Astron. Soc.*, 396:19–38, June 2009. doi: 10.1111/j.1365-2966.2009.14389.x.

P. J. E. Peebles. *The large-scale structure of the universe.* 1980.

S. Perlmutter et al. *Astrophys. J.*, 517:565–586, June 1999. doi: 10.1086/307221.

A. Pisani, P. M. Sutter, N. Hamaus, E. Alizadeh, R. Biswas, B. D. Wandelt, and C. M. Hirata. Counting voids to probe dark energy. *Phys. Rev. D*, 92 (8):083531, Oct. 2015. doi: 10.1103/PhysRevD.92.083531.

E. Platen, R. van de Weygaert, and B. J. T. Jones. A cosmic watershed: the WVF void detection technique. *Mon. Not. R. Astron. Soc.*, 380:551–570, Sept. 2007. doi: 10.1111/j.1365-2966.2007.12125.x.

G. Pollina, M. Baldi, F. Marulli, and L. Moscardini. Cosmic voids in coupled dark energy cosmologies: the impact of halo bias. *Mon. Not. R. Astron. Soc.*, 455:3075–3085, Jan. 2016. doi: 10.1093/mnras/stv2503.

G. Pollina, N. Hamaus, K. Dolag, J. Weller, M. Baldi, and L. Moscardini. On the linearity of tracer bias around voids. *Mon. Not. R. Astron. Soc.*, 469:787–799, July 2017. doi: 10.1093/mnras/stx785.

G. Pollina, N. Hamaus, K. Paech, K. Dolag, J. Weller, C. Sánchez, E. S. Rykoff, B. Jain, T. M. C. Abbott, S. Allam, S. Avila, R. A. Bernstein, E. Bertin, D. Brooks, D. L. Burke, A. Carnero Rosell, M. Carrasco Kind, J. Carretero, C. E. Cunha, C. B. D'Andrea, L. N. da Costa, J. De Vicente, D. L. DePoy, S. Desai, H. T. Diehl, P. Doel, A. E. Evrard, B. Flaugher, P. Fosalba, J. Frieman, J. García-Bellido, D. W. Gerdes, T. Giannantonio, D. Gruen, J. Gschwend, G. Gutierrez, W. G. Hartley, D. L. Hollowood, K. Honscheid, B. Hoyle, D. J. James, T. Jeltema, K. Kuehn, N. Kuropatkin, M. Lima, M. March, J. L. Marshall, P. Melchior, F. Menanteau, R. Miquel, A. A. Plazas, A. K. Romer, E. Sanchez, V. Scarpine, R. Schindler, M. Schubnell, I. Sevilla-Noarbe, M. Smith, M. Soares-Santos, F. Sobreira, E. Suchyta, G. Tarle, A. R. Walker, and W. Wester. On the relative bias of void tracers in the Dark Energy Survey. *ArXiv e-prints*, June 2018.

W. H. Press and P. Schechter. Remark on the Statistical Significance of Flares in Poisson Count Data. *Astrophys. J.*, 193:437–442, Oct. 1974. doi: 10.1086/153179.

A. Pujol and E. Gaztañaga. Are the halo occupation predictions consistent with large-scale galaxy clustering? *Mon. Not. R. Astron. Soc.*, 442:1930–1941, Aug. 2014. doi: 10.1093/mnras/stu1001.

E. Ricciardelli, V. Quilis, and J. Varela. On the universality of void density profiles. *Mon. Not. R. Astron. Soc.*, 440:601–609, May 2014. doi: 10.1093/mnras/stu307.

A. G. Riess et al. Observational Evidence from Supernovae for an Accelerating Universe and a Cosmological Constant. *Astron. J.*, 116:1009–1038, Sept. 1998. doi: 10.1086/300499.

T. Ronconi and F. Marulli. Cosmological exploitation of cosmic void statistics. New numerical tools in the CosmoBolognaLib to extract cosmological constraints from the void size function. *Astron. Astrophys.*, 607:A24, Oct. 2017. doi: 10.1051/0004-6361/201730852.

T. Ronconi et al. . in preparation.

M. Sahlén and J. Silk. Cluster-Void Degeneracy Breaking: Modified Gravity in the Balance. *ArXiv e-prints*, Dec. 2016.

R. K. Sheth and R. van de Weygaert. A hierarchy of voids: much ado about nothing. *Mon. Not. R. Astron. Soc.*, 350:517–538, May 2004. doi: 10.1111/j.1365-2966.2004.07661.x.

R. K. Sheth, H. J. Mo, and G. Tormen. Ellipsoidal collapse and an improved model for the number and spatial distribution of dark matter haloes. *Mon. Not. R. Astron. Soc.*, 323:1–12, May 2001. doi: 10.1046/j.1365-8711.2001.04006.x.

V. Springel. The cosmological simulation code GADGET-2. *Mon. Not. R. Astron. Soc.*, 364:1105–1134, Dec. 2005. doi: 10.1111/j.1365-2966.2005.09655.x.

Y. Suto, K. Sato, and H. Sato. Expansion of Voids in a Matter-Dominated Universe. *Progress of Theoretical Physics*, 71:938–945, May 1984. doi: 10.1143/PTP.71.938.

P. M. Sutter, G. Lavaux, N. Hamaus, B. D. Wandelt, D. H. Weinberg, and M. S. Warren. Sparse sampling, galaxy bias, and voids. *Mon. Not. R. Astron. Soc.*, 442:462–471, July 2014. doi: 10.1093/mnras/stu893.

P. M. Sutter, G. Lavaux, N. Hamaus, A. Pisani, B. D. Wandelt, M. Warren, F. Villaescusa-Navarro, P. Zivick, Q. Mao, and B. B. Thompson. VIDE: The Void IDentification and Examination toolkit. *Astronomy and Computing*, 9:1–9, Mar. 2015. doi: 10.1016/j.ascom.2014.10.002.

I. Szapudi, A. Kovács, B. R. Granett, Z. Frei, J. Silk, W. Burgett, S. Cole, P. W. Draper, D. J. Farrow, N. Kaiser, E. A. Magnier, N. Metcalfe, J. S. Morgan, P. Price, J. Tonry, and R. Wainscoat. Detection of a supervoid aligned with the cold spot of the cosmic microwave background. *Mon. Not. R. Astron. Soc.*, 450:288–294, June 2015. doi: 10.1093/mnras/stv488.

A. V. Tikhonov and I. D. Karachentsev. Minivoids in the Local Volume. *Astrophys. J.*, 653:969–976, Dec. 2006. doi: 10.1086/508981.

J. Tinker, A. V. Kravtsov, A. Klypin, K. Abazajian, M. Warren, G. Yepes, S. Gottlöber, and D. E. Holz. Toward a Halo Mass Function for Precision Cosmology: The Limits of Universality. *Astrophys. J.*, 688:709–728, Dec. 2008. doi: 10.1086/591439.

J. L. Tinker, B. E. Robertson, A. V. Kravtsov, A. Klypin, M. S. Warren, G. Yepes, and S. Gottlöber. The Large-scale Bias of Dark Matter Halos: Numerical Calibration and Model Tests. *Astrophys. J.*, 724:878–886, Dec. 2010. doi: 10.1088/0004-637X/724/2/878.

C. G. R. Wallis, J. D. McEwen, T. D. Kitching, B. Leistedt, and A. Plouviez. Mapping dark matter on the celestial sphere with weak gravitational lensing. *ArXiv e-prints*, Mar. 2017.

Y. Wang, L. Xu, and G.-B. Zhao. A Measurement of the Hubble Constant Using Galaxy Redshift Surveys. *Astrophys. J.*, 849:84, Nov. 2017. doi: 10.3847/1538-4357/aa8f48.

M. S. Warren. 2HOT: An Improved Parallel Hashed Oct-Tree N-Body Algorithm for Cosmological Simulation. *ArXiv e-prints*, Oct. 2013.

Y. B. Zeldovich. A hypothesis, unifying the structure and the entropy of the Universe. *Mon. Not. R. Astron. Soc.*, 160:1P, 1972. doi: 10.1093/mnras/160.1.1P.

F. Zwicky. On the Masses of Nebulae and of Clusters of Nebulae. *Astrophys. J.*, 86:217, Oct. 1937. doi: 10.1086/143864.